A measurement of $\psi(2S)$ production cross-section in $\psi(2S) \rightarrow J/\psi(\rightarrow \mu^+\mu^-)\pi^+\pi^-$ decay with ATLAS detector

Lee Allison

MPhys (Lancaster)

Particle Physics Group

Department of Physics

Lancaster University

September 2013

A thesis submitted to Lancaster University for the degree of Doctor of Philosophy in the Faculty of Science and Technology

Abstract

The thesis describes the prompt and non-prompt production cross-sections for $\psi(2S)$ mesons, using 2.1 fb^{-1} of 2011 proton-proton collision data at a centre-of-mass energy of 7 TeV recorded by the ATLAS experiment at the LHC. The measurement uses the decay mode $\psi(2S) \rightarrow J/\psi(\rightarrow \mu^+\mu^-)\pi^+\pi^-$, and studies $\psi(2S)$ with transverse momenta ranging between $p_T = 10-100$ GeV and rapidity $|y| < 2.0$. The prompt and non-prompt production results are compared to existing LHC $\psi(2S)$ measurements and theoretical models.

Dedicated to all the protons that sacrificed their existence, to help reveal the mysteries of the sub-atomic realm.

Acknowledgements

I would like to thank the following. First my supervisor Vato Kartvelishvili, for his support throughout my PhD, especially during the times when I was lost in my own little bubble. The Science and Technology Facilities Council (STFC), because without their funding my PhD and the amazing time spent out at CERN, would have not been possible. James Walder, for his advice and assistance with making sense of the code and my (sometimes stupid) questions. Darren Price, for the help understanding the theory and being an approachable group convener. Lancaster University High Energy Physics group, for being friendly and welcoming. My parents for their help and assistants, with all the moving back and forth, and listening to me talking about things they may not have understood. Finally the long list of people I met at CERN (most notably the LTA group), who made CERN much more than just a place to work, they made it a truly wonderful experience.

Last of all I would like to thank coffee, as it help me to write this thesis.

Declaration

This thesis is my own work and no portion of the work referred to in this thesis has been submitted in support of an application for another degree or qualification at this or any other institute of learning.

"The atoms or elementary particles themselves are not real; they form a world of potentialities or possibilities rather than one of things or facts."
Werner Heisenberg.

"Allons-y!"
10^{th} Doctor, Doctor Who.

Contents

List of Figures

List of Tables

Chapter 1

Introduction

From the dawn of human history, people have always had questions about the fundamental workings of the world around them, with answers ranging from gods to theories. It was using these theories that our knowledge has grown by leaps and bounds over the last few centuries. This was especially true in the 20^{th} century, when the sub-atomic world was discovered and studied by many talented scientists, leading to the formation of the Standard Model (SM) of particle physics, which is the culmination of all our current understanding. It continues to be tested to this day, by ever more powerful accelerators and detectors. One of the places that this work is carried out is the Large Hadron Collider (LHC), built underground at the European Organization for Nuclear Research (CERN) site.

A component of the SM is Quantum Chromodynamics (QCD), and one of the ways that this is studied, is the analysis of heavy quarkonium states, which have been objects of intense theoretical and experimental studies for many decades. There was increased interest in quarkonium production after it was shown that in the J/ψ cross-section there was an order-of-magnitude difference between theoretical expectations and data. Despite these being among the most studied heavy quark bound states, there is still no complete understanding of the underlying production mechanisms and properties of its formation. With the data obtained from the LHC, it will be possible to make comparisons to current theories, and provide feedback to improve future theoretical models.

There have already been measurements of a few of the quarkonium states made at the LHC and the work presented here looks to expand on existing results. The measurements described in this thesis are based on an analysis of proton-proton collision data taken during 2011 and studying both the prompt and non-prompt production of the $\psi(2S)$ meson in the decay mode $J/\psi(\rightarrow \mu^+\mu^-)\pi^+\pi^-$. In the following chapters the relevant information to understand the final results will be provided. Chapter 2 starts with an overview of the SM and its components, as well as details of the most prominent theories of quarkonium production. In Chapter 3 there is an overview of the LHC and a review of the ATLAS detector and its sub-detectors.

Chapter 4 talks about the B-physics triggers and the contributions that were made to their monitoring. Chapter 5 discusses the main $\psi(2S)$ analysis, which is split into sections covering the data used and the event selection, efficiency corrections and finally the fitting procedure. Chapter 6 presents the final results and the systematic studies of the analysis. Finally, Chapter 7 gives a summary of the work presented in this thesis.

There are several appendices that contain further details of the analysis and plots that were used to obtain values shown in Chapters 5 and 6. This work has been published as an ATLAS conference note [1] and presented by the author at the 2013 international charm physics conference.

Chapter 2

Theory

2.1 Standard Model

The Standard Model (SM) is the theory that best describes our current understanding of the fundamental sub-atomic particles and the forces by which they interact. Figure 2.1 shows how the particles of the SM are arranged into several groups, which are defined by properties of the particle, and Figure 2.2 shows how the particles interact with one another. Within the SM there are two main types of particles, fermions and boson. Fermions are defined as particles having half-integer spin, which can be further split into two sub-groups of quarks and leptons, and all the fermions have anti-matter equivalents. Leptons can exist as individual particles, whereas the quarks exist in bound states, such as mesons (quark anti-quark pair) and baryons (3 quarks). The bosons are defined as particles having an integer spin and the SM bosons are responsible for mediating the fundamental forces. The electromagnetic force is mediated by the photon (γ), the weak force is mediated by W^+, W^- and Z boson and the strong force is mediated by the gluon (g). The gravitational force is mediated by the still theoretical graviton, but this is beyond the SM, at the sub-atomic scale gravity has little to no affect.

The SM is the culmination of several decades of work and the combination of a few theories. The SM is a non-abelian gauge theory based on the symmetry group $SU(3)\otimes SU(2)\otimes U(1)$, where the $SU(2)\otimes U(1)$ group describes the

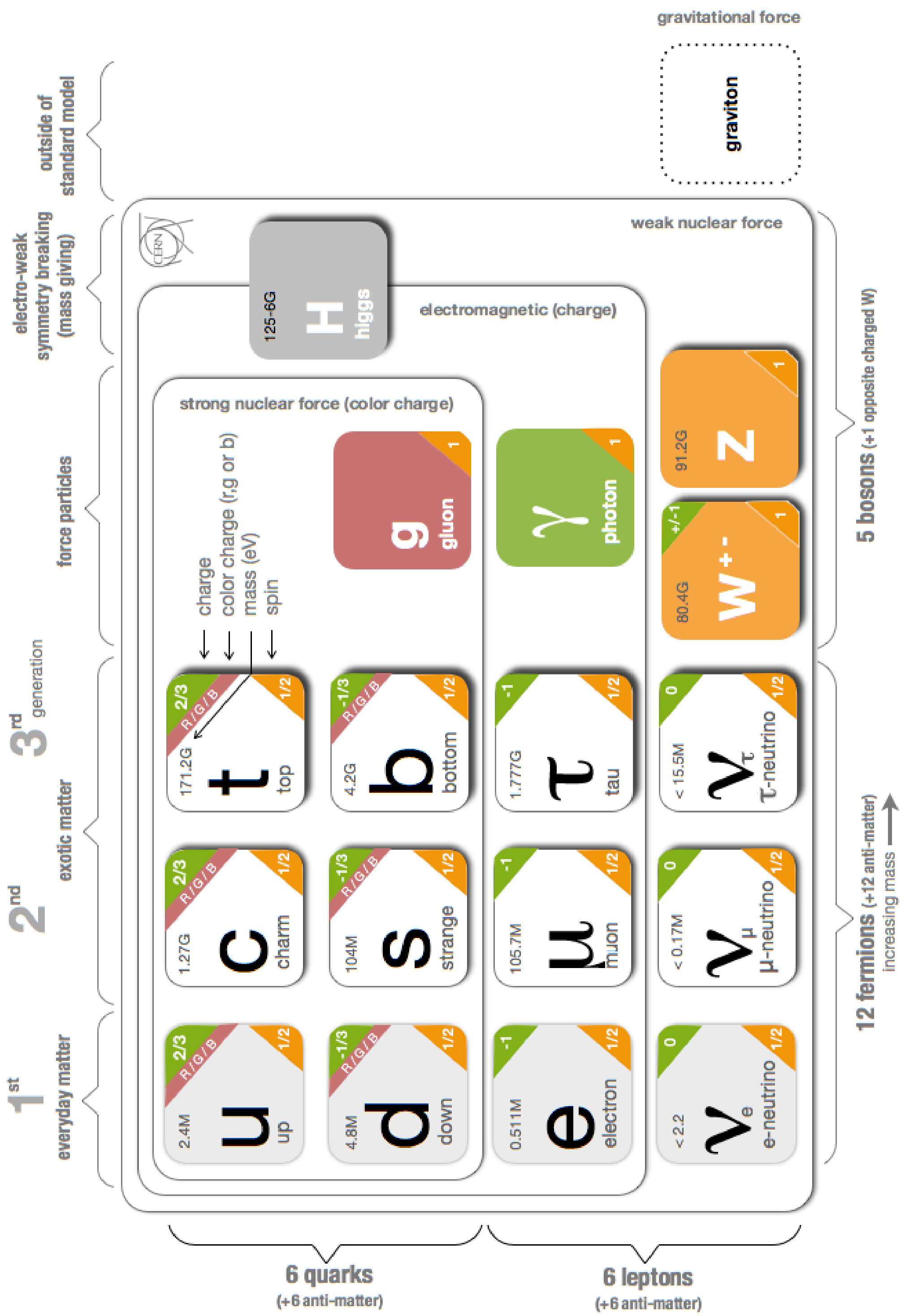

Figure 2.1: Infographic diagram showing the grouping of the particles of the Standard Model [2].

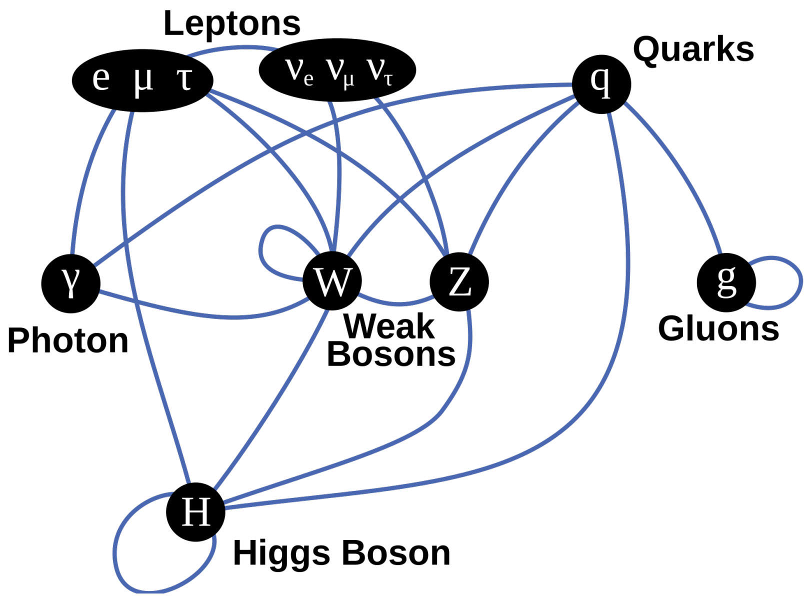

Figure 2.2: A diagram showing how the particles of the Standard Model interact with each other [3].

electroweak interactions (electroweak theory) and SU(3) group describes the interaction of coloured quarks and gluons (quantum chromodynamics) [4].

2.1.1 Electroweak theory

The electroweak theory is the unification of Quantum Electrodynamics (QED) and the theory of weak interactions [5, 6, 7]. The QED is an abelian theory that describes electrically charged particles interacting via the exchange of a neutral photon [8, 9, 10]. Weak interactions allow quarks to change their flavour; a good example of this is beta decay, in which a down quark changes flavour to an up quark, via the emission of a W boson [11, 12]. The difference in mass between the massless photon and the massive $W^{\pm}$ and Z bosons is explained by the introduction of the concept of spontaneous symmetry breaking via the Higgs mechanism, which is mediated by the Higgs boson [13].

2.1.2 Quantum Chromodynamics

Quantum Chromodynamics (QCD) is a non-abelian theory that describes coloured particles interacting via the exchange of gluons [14, 15, 16]. There exist three colour types, red, blue and green; the gluons that mediates coloured interaction themselves contains colour and anti-colour. From this it would be possible to conclude that there are nine states of gluons; however this is not the case as one of the states is a colourless singlet state that is not seen, meaning there are only eight colour octet states. Another consequence of the gluons having colour is that they can interact with themselves, thus making QCD calculations more challenging.

2.2 Quarkonium

Quarkonium is a meson that contains a quark and a anti-quark of the same flavour. Normally "quarkonium" only refers to states containing charm or bottom quarks, as the lighter quarks (up, down, strange) form particles that are a combination of states, and the top quark is too short-lived to form a bound state. The first observed quarkonium state was the J/ψ, which is a $c\bar{c}$ state. It was discovered in 1974 simultaneously at Brookhaven National Laboratory (BNL) [17] and Standford Linear Accelerator Centre (SLAC) [18]. Shortly after the discovery of the J/ψ, other charmonium states were discovered, which can be seen in Figure 2.3. Also a few years later the first bottomonium state was observed [19].

The J/ψ has the quantum numbers $J^{PC} = 1^{--}$, where J is the total spin, P is the parity value and C is the charge parity value. The quantum numbers of the ψ(2S) are the same as the J/ψ, as it is a radially excited state of it. In addition to the S-wave states, there are also P-wave states, most notably $\chi_{c0,1,2}$. Between these states there are various radiative and hadronic transitions. Most important for this analysis are the decays of the ψ(2S) to a J/ψ and two πs, which happens 51.9% of the time. This can be separated into two modes; the highest decay mode is $\psi(2S) \to J/\psi\pi^+\pi^-$, which accounts for 34.0% of the total decays.

The discovery of the X(3872) [20] started a new wave of discoveries of exotic charmonium and charmonium-like states, that are known as the XYZ states [21],

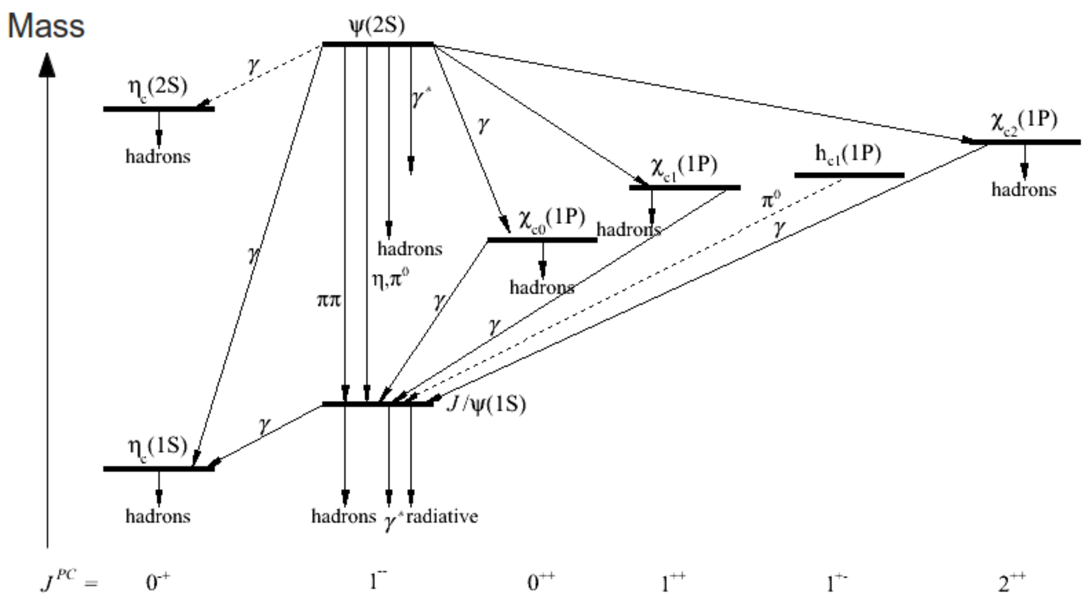

Figure 2.3: Spectrum of charmonium state at different mass and quantum numbers J^{PC}, below the $D\bar{D}$ thresholds (3.728 GeV)

and this period of discovery is still ongoing. So the charmonium spectrum more recently looks like what is shown in Figure 2.4.

2.3 Quarkonium Production

Models for the heavy quarkonium production occurring in hadron-hadron collisions (hadroproduction) need to accurately predict both its cross-section and polarisation. There are two major forms of quarkonium hadroproduction; these are prompt production from QCD sources and feed-down from higher states, and non-prompt from the decay of long-lived particles, such as b-hadrons.

2.3.1 Prompt Production

Prompt quarkonium production proceeds directly via QCD production, from the formation of a quark anti-quark pair into a bound state. The most popular theories of prompt production are the Colour Singlet Model (CSM), Colour Evapora-

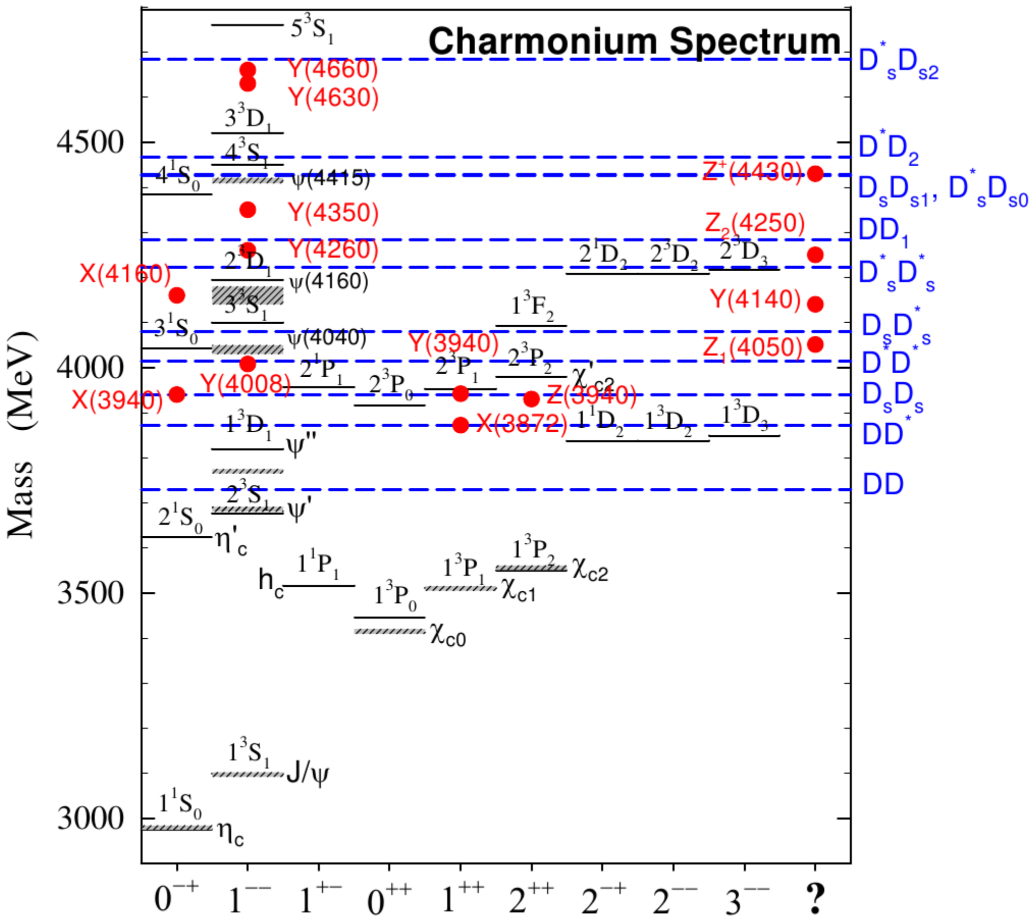

Figure 2.4: The spectrum of charmonium, where the solid lines are quark model predictions, the shaded lines are conventional charmonium states, the dashed blue lines are $D\bar{D}$ thresholds and the red dots are recently discovered charmonium-like states [22].

tion Model (CEM), k_T factorisation model and Non Relativistic QCD (NRQCD). Greater detail of prompt quarkonium production is given in Reference [21, 23]

Colour Singlet Model

The CSM was proposed shortly following the discovery of the J/ψ. In the model it is assumed that the quark-anti-quark ($Q\bar{Q}$) pair produced, have to be in the same colour and spin state as the final state quarkonium. As the quarkonium is a colour singlet state, the $Q\bar{Q}$ pair that produces it must also be in a colour singlet state. In the mid-1990's a clear discrepancy between the prediction of the CSM and the measured cross-section was seen. This is made abundantly obvious in Figure 2.5 where there is an excess in the production of ψ(2S) by nearly 50 times the prediction [24].

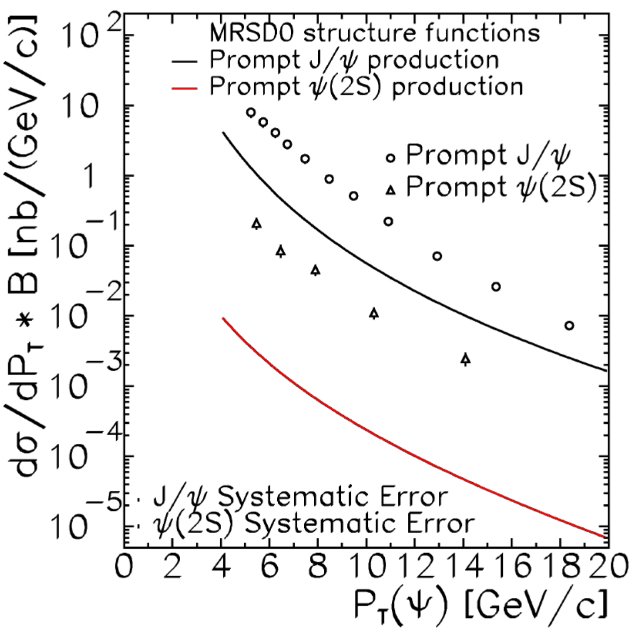

Figure 2.5: Cross-section for prompt J/ψ and $\psi(2S)$ from CDF experiment. The lines are the predictions from CSM [24].

The CSM has recently been calculated at higher orders of α_s, full next-to-leading-order (NLO) and some of the most important next-to-next-to-leading-order (NNLO*) calculations. The partial nature of the NNLO* calculations means they can be dependent on the factorisation and renormalisation scale chosen. The current prediction have had better agreement with the experimental data, which has led to continued interest in the CSM, as an important production mechanism. Figure 2.6 shows three example diagrams of CSM production at leading order, NLO and NNLO. Comparison of predictions with recent ATLAS J/ψ results seen in Figure 2.7, show that CSM is still underestimating the data.

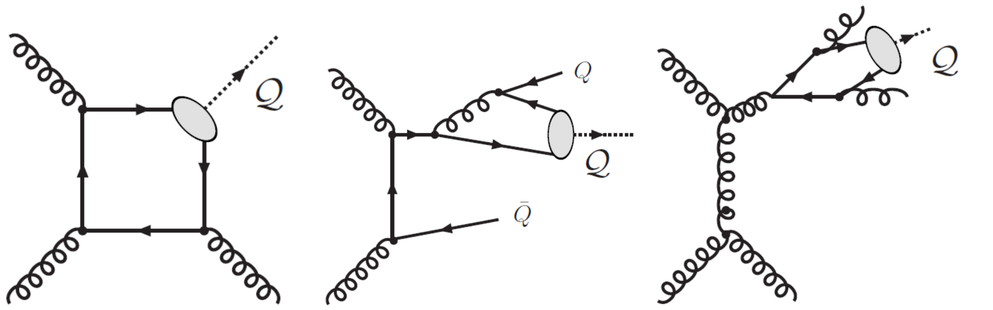

(a) Leading Order CSM **(b)** NLO CSM **(c)** NNLO CSM

Figure 2.6: Example Feynman diagrams of CSM production of quarkonium at Leading Order, NLO and NNLO [25].

Colour Evaporation Model

Another model proposed shortly following the J/ψ discovery was the CEM. The CEM is a phenomenological model that states that every $Q\bar{Q}$ pair can become quarkonium regardless of the colour and spin state, as long as it has an invariant mass that is less than the open-flavour heavy meson threshold, which for charmonium is the $D\bar{D}$. The $Q\bar{Q}$ pair is assumed to interact with the colour field that is produced during the collision; without affecting the kinematics of the $Q\bar{Q}$ pair. This is how it neutralises its colour and what is meant by colour evaporation. Comparison with ATLAS J/ψ results can be seen in Figure 2.7, which shows that the predictions slightly underestimate the data at low p_T and overestimate it at high p_T.

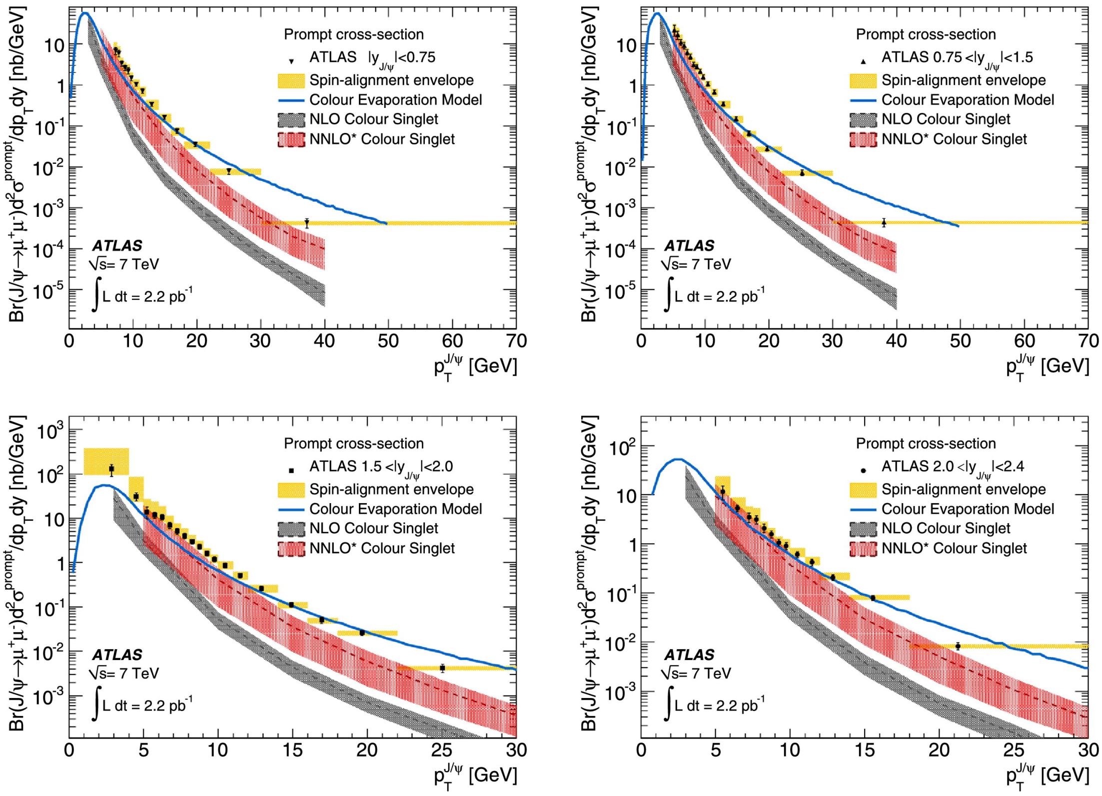

Figure 2.7: Cross-section for prompt J/ψ from ATLAS experiment in the four rapidity regions $|y|$ <0.75, 0.75< $|y|$ <1.5, 1.5< $|y|$ <2.0 and 2.0< $|y|$ <2.4. The predictions shown are for the CSM at NLO (Grey shaded area), NNLO* (Red shaded area), and the CEM (Blue line) [26]

k_T Factorisation Model

The k_T-factorisation model approach is an alternative approach to standard collinear factorisation, which neglects parton transverse momentum. The k_T-factorisation model approach uses a parton-level cross-section prediction from the CSM [27, 28, 29] and attempts to take into account the initial-state radiation effects through parton transverse momentum (k_T) dependent parton distributions. These k_T-dependent parton distributions are not well-constrained phenomenologically, and there are possible unresolved theoretical issues, but study of quarkonium production offers an important testing ground for these approaches and can provide useful feedback [30].

Non-Relativistic QCD

The NRQCD factorisation method, which is also known as the Colour Octet Model (COM) expands the perturbative series, not only in orders of α_s, but also in orders of $m_Q v$, where m_Q is the mass of the heavy quark and v is the typical heavy quark velocity in the centre-of-mass frame. NRQCD factorization contains both CSM and CEM as special cases, but it allows for the possibility of formation of the heavy quark pair in a coloured state which subsequently evolves into a physical singlet quarkonium bound state through the non-perturbative emission of soft gluons.

The inclusive cross-section for direct quarkonium production can be written as the sum of products of short-distance coefficients (σ_n) and long-distance matrix elements (LDME):

$$\sigma[\mathcal{Q}] = \sum_n \sigma_n(\Lambda) \left\langle \mathcal{O}_n^{\mathcal{Q}}(\Lambda) \right\rangle , \tag{2.1}$$

where Λ is the ultraviolet cutoff of the NRQCD effective theory of QCD and $\left\langle \mathcal{O}_n^{\mathcal{Q}} \right\rangle$ are vacuum-expectation values of four-fermion operators.

The LDME describe the probability for a $Q\bar{Q}$ pair in a particular state n to evolve into a heavy quarkonium states $\mathcal{Q}$. These matrix elements must be determined from fits to experimental data, and while a strength of the approach is that for a particular partonic process these matrix elements are universal, the individual matrix elements are often poorly constrained by data and the theoretical observables can be quite dependent on them. This can result in notably different theoretical predictions even for the same order in the perturbative expansion. Currently there is a good agreement with recent data, because the parameters of the theory have been successfully tuned to the data. This agreement can be seen in the CMS result for $\psi(2S) \to \mu^+\mu^-$, as seen in Figure 2.8.

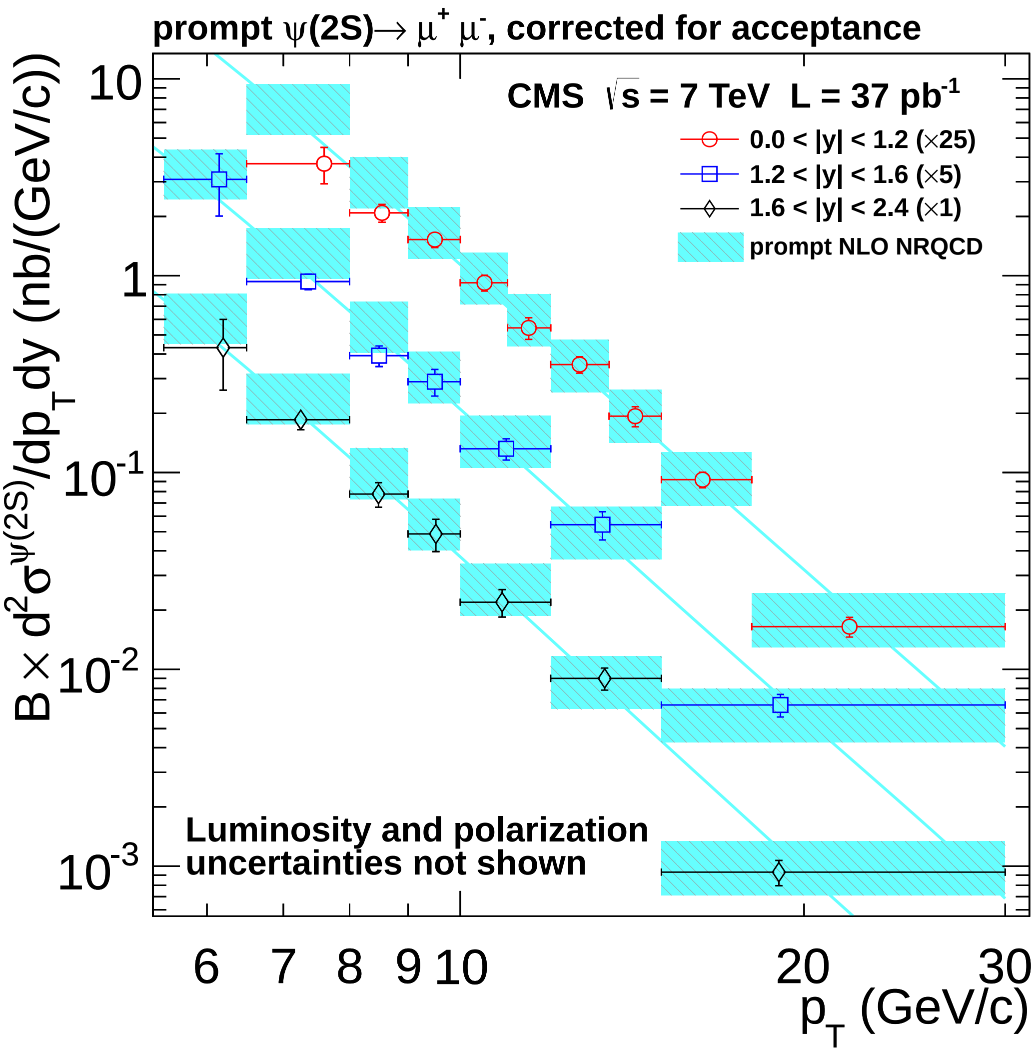

Figure 2.8: Cross-section for prompt $\psi(2S) \to \mu^+\mu^-$ from CMS experiment. The blue shaded areas are the prediction for NLO NRQCD [31]

2.3.2 Non-Prompt Production

Quarkonium can also be produced from the decay of b-hadrons, which can be separated from the promptly produced quarkonium, by making use of the relatively long lifetime of the b-hadrons, which is of the order 10^{-12} seconds. The popular theories for non-prompt production are Fixed Order Next-to-Leading-Log (FONLL) and Next-to-Leading-Order (NLO) approaches, full details of which can be found in Reference [32, 33].

Fixed-Order Next-to-Leading-Log

FONLL predictions are obtained by first determining the b-hadron production spectrum from a NLO QCD calculation matched with an all-order resummation to Next-to-Leading Log (NLL) accuracy in the limit where the transverse momentum ($\mathrm{p}_{T(q)}$) of the heavy quark is much larger than its mass($\mathrm{m}_{(q)}$), where the NLL calculation adds a term of order $\alpha_s^n \log^n(\mathrm{p}_{T(q)}/\mathrm{m}_{(q)})$. The Kartvelishvili fragmentation function parameterisation [34] is used for determination of the fragmentation of the b-quark into b-hadron. Uncertainties on the predictions are assessed by varying the heavy quark mass, evaluating PDF uncertainties and varying the renormalisation and factorisation scales independently up and down by a factor of two from their nominal values. A comparison of FONLL predications with CMS $\psi(2S) \rightarrow \mu^+\mu^-$ data and ATLAS $J/\psi \rightarrow \mu^+\mu^-$ data can be seen in Figures 2.9 and 2.10, respectively.

Next-to-Leading-Order approaches

At small and moderate p_T, near and not significantly larger than the heavy quark mass NLO approaches are expected to do well, when they have the same starting parameters and use the same uncertainty calculations as the FONLL.

It has been noted [33] that by employing a fit of the non-perturbative fragmentation functions used in the NLO predictions to LEP e^+e^- data with a NLO fit the difference between the two predictions can be largely compensated, although this compensation is expected to break down when p_T studied are equal to or

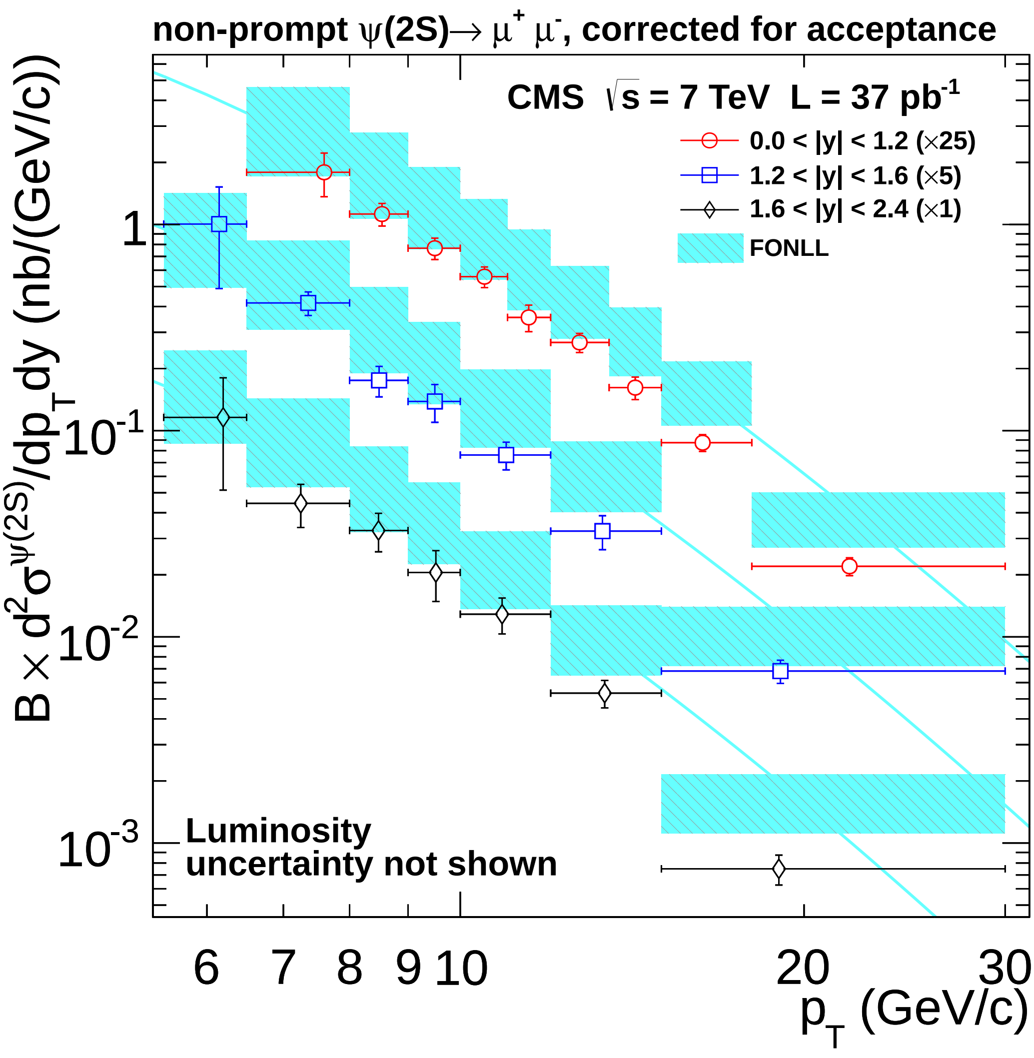

Figure 2.9: Cross-section for non-prompt $\psi(2S) \to \mu^+\mu^-$ from CMS experiment. The blue shaded areas are the prediction for FONLL [31].

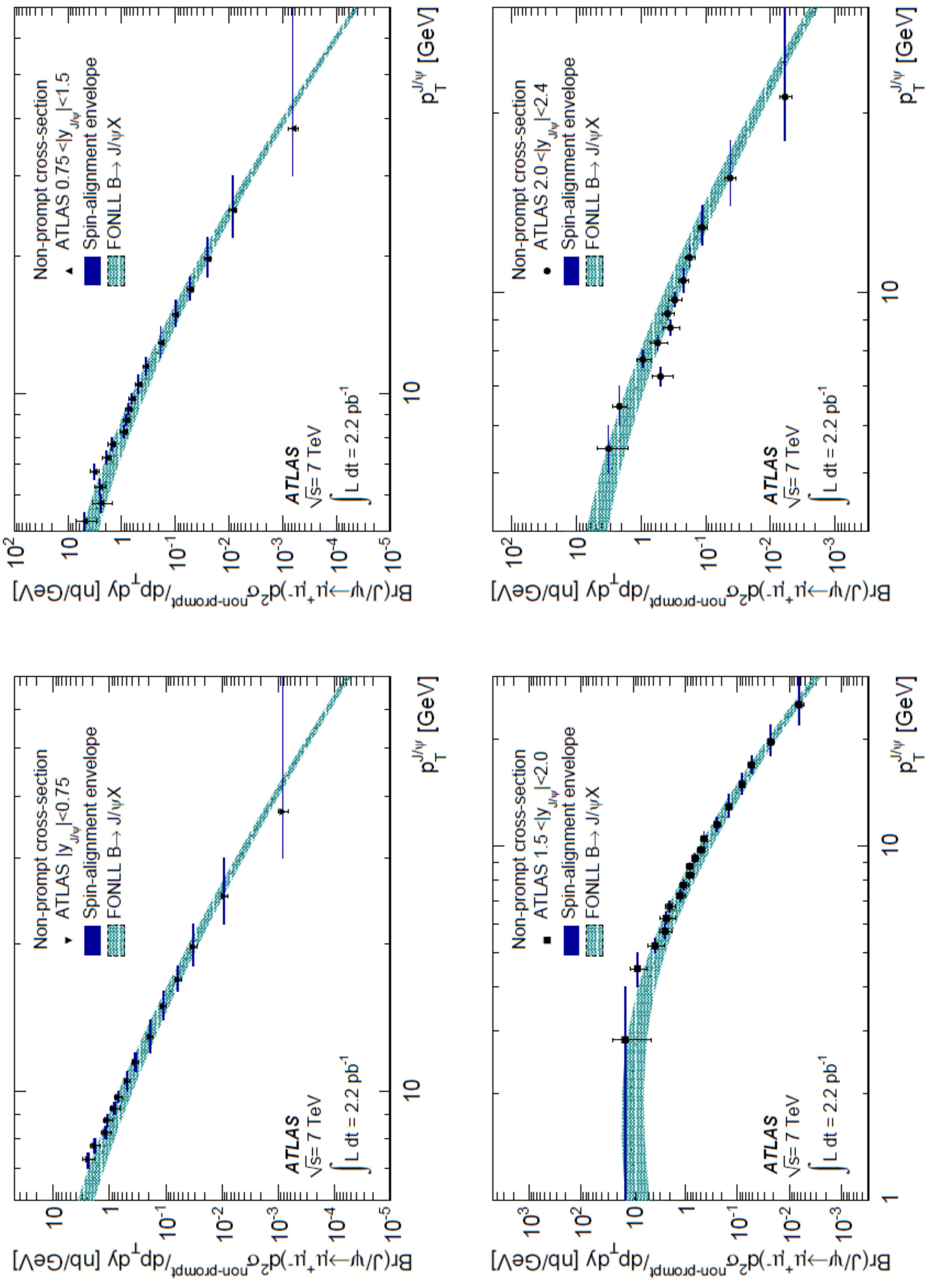

Figure 2.10: Cross-section for non-prompt $J/\psi \to \mu^+\mu^-$ from ATLAS experiment. The blue shaded area is the prediction for FONLL [26].

larger than the Z mass. At low and moderate p_T NLO approaches are expected to have similar accuracy to FONLL.

2.4 Quarkonium spin-alignment

The spin-alignment of a quarkonium state in its decay into a pair of leptons, in its decay frame is calculated [35] by,

$$\frac{\mathrm{d}^2 N}{\mathrm{d}\cos\theta^* \mathrm{d}\phi^*} \propto \left(\frac{1}{3+\lambda_\theta}\right)\left(1+\lambda_\theta \cos^2\theta^* + \lambda_\phi \sin^2\theta^* \cos 2\phi^* + \lambda_{\theta\phi} \sin 2\theta^* \cos\phi^*\right), \tag{2.2}$$

where the λ_i are coefficients related to the spin density matrix elements of the quarkonium wavefunction. Here, in the helicity frame (HX), θ^* is the angle between the direction of the positive lepton momentum ($^+$) in the decay frame with respect to the direction of the quarkonium momentum in the laboratory frame, while ϕ^* is the angle between the production and decay planes of the quarkonium, these angles are illustrated in Figure 2.11 and is covered in greater depth in Ref [36].

In the decay $\psi(2S) \to J/\psi\pi\pi$, the $\pi\pi$ system was shown to be a S-wave state [37], which is the same as the $J/\psi\pi\pi$ system. This means that there is a flat angular distribution between the $\pi\pi$ and J/ψ planes, so the spin-alignment of the $\psi(2S)$ is fully transferred to the J/ψ.

There have recently been measurements of the spin-alignment of the J/ψ and $\psi(2S)$ [38], which are shown in Figure 2.12, as well as all three Υ states [39]. These results show nearly no spin-alignment, as on average all λ_i are close to zero. Nevertheless the present analysis keeps the options open by providing spin-alignment cases, where the values of λ_i are non-zero.

In the default case of isotropic $\psi(2S)$, all three λ_i coefficients in Equation 2.2 are equal to zero. This assumption is compatible with recent measurements, as mentioned above.

In certain areas of the phase space, the kinematic acceptance may depend quite strongly on the values of the λ coefficients in Equation 2.2. So the seven extreme cases that lead to the largest possible variations of kinematic acceptance

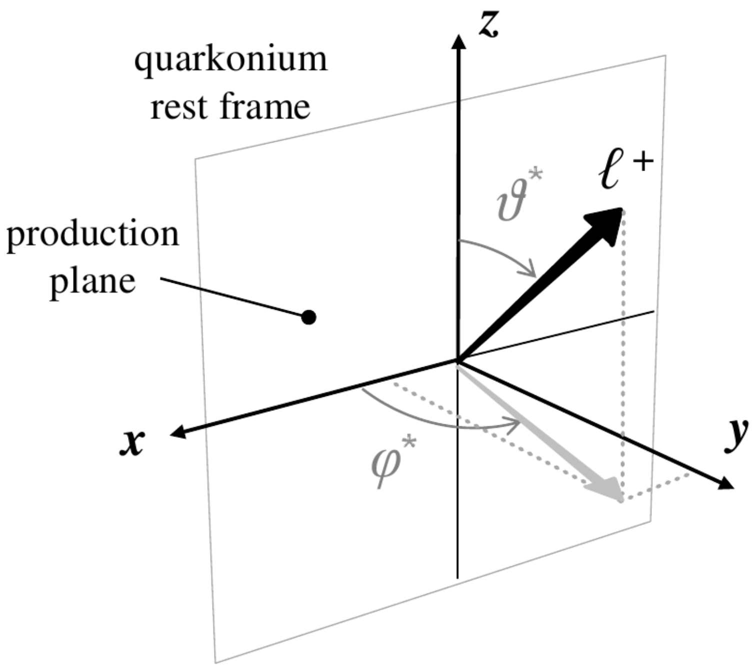

(a) Illustration of the angles used for spin-alignment studies.

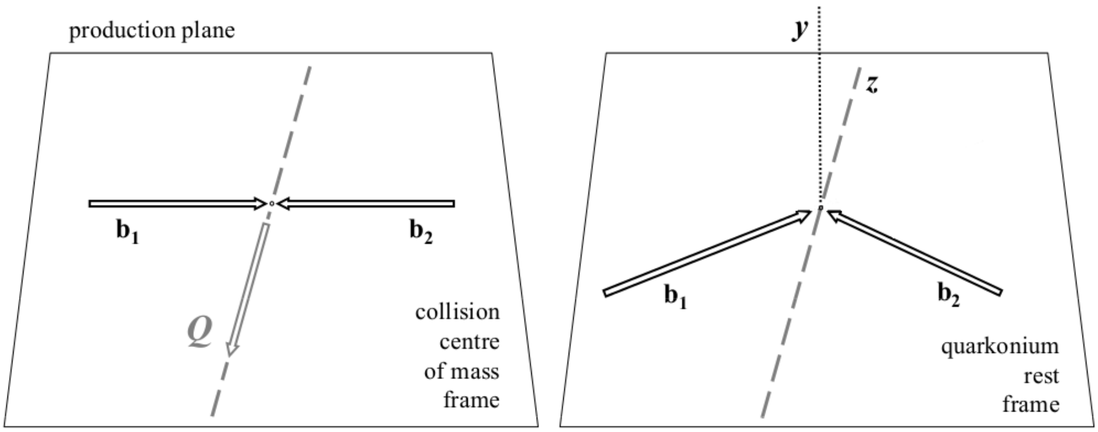

(b) Illustration of the planes used for spin-alignment studies.

Figure 2.11: Illustration of the angles and planes used for spin-alignment studies, which shows the directions of motion of the colliding beams (b_1 and b_2), the y-axis is perpendicular to the plane containing the momenta of b_1 and b_2 and the z-axis is defined by using HX [36].

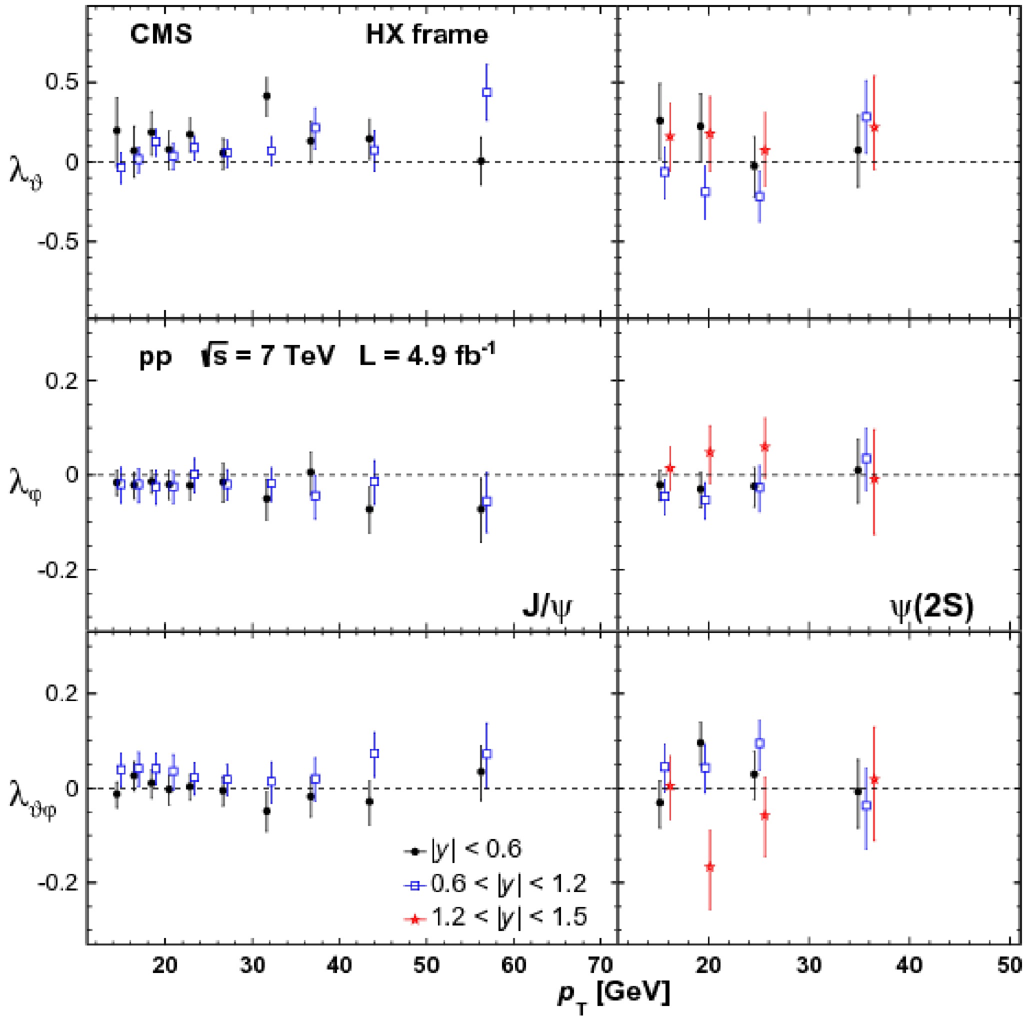

Figure 2.12: CMS spin-alignment results for the three λ_i coefficients as a function of p_T for several $|y|$ regions. The error bars represent total uncertainties (at 68.3% confidence level) [38].

in the allowed phase space are used for this measurement, where the phase space is illustrated in Figure 2.13. These seven extreme cases are defined as follows:

- isotropic distribution independent of θ^* and ϕ^*:
  $\lambda_\theta = \lambda_\phi = \lambda_{\theta\phi} = 0$, (Isotropic);
- longitudinal alignment:
  $\lambda_\theta = -1, \lambda_\phi = \lambda_{\theta\phi} = 0$, (Longitudinal);
- three types of transverse alignment:
  $\lambda_\theta = +1, \lambda_\phi = \lambda_{\theta\phi} = 0$, (Transverse zero)
  $\lambda_\theta = +1, \lambda_\phi = +1, \lambda_{\theta\phi} = 0$, (Transverse positive)
  $\lambda_\theta = +1, \lambda_\phi = -1, \lambda_{\theta\phi} = 0$, (Transverse negative);
- two types of off-plane alignment:
  $\lambda_\theta = 0, \lambda_\phi = 0, \lambda_{\theta\phi} = +0.5$, (Off-plane positive)
  $\lambda_\theta = 0, \lambda_\phi = 0, \lambda_{\theta\phi} = -0.5$, (Off-plane negative).

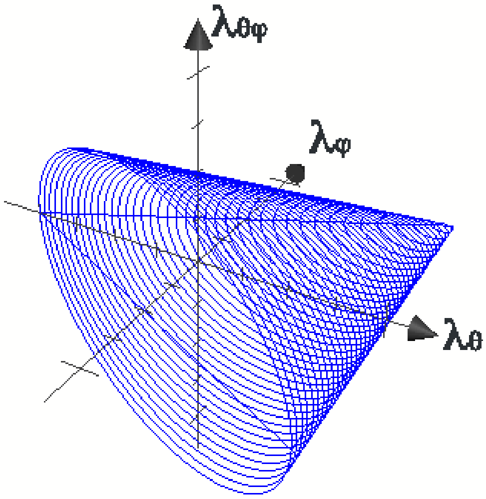

Figure 2.13: A 3-dimensional representation of the allowed phase space of the spin-alignment [35].

Later in the ψ(2S) analysis chapter the six anisotropic spin-alignment scenarios will be used to show the variation of the kinematic acceptance, in relation to the isotropic case.

Chapter 3

LHC and ATLAS Detector

3.1 LHC overview

The LHC is currently the highest energy superconducting hadron accelerator and collider in the world. The LHC is the successor to the Large Electron-Positron Collider (LEP) and was constructed in the existing tunnels, which have a circumference of 27 km and are on average 100 m underground that span across the French-Swiss border. The LHC was designed to collide proton bunches at centre of mass energies of $\sqrt{s}$ = 14 TeV with a machine luminosity of L = 10^{34} cm^{-2}s^{-1}. This is done by accelerating the protons through a series of existing small accelerators, which are shown in Figure 3.1. Before entering the accelerators, first the proton bunches are created by stripping the electrons off the hydrogen atoms. Then the smaller accelerators work in the steps detailed in Table 3.1

Once in the LHC the beam is controlled using liquid helium cooled superconducting magnets operating at 1.9 K. There are dipole magnets that bend the beam and quadrupole magnets that focus the beam. Also there are radio frequency (RF) cavities that are tuned to either accelerate or decelerate the particles to keep them at the preferred energy [42].

The LHC has four main experiments, as indicated in Figure 3.1. The biggest of these are the two large general purpose experiments ATLAS (**A** **T**oroidal **L**HC

Table 3.1: The accelerators used at CERN and the beam energies they produce [40].

Accelerator	Final Beam Energy
Linear Accelerator (Linac 2)	50 MeV
Booster synchrotron (BOOSTER)	1.4 GeV
Proton Synchrotron (PS)	25 GeV
Super Proton Synchrotron (SPS)	450 GeV
LHC	upto 7 TeV

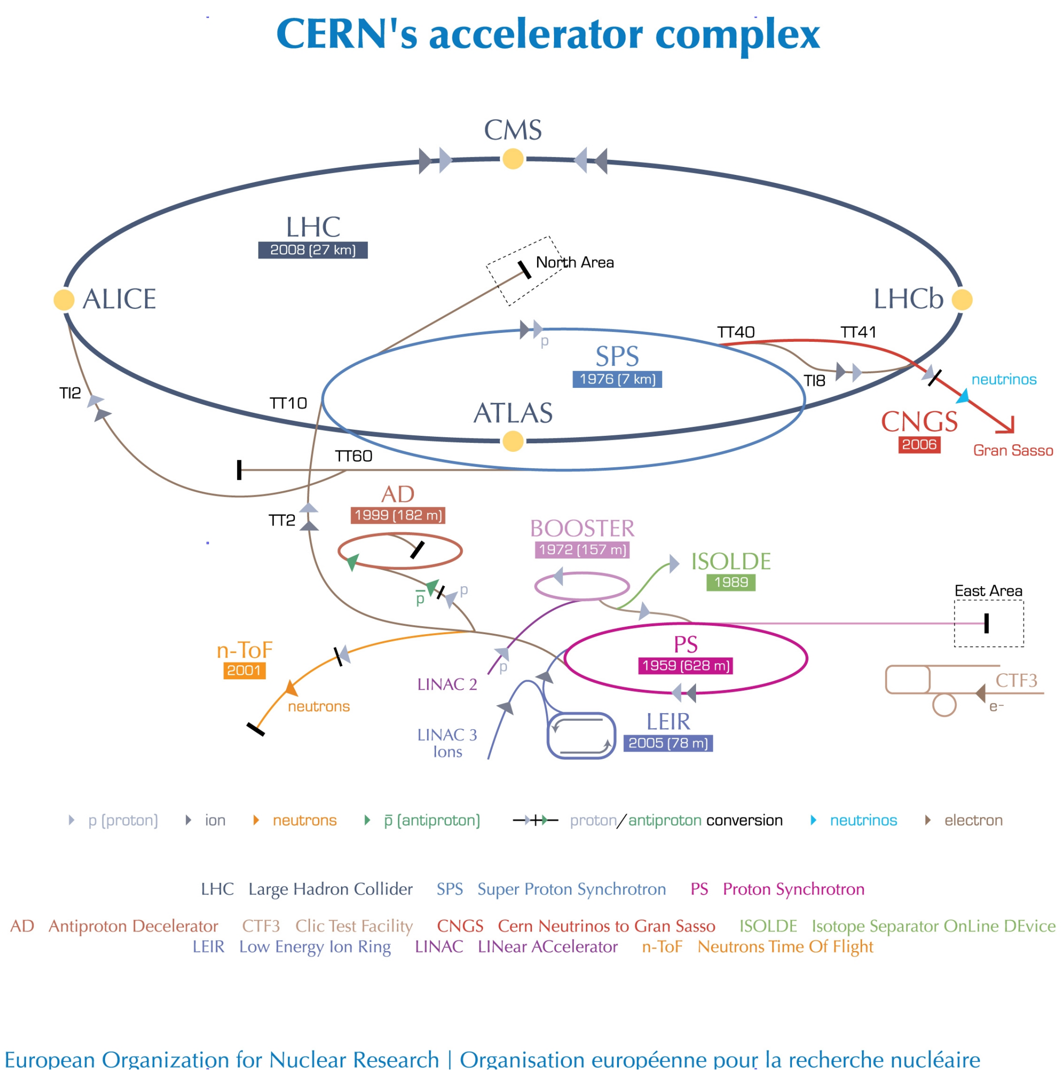

Figure 3.1: Diagram of the LHC and the smaller accelerators leading into it [41]

Apparatu**S**) and CMS (**C**ompact **M**uon **S**olenoid). Also there is the LHCb (**L**arge **H**adron **C**ollider **b**eauty) experiment, which looks into CP violating B-physics, and the ALICE (**A** **L**arge **I**on **C**ollider **E**xperiment) experiment, which has the main goal of investigating heavy ion collisions.

The LHC had a troubled beginning, as shortly after power testing began in 2008, an electrical fault caused a magnet quench, which led to the sudden heating of the liquid helium that expanded with explosive force [43]. As a result a new quench-protection system was installed in the LHC, to stop a repeat of this incident [44]. The LHC had beams circulating again in November 2009 [45]. After that the LHC successfully ran at $\sqrt{s}$ = 7 TeV (3.5 TeV per beam) during 2010 and 2011, and at $\sqrt{s}$ = 8 TeV (4 TeV per beam) during 2012. Collectively these three years are known as Run 1, in which the LHC delivered a total integrated luminosity to ATLAS of 28.31 fb^{-1}: 48.1 pb^{-1} in 2010, 5.46 fb^{-1} in 2011 and 22.8 fb^{-1} in 2012 of proton-proton collision data [46], and the cumulative luminosity across these years is shown in Figure 3.2.

During this time ATLAS first discovered the $\chi_b(3P)$ meson [47] in 2011 and in 2012 both ATLAS and CMS jointly announced the discovery of the Higgs boson [48, 49]. Currently the LHC is in Long Shutdown 1 (LS1), during which time the accelerator and the detectors will be upgraded to handle an increase in the beam energy, and will start colliding beams again in 2015.

3.2 ATLAS

The ATLAS detector [50] is a general purpose experiment running at the LHC, which is studying proton-proton and heavy-ion collisions. The aims of the ATLAS detector is to improve existing measurements and search for new physics, such as the Higgs boson, supersymmetry (SUSY) and more sources of CP violation. The ATLAS detector is 46 m long, has a diameter of 25 m and in total weight about 7,000 tonnes.

The Cartesian coordinate system of the ATLAS detector defines the direction of the beam pipe as the z-axis, meaning that the $x - y$ plane is transverse to the beam pipe. Here the positive directions are defined as follows: x-axis is pointing

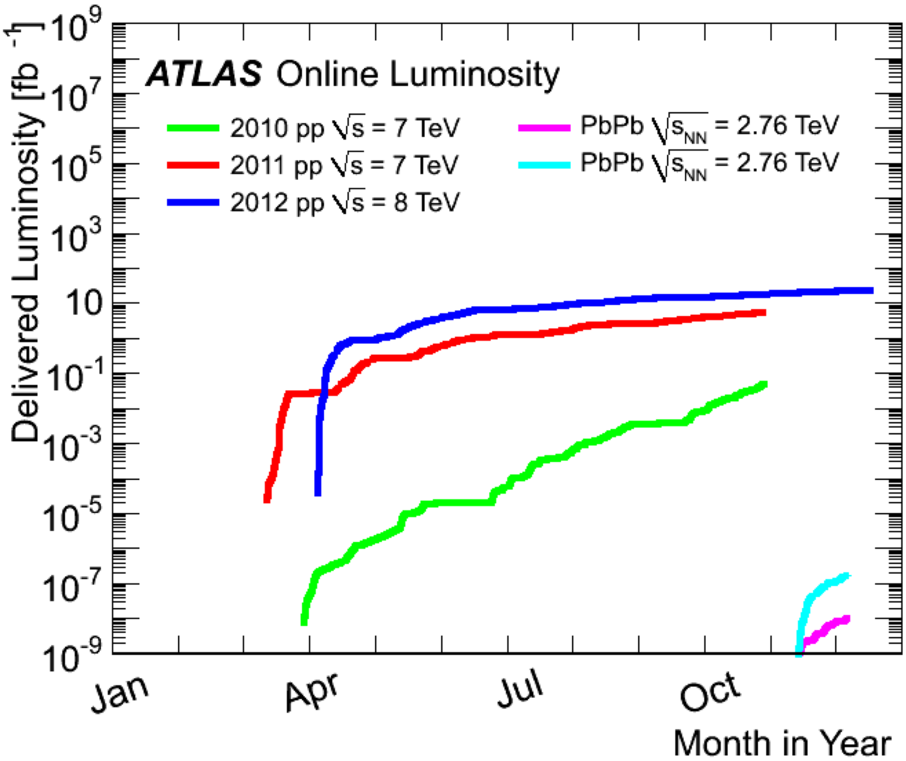

Figure 3.2: Cumulative luminosity delivered by ATLAS versus the months of the year. Showing proton-proton collision data for 2010 (green), 2011 (red) and 2012 (blue). Also shown is the lead-lead collision data for 2010 (magenta) and 2011 (cyan) [46]

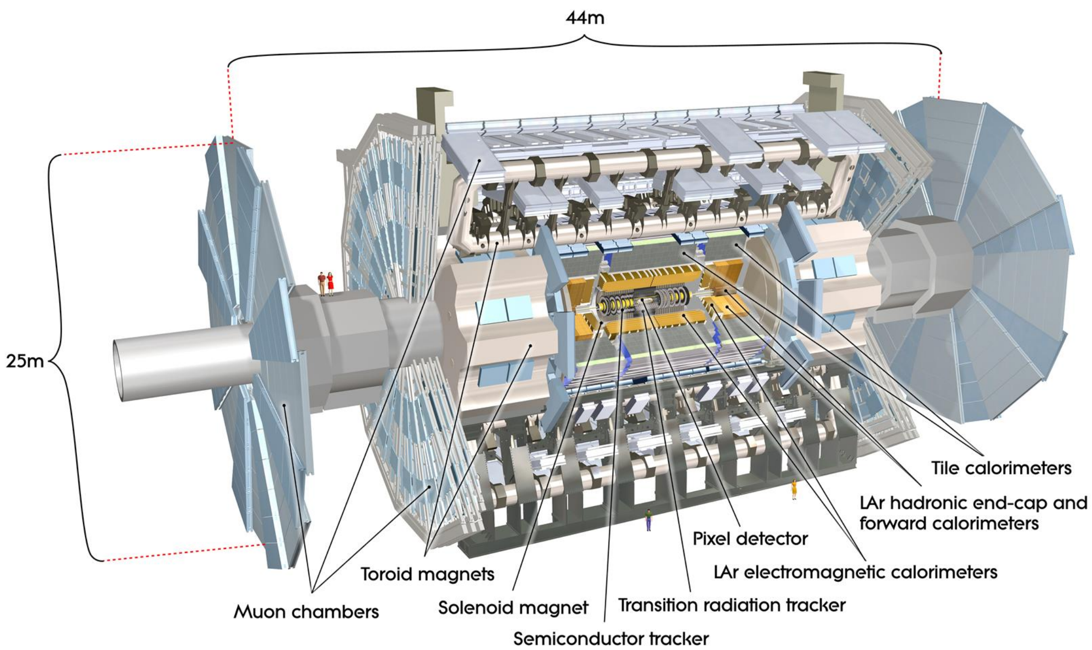

Figure 3.3: A cutaway of the ATLAS detector showing the position of its sub-detectors. [51]

into the centre of the LHC ring, y-axis is pointing upwards and z-axis is heading towards side-A of the detector. The spherical coordinates define the azimuthal angle ϕ as being measured around the z-axis and the polar angle θ as being the angle from the z-axis. In particle physics, pseudorapidity η and rapidity y are commonly used variables.They are defined as follows:

$$\eta = -\ln\left(\tan\left(\frac{\theta}{2}\right)\right) \tag{3.1}$$

$$y = \frac{1}{2}\ln\left(\frac{E + p_z}{E - p_z}\right) \tag{3.2}$$

where E is the energy of the particle and p_z is the momentum along the z-axis. For massless particles $y = \eta$.

The ATLAS detector contains a number of sub-detectors. The innermost of these is the Inner Detector (ID), then the two types of calorimeters, electromagnetic (ECAL) and hadronic (HCAL) and the outermost is the Muon Spectrometer (MS). An illustration of the ATLAS detector and its sub-detector can be seen in Figure 3.3.

3.2.1 Inner Detector

The ID is placed in the centre of the ATLAS detector and provides the measurements of particle's momentum and vertex position in the region $|\eta| < 2.5$. This is done with the high granularity of the sub-systems of the ID, which are the pixel detector, the semiconductor tracker (SCT) and the transition radiation tracker (TRT). The layout of the three sub-systems is shown in Figure 3.4. All of the ID is placed in a nominal magnetic field of 2 T, generated by a central solenoid that is part of the ID. The detector itself measures 7m in length and has a radius of 1.15m.

3.2.1.1 Pixel Detector

The pixel detector is placed as close as possible to the beam pipe and is only a few centimetres away from it, in order to achieve the highest possible precision.

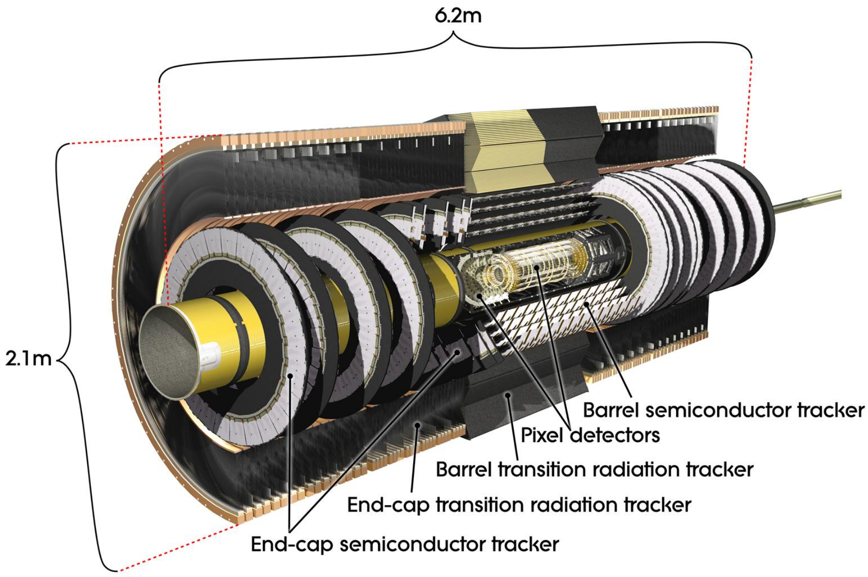

Figure 3.4: A cutaway of the Inner Detector showing the position of its sub-systems. [52]

It achieves the necessary resolution by using a total of 80 million pixels that cover an area of 1.7 m^2, where the nominal pixel size is 50 μm $\times$ 400 μm in $(R-\phi)\times z$, which achieve a resolution of 10 μm in $(R-\phi)$ and 115 μm (z in the barrel region and R in the end-caps). The pixel detector is split into three layers in the barrel region, the spacing of which is illustrated in Figure 3.5. The innermost of these layers is known as the B-layer and is important in the secondary vertex reconstruction, which is essential for B-physics analyses. The end-caps of the pixel detector are placed at 495 mm, 580 mm and 650 mm along the z-axis.

3.2.1.2 Semiconductor Tracker

The SCT is the middle sub-system of the ID using sensing elements that work in a similar way to those in the pixel detector, but in the SCT strips are used rather than pixels. In the barrel region there are four layers, as illustrated in Figure 3.5 and 2 sets of nine disks in the end-caps. In the barrel region the sensors consist of two 6.4 cm strips with a pitch of 80 μm. In both the barrel and the end-caps the strips are double sided, which have a slight angle between them of 40 mrad,

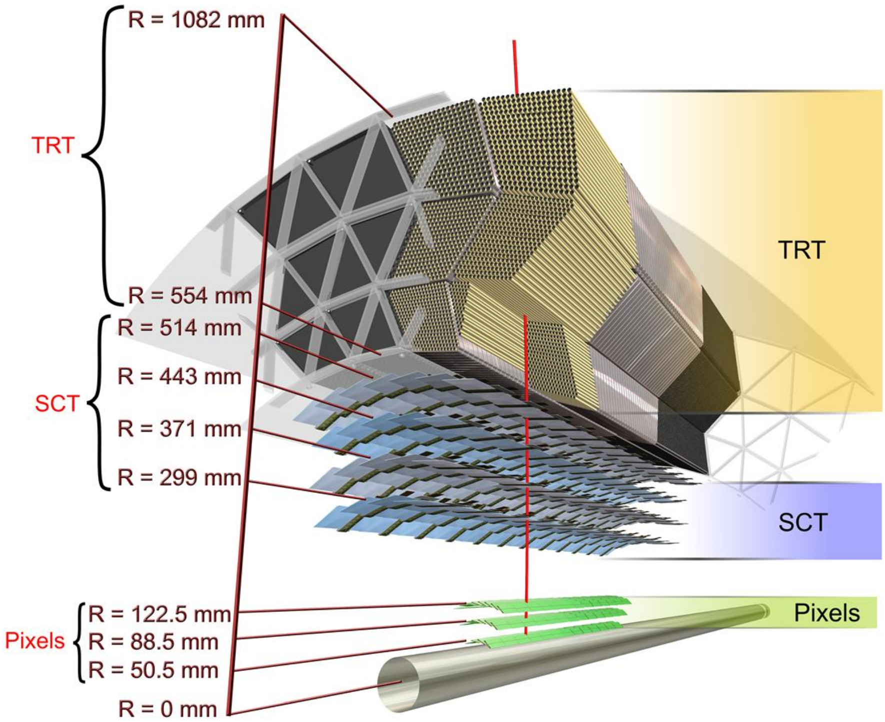

Figure 3.5: The position of the layers of the Inner Detector's sub-systems. [52]

which provides a stereo measurement. So in total the SCT has a detection surface area of 60 m^2, which has a resolution 17 μm $(R-\phi)$ and 580 $\mu m(z$ in barrel and R in end-caps).

3.2.1.3 Transition Radiation Tracker

The outer sub-system of the ID is the TRT, which is based on 4 mm drift straw detectors. In the centre of each straw is a 30 μm diameter gold-plated tungsten sense wire, which only provides a two-dimensional measurement in $(R-\phi)$ plane to a resolution of 130 μm. The straws are filled with a gas mixture of 70% xenon, 27% carbon dioxide and 3% oxygen. The longest straws measure 144 cm, which are around the barrel parallel to the z direction and are split into two at approximately $\eta = 0$ and read out at both ends. The straws in the end-caps measure 37 cm long and are arranged radially.

3.2.2 Calorimeters

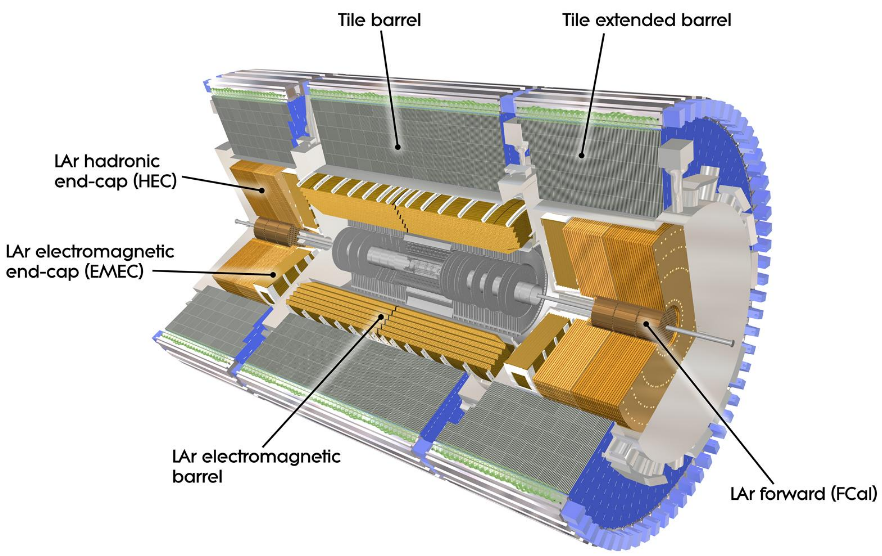

Figure 3.6: A cutaway of the calorimeters showing the position of its sub-systems. [53]

The calorimeters are used to measure the energies of both charged and neutral particles. The innermost calorimeter is the ECAL and the outer is the HCAL, as illustrated in Figure 3.6. Together they cover a range upto $|\eta| = 4.9$. There is finer granularity of the ECAL over the η region that matches the ID, and wider granularity in the rest. The calorimeters are also designed to limit non-muon particles from entering into the MS.

3.2.2.1 Electromagnetic Calorimeter

The barrel section of the ECAL covers the region $|\eta| < 1.475$, while the electromagnetic end-cap (EMEC) covers $1.375 < |\eta| < 3.2$. The ECAL works by having lead absorbers arranged in an accordion shape, with liquid argon (LAr) between the lead plates. The accordion shape is important to get complete ϕ coverage. Within the LAr there is a copper grid, which detects the electrons liberated from LAr as the particles pass through it. The granularity of the ECAL varies between 0.003-0.1 in $\Delta\eta$ and 0.025-0.1 $\Delta\phi$, depending on whether in the barrel or end-caps.

3.2.2.2 Hadronic Calorimeter

Directly after the ECAL in the barrel region is the tile calorimeter, which uses an extended barrel to cover the region $|\eta| < 1.7$. The tile calorimeter uses steel absorbers with scintillating tiles as the active medium that are connected to photomultiplier tubes via fibre optic cables. The scintillating tiles provide a granularity of 0.1×0.1 in $\Delta\eta \times \Delta\phi$ in the inner layers and in the outermost layer it increases to 0.2×0.1 in $\Delta\eta \times \Delta\phi$.

The hadronic end-caps (HEC) use copper absorbers and LAr as their active medium; they cover the range $1.5 < |\eta| < 3.2$. The HEC are placed right next to the EMEC and share the same LAr cryostat. The forward calorimeter (FCAL) also uses the LAr cryostat and uses copper or tungsten as absorbers to extend the coverage from $3.1 < |\eta| < 4.9$. In these high $|\eta|$ regions the reason that the HEC and FCAL are using LAr as a sensing element is due the fact that they are in a area exposed to high radiation and LAr calorimeters are more resistant to radiation.

3.2.3 Muon Spectrometer

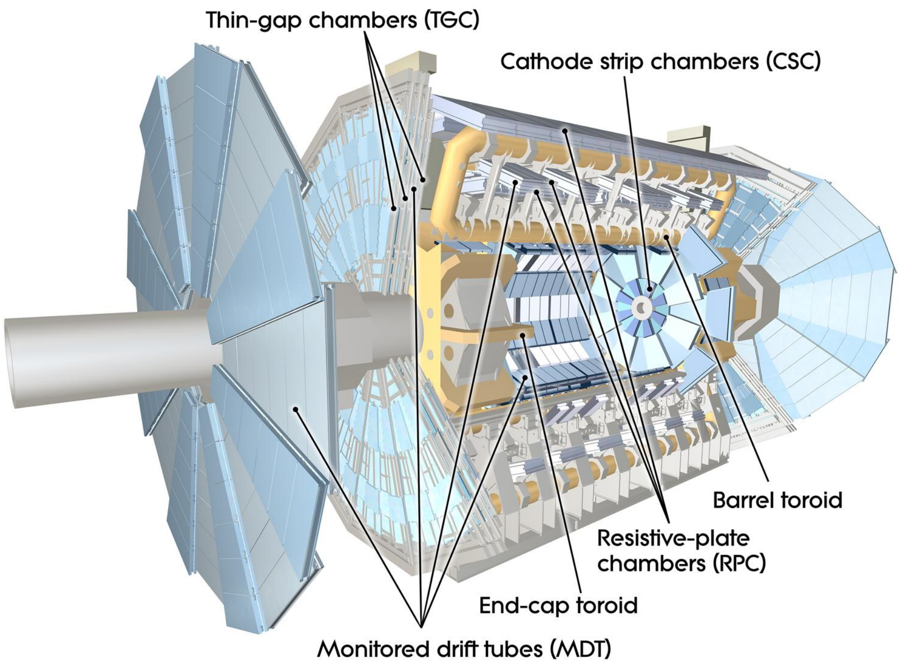

Figure 3.7: A cutaway of the Muon Spectrometer showing the position of its sub-systems. [54]

The muon spectrometer is the outermost section of the ATLAS detector. The detectable particles that travel through the whole detector without being fully stopped, majority of the time are muons. The MS consists of four types of detectors; these are: Monitored Drift Tubes (MDT); Resistive Plate Chambers (RPC); Thin Gap Chambers (TGC) and Cathode Strip Chambers (CSC) all of which are shown in Figures 3.7, 3.8 & 3.9. In the MS there are two detectors used for precision tracking measurements, which are the MDT and CSC. These detectors can measure muons with $p_T > 3$ GeV to a resolution of 4 % up to p_T 100 GeV and beyond this the resolution increases to 10% at 1 TeV. The other two types of detectors, the RPC and TGC are used for muon triggering, as they have to have a fast response of about a few nanoseconds, after the particles have passed through. All four of these detectors are built around a barrel and two end-cap air-core toroid magnets that produce an approximate 0.5-1 T field, but the field is not uniform through the entire set of magnets. This is corrected for using computer models normalised with readings from sensors in the MS.

3.2.3.1 Precision-tracking chambers

The MDT cover the range $|\eta| < 2.7$ and consist of three to eight layers of drift tubes that provide an average resolution of 80 μm. The tubes themselves are about 30 mm in diameter with a 50 μm gold plated W/Re wire in a 93% argon, 7% carbon dioxide and H_2O at < 1000 ppm gas mixture. The CSC replaces the MDT as the first layer in the range $2 < |\eta| < 2.7$; this is due to the higher rate that they can handle, but can still provide a resolution of 60 μm. The CSC uses multi-wire chambers that have 30 μm wires with cathodes both perpendicular and parallel to them in a 80% argon and 20% carbon dioxide gas mixture.

3.2.3.2 Trigger chambers

The RPC are used in the barrel region ($|\eta| <1.05$) and the TGC cover the end-caps ($1.05 < |\eta| < 2.4$). Both chambers were designed to have fast response times, so that they trigger on individual bunch crossings (faster than 25 ns). The RPC consists of two parallel electrode plate that are spaced 2 mm apart, with a low operating voltage gas mixture between them. The TGC work on the same principle as multi-wire proportional chambers, and have 50 μm wires.

3.2.4 Muon Identification

In ATLAS there are three classification of muons, which are defined by how they are reconstructed.

Standalone muon
A standalone muon is only reconstructed using the MS. The muon momentum is corrected to take into account the energy loss of the muon as it passes through the detector material. The track information of the muon is calculated by extrapolating it back to the interaction point.

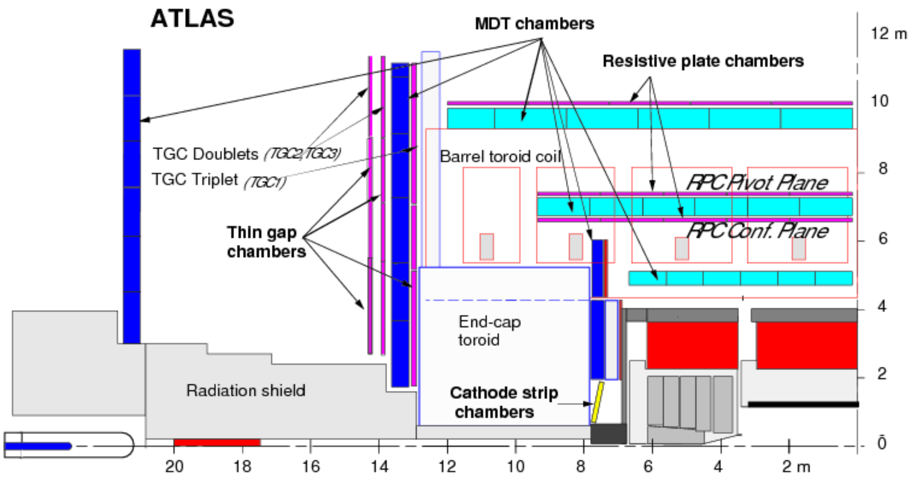

Figure 3.8: A diagram of of the Muon Spectrometer in the zy plane moving outwards from the interaction point (bottom right corner) [55].

Combined muon

A combined muon is when the muon from the MS is combined with the momentum of a track from in the ID. Being combined with a ID track means that the track information can be directly obtained.

Segment tagged muon

A segment tagged muon is when the ID track is extrapolated to the MS and the track can be associated with hits in the MS.

3.2.5 Magnetic System

As mentioned previously in the Section 3.2.1 and Section 3.2.3 the magnet system in ATLAS consist of four superconducting magnets, one solenoid, one barrel toroid and two end-cap toroids. The central solenoid surrounds the ID, measures 5.8 m long and 2.56 m in diameter, and produces a magnetic field ranging between 0.9 - 2.0 T. The barrel toroid surrounds the calorimeters, measures 25.3 m in length and has a diameter ranging from 9.4 to 20.1 m and has a magnetic field ranging between 0.2 - 2.5 T. The end-cap toroids are placed outside the calorimeters and have a radial overlap with the barrel toroid to provide a smooth

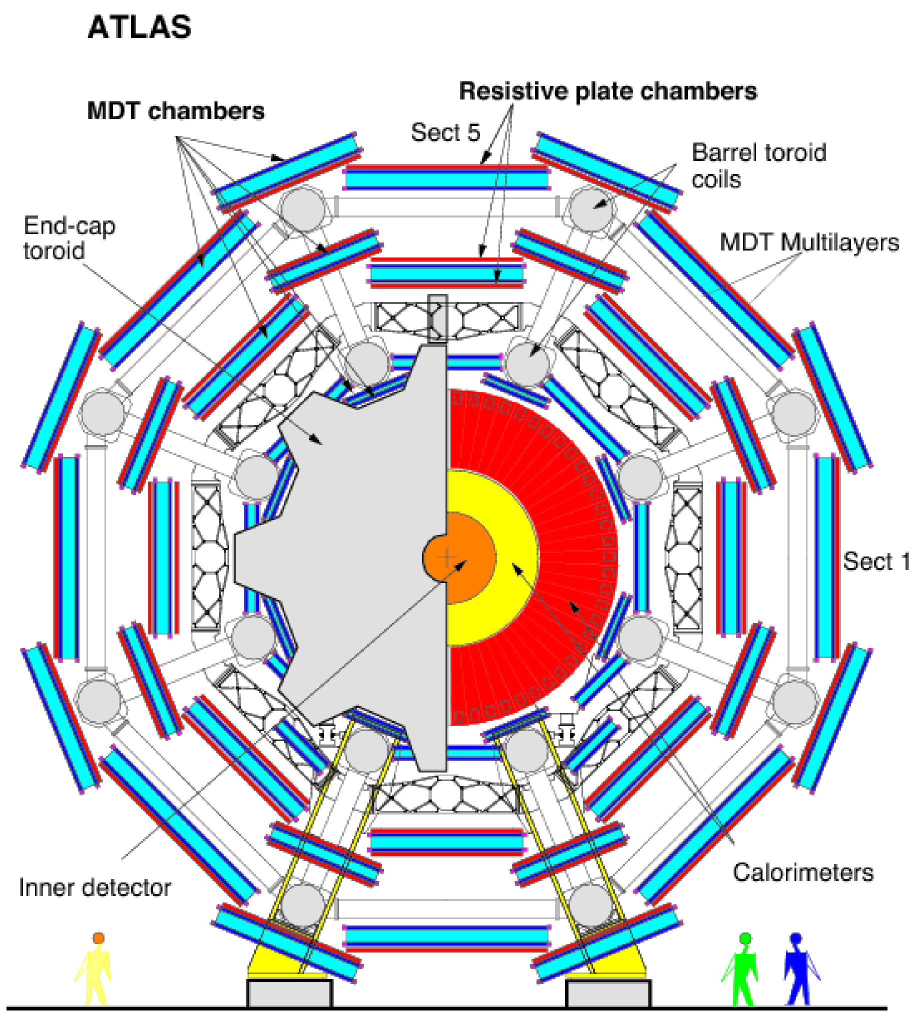

Figure 3.9: A diagram of of the Muon Spectrometer in the xy plane, showing the position of the Monitored Drift Tubes and Resistive Plate Chambers layers within the toroid magnets. [55]

and continuous magnetic field at the interface between between the two, and the end-caps toroids produce a magnetic field range 0.2 - 3.5 T.

3.2.6 Trigger System

The purpose of the ATLAS trigger system is to reduce the nominal LHC bunch crossing rate of 40 MHz, to a few hundred Hz. This is done by a three level trigger system. Level 1 (L1) is a hardware-based system that uses the information from the calorimeters and MS to reduce the rate to about 75 kHz. Level 2 (L2) and level 3 (which is known as the Event Filter, EF), are software-based systems that uses information from all the sub-detectors, and together they are known as the High-Level Trigger (HLT). L2 reduces the rate to a couple of kHz and the EF finally reduces the rate to a few hundreds Hz, with an event size of about 1.3 MB. All three levels of the trigger system are illustrated in Figure 3.10.

The L1 electronics must make a decision within 2.5 μs after the bunch crossing, making use of the RPC and TGC for muons, and the full set of calorimeters for electromagnetic clusters, jets, τ and $\mathrm{E}_T^{\mathrm{miss}}$. L1 triggers look for high p_T muons, electromagnetic clusters (electrons or photons), jets and τ lepton decays; they can also select events that have large missing transverse energy ($\mathrm{E}_T^{\mathrm{miss}}$).

L2 starts with Regions-of-Interest (RoI) that L1 identified as areas of the detector where the particles passed trigger thresholds. It uses all available information within the RoI to construct trigger objects with more precise measurements. These trigger objects are run through algorithms that try to locate predefined physical features, within the time scale of 40 ms. The trigger objects that pass the selection algorithms are built into events and then passed to the EF.

The EF takes the events passed from L2 and uses offline analysis procedures to perform finer selection and thus further reduce the rate, which takes about four seconds. Another function that the EF does is to classify the events according to data stream type. An event can exist in one or more streams. The defined stream types are: electrons, muons, jets, photons, $\mathrm{E}_T^{\mathrm{miss}}$, τ lepton and B-physics. The processor farm running the HLT software is located in a room adjoining the ATLAS detector cavern, in order to reduce latency.

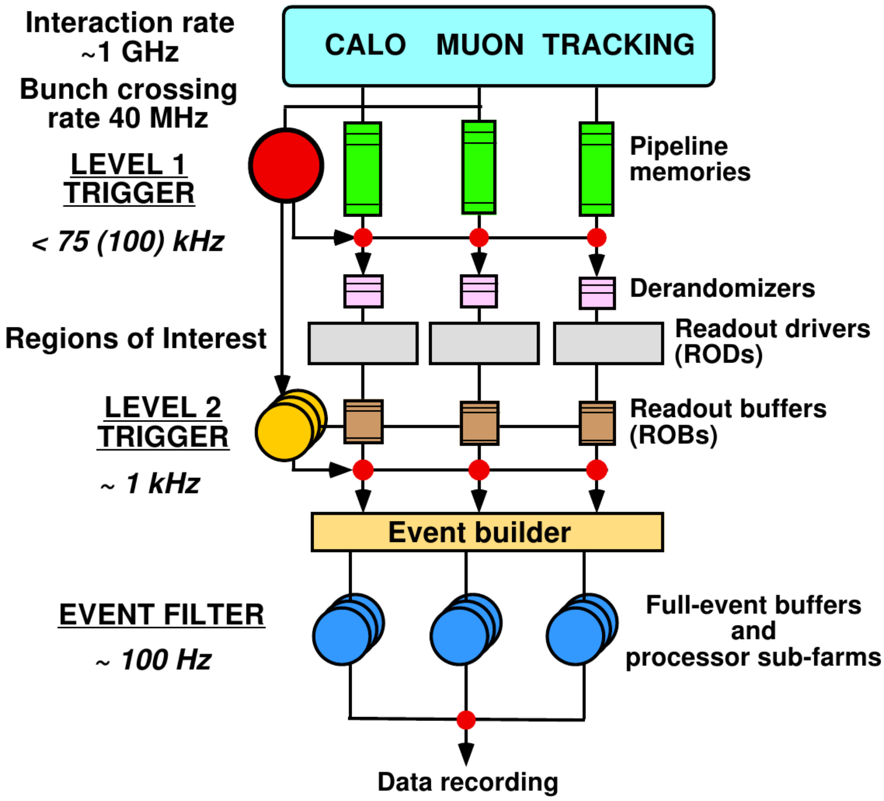

Figure 3.10: An illustration of the levels of the ATLAS trigger system. [56]

3.3 Data Distribution

The ATLAS detector will create a vast amount of data, on its own, not to mention the amount the other three experiments, which will also produce large amounts of generated and simulated data. In total the LHC will generate in the region of 15 petabytes a year, which is too much data for CERN to store and process, so the task of processing the data is shared using the Worldwide LHC Computer Grid (WLCG).

The WLCG is a global computer network that comprises four tiers. Tier 0 is the CERN Data Centre. This is the point where all the raw data from the LHC experiments flows through. It saves a copy of the raw data locally and sends another onto the Tier 1s. The Tier 1s consist of 11 computer centres spread across three continents, which store a share of the raw and the reconstructed data. The reconstructed data is then distributed to over 140 Tier 2s. The Tier 2s are research institutes and universities that have the computing power to run physics analysis over the reconstructed data. Tier 3s are local clusters or individual PCs that have been setup to allow scientist access to the WLCG [57].

On the WLCG there are different types of data, which are required for different levels of analysis. The type of data produced from the ATLAS experiment is classed as RAW and are about 1.6 MB per event. ESD (Event Summary Data) is the output of the reconstruction of the RAW data, intended to have all the necessary information for physics analysis, with a size 500 kB per event. AOD (Analysis Object Data) is a version of ESD with reduced event information, keeping objects of interest for physics analysis, and has a size of 100 kB per event. Another type of AOD is DAOD (Derived Analysis Object Data), which are created for physics analysis groups by adding or subtracting information, to make them more appropriate for that group's analyses. The final type of data store on the WLGC is group or user generated n-tuples for individual analyses. There is no fixed size for the last two types, as they vary as necessary [58].

Chapter 4

B-Physics Trigger

For this analysis the most important triggers are the B-physics di-muon triggers, which read from the muon stream. The B-physics triggers are extremely useful for quarkonium studies as they complement the muon triggers by focusing on the invariant mass range of the J/ψ, Υ, B mesons and the low mass di-muon region that ranges from below the J/ψ to above the Υ (DiMu). The regions the triggers cover are as follows:

- J/ψ (2.5 - 4.3 GeV), trigger name ending with **Jpsimumu**.
- B mesons (4 - 8.5 GeV), trigger name ending with **Bmumu**.
- Υ (8 - 12 GeV), trigger name ending with **Upsimumu**.
- DiMu (1.5 - 14 GeV), trigger name ending with **DiMu**.

These regions are illustrated in Figure 4.1 for the first half of 2011, with the 20 GeV single muon trigger plotted for comparison. The trigger names shown in Figure 4.1 start with the trigger level, then the muons p_T thresholds and the B-physics trigger region name, as defined in the list above. For example EF_2mu4_Jpsimumu, means it's an Event Filter trigger, which requires two muons to have $p_T > 4$ GeV in the J/ψ region. It can clearly be seen that all seven of the di-muon triggers shown (four triggers with both muons passing a 4 GeV

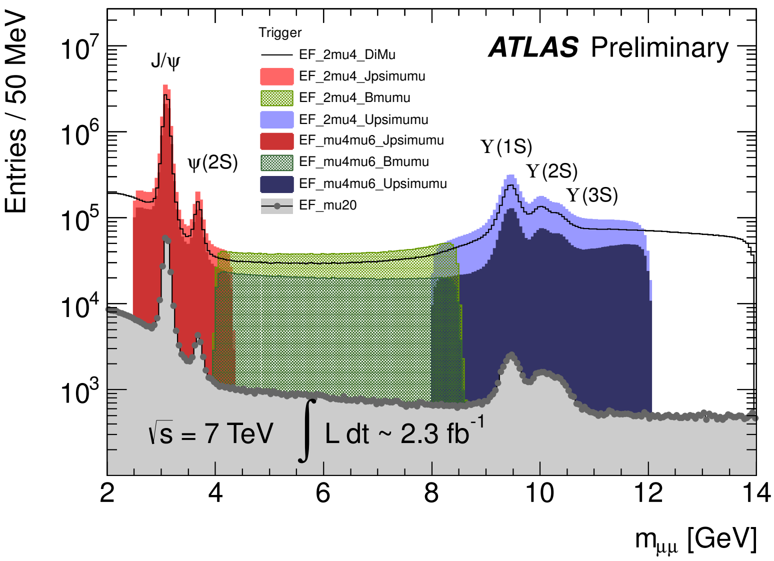

Figure 4.1: Di-muon invariant mass spectrum, showing the number of events passing the B-physics di-muon triggers for 2.3 fb^{-1} of 2011 data, compared with a single muon trigger [59].

threshold and three with one muon at 4 GeV and the other at 6 GeV) provide over an order-of-magnitude more events than the single muon trigger.

There are two types of B-Physics triggers, which are defined by either initially being triggered by a single muon (single RoI seeded) or a di-muon event (topological). Topological triggers require two L1 muons RoI, as can be seen in Figure 4.2a, after which both muons are confirmed separately in the HLT. Single RoI seeded triggers start with a single muon at L1 and then look for a second muon in the HLT, in a wide $\eta - \phi$ cone, around the triggered muon, as shown in Figure 4.2b.

The muon pairs found by the two techniques have to pass the following selection criteria: first that they are oppositely charged, pass the vertex fit quality required and that their invariant mass is within the trigger's range.

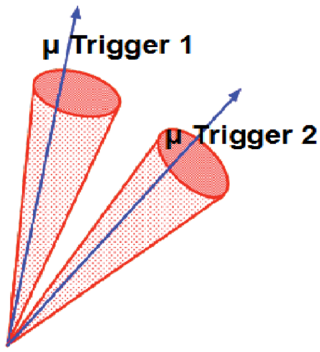

(a) Topological

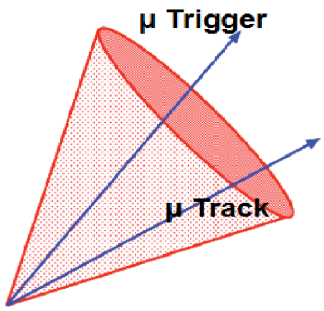

(b) Single Muon Trigger

Figure 4.2: Illustration of how the B-physics trigger algorithms identify di-muon events [60].

4.1 Data Taking

During data taking, changes will have to be occasionally made to the B-physics triggers, so that the rate from the trigger system doesn't increase beyond the allowed B-physics quota, which is around 10%. One of the ways to do this is increasing the p_T thresholds. This was done from the start of period L of 2011 onwards (run 188902, which started on the 7^{th} Sept), when the L1 threshold was increased to muons with $p_T > 4$ GeV; all the HLT names were changed to reflect this (mu4 changed to mu4T). Another way to reduce the rate is to narrow the region where the trigger is active; an example of this are the triggers that only look for muons in the barrel region of the detector. The most common way to reduce the rate is to increase the trigger's prescale, which means that randomly one in every predefined number of triggered events is selected and the rest of the events are ignored.

4.2 Trigger Monitoring

The B-physics triggers are monitored using the ATLAS trigger monitoring tools, which consist of an online and offline component. Majority of the histograms created by these components are only important for expert review, so only a small set of summary histograms are monitored by the trigger shifters. The author has spent time as both an online trigger shifter and an offline trigger expert.

4.2.1 Online Monitoring

Online monitoring takes place while a run is ongoing. During Run 1 of the LHC, ATLAS had two tools for this, the first was the Data Quality Monitoring Framework (DQMF), which used a series of tests to compare the current run histograms with a set of reference histograms. The reference histograms have to be manually extracted from a previous good run. The second is the Online Histogram Presenter (OHP), which does as the name implies, presents the current run histograms, with the reference histogram shown on top or by the side, but does not perform any comparison with the reference histograms.

4.2.2 Offline Monitoring

Offline monitoring is based on a web interface that allows for quick and easy monitoring, as automated checks colour code the histograms from the processed data streams. They are compared to a Centrally Managed Reference (CMR), which was updated about once a month with a high statistics run. Figure 4.3 shows examples of the histograms that need to be reviewed during a shift, in which the reference (shaded gray area) is scaled to the data (blue line). One of the useful features of the monitoring histograms, is that the mass peaks for the J/ψ and Υ can be seen in the relevant data streams.

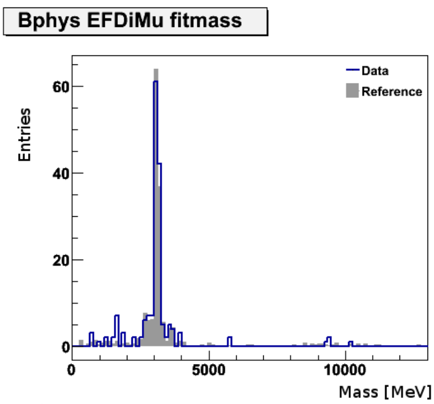

(a) Invariant mass of two muons, possibly forming resonance peaks. With only 1 required L2 muon starting from L1_MU*.

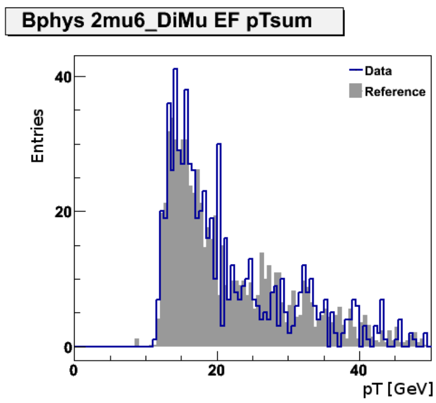

(b) Summed p_T distribution of two muons. With only 1 required L2 muon starting from L1_MU*.

Figure 4.3: Offline shifter monitoring histograms from run 203719.

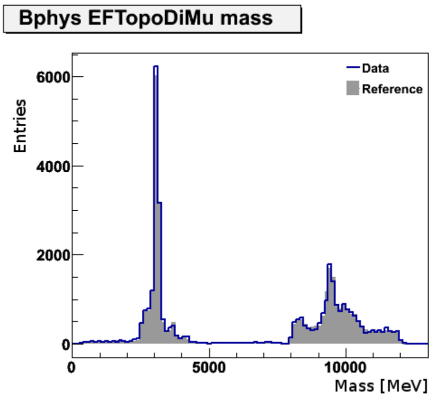

(c) Invariant mass of two muons, possibly forming resonance peaks. With 2 L1 muons.

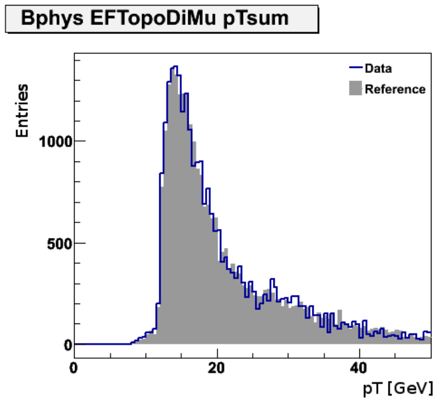

(d) Summed p_T distribution of two muons. With 2 L1 muons.

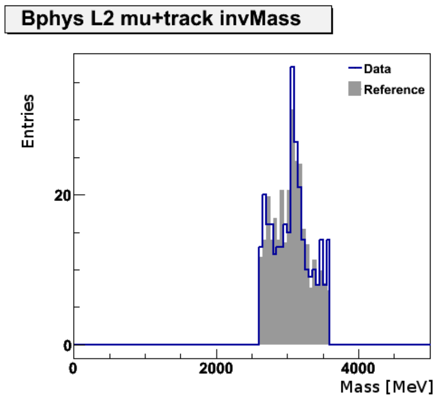

(e) Invariant mass of muon and a track, possibly forming resonance peaks.

Figure 4.3: Offline shifter monitoring histograms from run 203719 (Continued).

Chapter 5

$\psi(2S)$ Analysis

5.1 Data and Event Selection

Data for this analysis were taken during LHC proton-proton collisions at a centre-of-mass energy of 7 TeV from runs between data period B2 (22^{nd} March 2011) and K4 (21^{st} August 2011). Events had to pass the trigger EF_2mu4_Jpsimumu, which required two oppositely-charge muon candidates that satisfied a fit constraining the muons to originate from a common vertex while taking into account track parameter uncertainties and applying a loose selection on the vertex fit quality. This trigger was unprescaled for all of the periods that data were taken. This data selection resulted in a total integrated luminosity of 2.09$\pm$0.04 fb^{-1} [61]. The ψ(2S) is reconstructed using a similar technique as the B$_s \rightarrow$ J/$\psi\phi$ [62]. The two muon tracks from $J/\psi \rightarrow \mu^+\mu^-$ that can be fitted to a common vertex with a mass between 2.8 - 3.4 GeV, have their invariant mass constrained to the Particle Data Group value for the J/ψ (3.096916 GeV) [63].

The muon track parameters are taken from the ID measurement alone, since the MS does not add much to the precision in the lower momentum range relevant for the ψ(2S) measurements presented here. To ensure accurate inner detector measurements, each muon track must contain $\geq$ 6 silicon microstrip detector hits and $\geq$ 1 pixel detector hit. Muon candidates passing these criteria are required to have opposite-charges, with $p_T > 4$ GeV and $|\eta| < 2.3$ and a successful fit to

Table 5.1: The Muon Combined Performance (MCP) requirements applied to muon candidates.

No expected BLayer hit or number Of BLayer hits > 0
Number of pixel hits + number of crossed dead pixel sensors > 1
Number of SCT hits + number of crossed dead SCT sensors > 5
Number of pixel holes + number of SCT holes < 3
Let nTRThits denote the number of TRT hits on the muon track,
nTRToutliers the number of TRT outliers on the muon track,
and n = nTRThits + nTRToutliers
Case 1: $\|\eta\| < 1.9$. Require n > 5 and nTRToutliers < 0.9 n.
Case 2: $\|\eta\| \geq 1.9$. If n > 5, then require nTRToutliers < 0.9 n

a common vertex.

Good spatial matching, $\Delta R = \sqrt{(\Delta\eta)^2 + (\Delta\phi)^2)} < 0.01$, between each reconstructed muon candidate and the trigger identified candidates is required to accurately correct for trigger inefficiencies. For the other two tracks in the decay the pion mass hypothesis is used due to the lack of particle identification in ATLAS. The dataset containers are defined in Appendix A, in which the muons have already passed the ATLAS Muon Combined Performance (MCP) requirements, as given in Table 5.1. The selection criteria based on the number of hits within the ID for the assumed pion tracks are given in Table 5.2.

Table 5.2: Pion tracking quality selection requirements.

Cut	Condition
Number of B Layer hit	> 0
Number of Pixel hits	> 1
Number of BLayer + Pixel hits	> 1
Number of SCT hits	> 2
Number of Silicon hits	> 3

The various tracks and track combinations have to pass the selection criteria given in Table 5.3. The matching of the muons to the trigger and the selection of

$p_T > 8$ GeV (Table. 5.3) were investigated and found to have a negligible effect on the signal yield. Applying the selection requirement of the probability of χ^2 of the $J/\psi\pi\pi$ vertex fit, (Prob(χ^2)) is efficient in reducing the background, but has a measurable effect on the signal yield, the results of this investigation are shown in Table B.1 (Appendix B).

Table 5.3: Selection criteria for the muon tracks, pion tracks, di-muons, di-pions and $J/\psi\pi\pi$ candidates

μ	π
$p_T > 4$ GeV	$p_T > 0.5$ GeV
$\lvert\eta\rvert < 2.3$	$\lvert y\rvert < 2.5$
Oppositely Charged	Oppositely Charged
Both Combined Muons	
MCP Cuts	

$\mu\mu$	$J/\psi\pi\pi$
$\chi^2 < 200$	Prob(χ^2) > 0.005
$p_T > 8$ GeV	
$\lvert\eta\rvert < 2.0$	
$2.8 < \mathrm{m}_{\mu\mu} < 3.4$	

5.1.1 Binning

The constrained vertex fit allows for significantly improved invariant mass resolution for the $J/\psi\pi\pi$ system over what would be expected from momentum resolution alone, so it is possible to focus in on the narrow mass region 3.586 GeV $< \mathrm{m}_{J/\psi\pi\pi} <$ 3.786 GeV. The results are plotted in three rapidity regions, the same as the first three used in the J/ψ analysis [26], which were:

$$0 < |y| < 0.75,\ 0.75 < |y| < 1.5,\ 1.5 < |y| < 2.0.$$

Figure 5.1 illustrates the raw yields and the resolutions of the di-muons (top row) and the $J/\psi\pi\pi$ system (bottom row) in the three rapidity regions, which comprise about 94,000, 64,000 and 39,000 ψ(2S) candidates respectively. For the di-muon invariant mass fits a double Gaussian is used to describe the signal

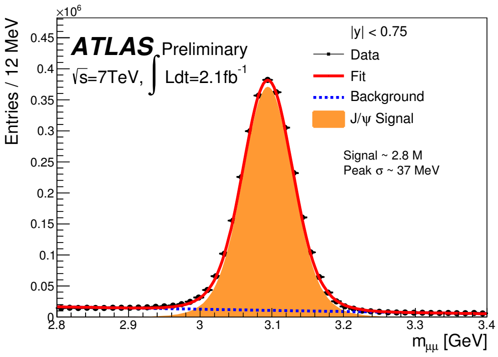

(a) $\mu\mu$, $|y| < 0.75$

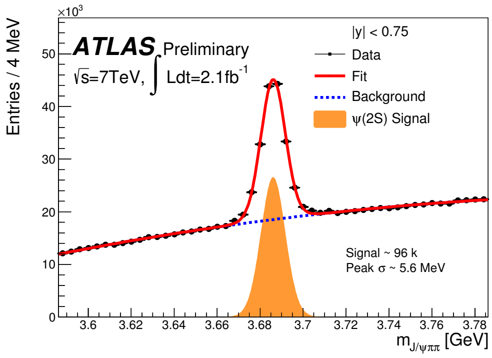

(b) $J/\psi\pi\pi$, $|y| < 0.75$

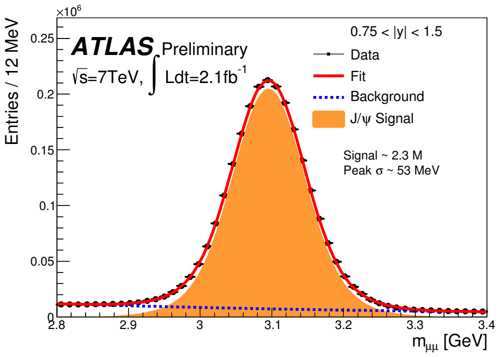

(c) $\mu\mu$, $0.75 < |y| < 1.5$

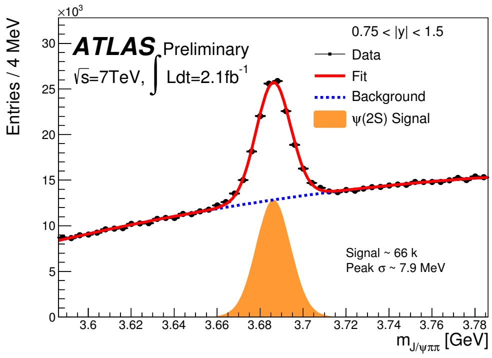

(d) $J/\psi\pi\pi$, $0.75 < |y| < 1.5$

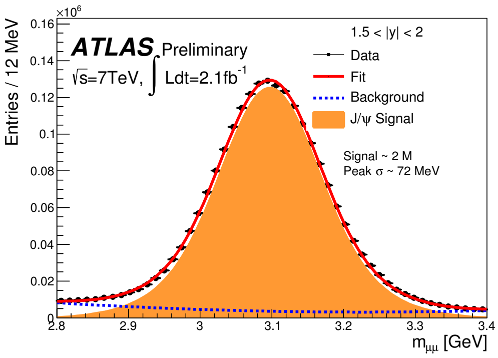

(e) $\mu\mu$, $1.5 < |y| < 2.0$

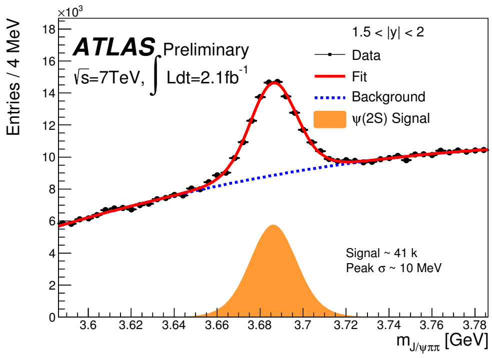

(f) $J/\psi\pi\pi$, $1.5 < |y| < 2.0$

Figure 5.1: An illustration of fitted mass peaks of the unweighted di-muon (a,c,e) and $J/\psi\pi\pi$ candidates (b,d,f).

peak, and a 2nd-order Chebyshev polynomial to model the background. For the $J/\psi\pi\pi$ distribution a single Gaussian describes the signal shape, and a 2nd-order Chebyshev polynomial to parameterise the background. The 2-dimensional distribution in transverse momentum (p_T) and absolute rapidity $|y|$ of all $J/\psi\pi\pi$ candidates contributing to Figure 5.1 is shown in Figure 5.2. In each of the three rapidity ranges, the events were further split into a number of p_T bins with the following bin boundaries: 10–11, 11–12, 12–14, 14–16, 16–18, 18–22, 22–30, 30–40, 40–60, 60–100 GeV.

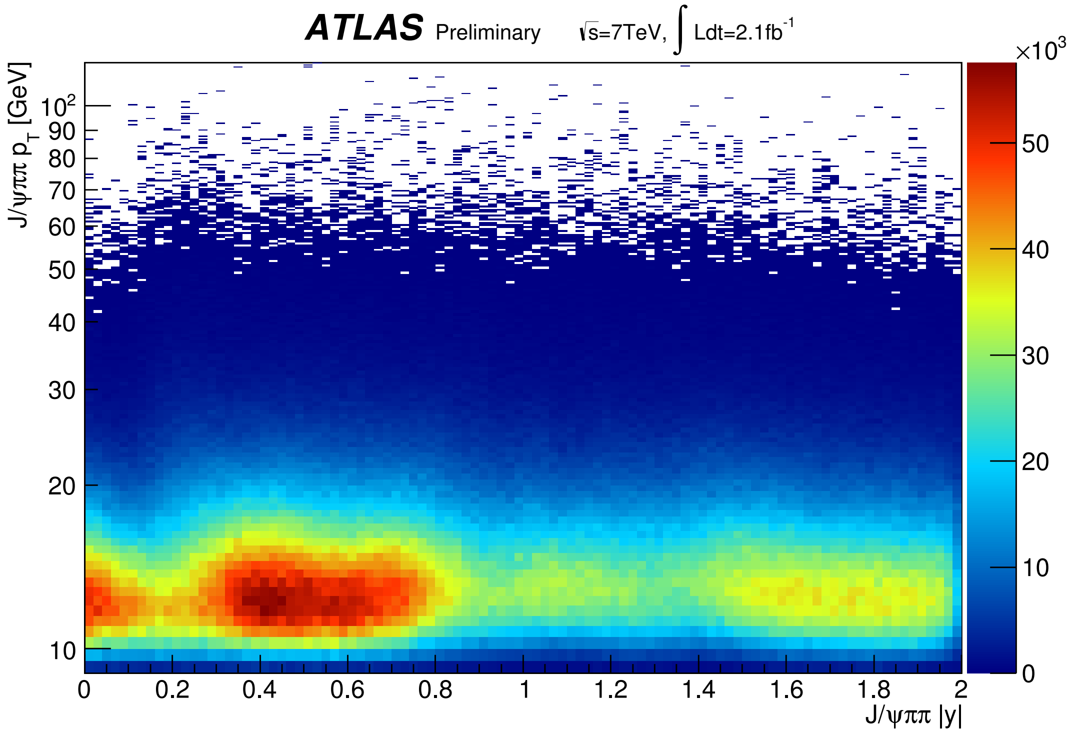

Figure 5.2: 2D Map of all events passing selection criteria within the mass region 3.586 GeV $<$ $\mathrm{m}_{\mathrm{J}/\psi\pi\pi}$ $<$ 3.786 GeV. Each bin in this histogram corresponds to $\Delta p_T = 0.5\ GeV$ and $\Delta|y| = 0.02$.

5.2 Cross-Section Determination

There are two sets of cross-sections that need to be determined, one set for the prompt and one for the non-prompt $\psi(2\mathrm{S})$. The prompt $\psi(2\mathrm{S})$ has no significant "feed down" from higher mass charmonium states, since it is just below the $D\bar{D}$ threshold. The non-prompt $\psi(2\mathrm{S})$ are distinguished from prompt processes by their long lifetimes, through the decay via a b-hadron. Since in this analysis the b-hadron is not fully reconstructed, it is not possible to use its lifetime. Instead a parameter called pseudo-proper lifetime τ is constructed using the $J/\psi\pi\pi$ transverse momentum:

$$\tau = \frac{L_{xy} m^{\mathrm{J}/\psi\pi\pi}}{P_T^{\mathrm{J}/\psi\pi\pi}} \tag{5.1}$$

L_{xy} is defined by the equation:

$$L_{xy} \equiv \vec{L} \cdot \vec{p}_T(\mathrm{J}/\psi\pi\pi)/p_T(\mathrm{J}/\psi\pi\pi), \tag{5.2}$$

where $\vec{L}$ is the vector from the primary vertex to the $J/\psi\pi\pi$ decay vertex and $\vec{p}_T^{\mathrm{J}/\psi\pi\pi}$ is the transverse momentum vector of the $J/\psi\pi\pi$.

To obtain the cross-section measurement, firstly the observed candidates are individually weighted to correct for detector effects, such as acceptance, muon reconstruction efficiency, pion reconstruction efficiency and trigger efficiency. Afterwards the distribution of candidates in each p_T and $|y|$ bin is fitted using a weighted 2D unbinned maximum likelihood method, which was performed on mass and pseudo proper lifetime. The corrected prompt and non-prompt signal yields ($N_{(\mathrm{P})}^{\psi(2\mathrm{S})}$, $N_{(\mathrm{NP})}^{\psi(2\mathrm{S})}$) are then used to calculate the differential cross-sections, using the equation:

$$Br\left(\psi(2\mathrm{S}) \to J/\psi(\mu^+\mu^-)\pi^+\pi^-\right) \times \frac{d^2\sigma(\psi(2\mathrm{S}))}{dp_T dy} = \frac{N_{(\mathrm{P/NP})}^{\psi(2\mathrm{S})}}{\Delta p_T \Delta y \int \mathcal{L} dt} \tag{5.3}$$

where $\int \mathcal{L}\mathrm{d}t$ is the total integrated luminosity, Δp_T and Δy are the bins sizes in $\psi(2\mathrm{S})$ transverse momentum and rapidity, respectively.

The non-prompt fraction is defined to be the corrected number of non-prompt ψ(2S) divided by the corrected total number of produced ψ(2S), as seen in the equation:

$$f_B^{\psi(2\mathrm{S})} \equiv \frac{N_{\mathrm{NP}}^{\psi(2\mathrm{S})}}{N_{\mathrm{P}}^{\psi(2\mathrm{S})} + N_{\mathrm{NP}}^{\psi(2\mathrm{S})}}. \tag{5.4}$$

The fraction has the advantage that acceptances and some efficiencies are the same for the numerator and denominator, and so it removes the uncertainties from luminosity and ID tracking efficiency.

5.2.1 Acceptance

The acceptance $\mathcal{A}$ is defined as the probability that the decay products in $\psi(2\mathrm{S}) \to \mathrm{J}/\psi(\to \mu^+\mu^-)\pi^+\pi^-$ fall within the fiducial volume of the detector, $p_T^\mu > 4$ GeV and $|\eta^\mu| < 2.3$, $p_T^\pi > 500\ MeV$ and $|\eta^\pi| < 2.5$. It has been shown [37] that the spin states of the pions in the di-pion system, and the di-pion system with respect to the J/ψ are heavily dominated by their respective S-waves. Hence, no angular dependence is expected for these systems, and the polarisation state of the ψ(2S) is directly transferred to the J/ψ. The acceptance depends on the spin alignment of the ψ(2S). For the central results obtained in this analysis, the ψ(2S) was assumed to be isotropic, with variations corresponding to a number of extreme spin alignment scenarios detailed below.

The acceptance maps are created using a high statistics generator-level Monte Carlo simulation, which randomly creates and decays ψ(2S), as a function of p_T and rapidity of the ψ(2S), in fine bins of the di-pion invariant mass $m_{\pi\pi}$, covering the allowed range, $2m_\pi < m_{\pi\pi} < M_{\psi(2\mathrm{S})} - M_{\mathrm{J}/\psi}$. Examples of the acceptance maps, for two extreme values of $m_{\pi\pi}$, are shown in Figure 5.3, and the ratio between them. In Figures 5.3a and 5.3b it is shown that there is a smooth increase in acceptance over p_T in the region $|y| < 2.0$, so that it is $\sim$ 100% at 100 GeV. As expected the acceptance reaches zero at 8 GeV and $|y| \approx$2.4. Figures 5.3c shows that as $m_{\pi\pi}$ increases there is slight change to the acceptance in the region $10 < p_T < 30$ GeV and $|y| < 2.0$, but the most dramatic changes occur in the acceptance regions not used in this analysis. Examples of the six anisotropic cases can been found in Appendix C.

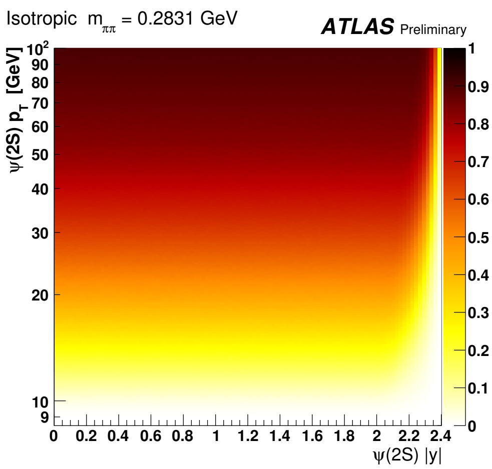

(a) Lowest di-pion bin

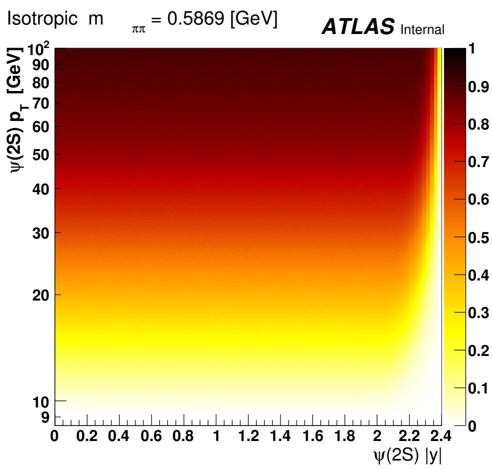

(b) Highest di-pion bin

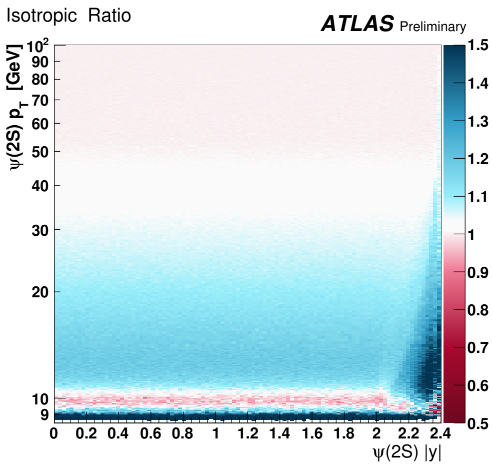

(c) Ratio

Figure 5.3: isotropic acceptance map is a 3D plot of $|y|$, p_T and $m_{\pi\pi}$. Shown in (5.3a) and (5.3b) is the 2D ($|y| - p_T$) slice of the lowest and highest di-pion mass.

Figure 5.4 illustrates the variation of the acceptance correction weights with p_T and rapidity, for the seven scenarios described above, relative to the isotropic case.

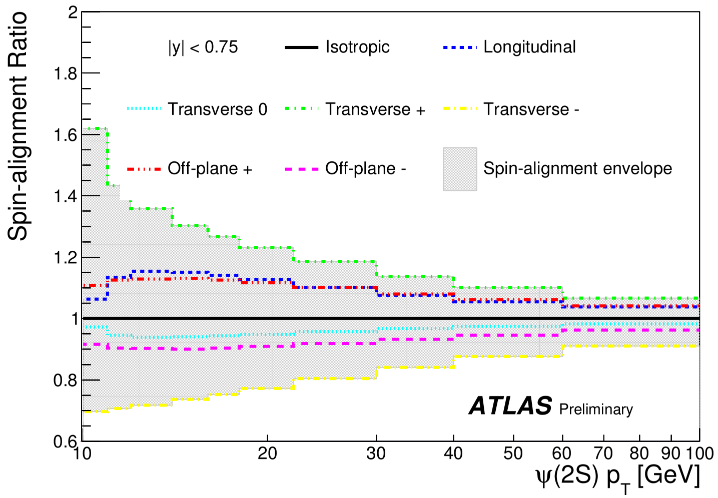

(a) $|y| < 0.75$

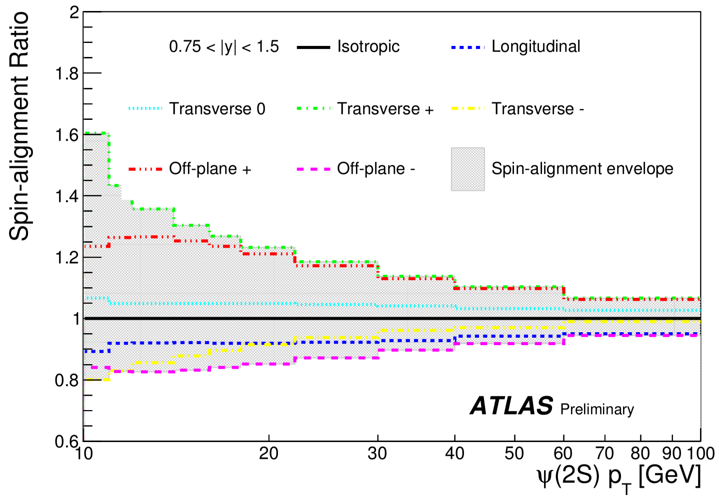

(b) $0.75 < |y| < 1.5$

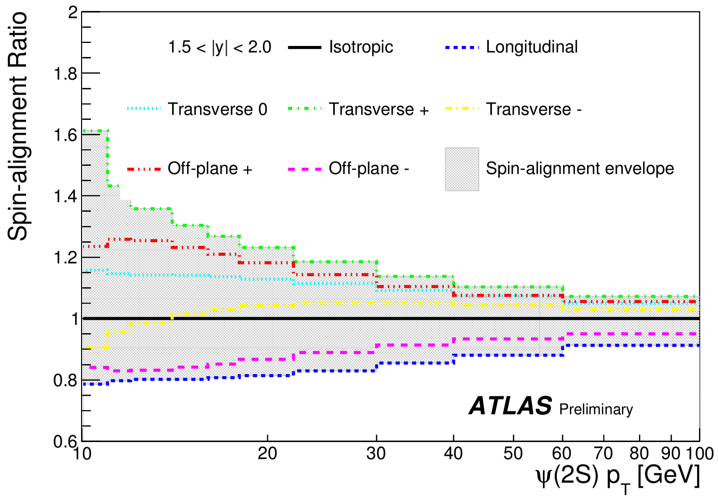

(c) $1.5 < |y| < 2.0$

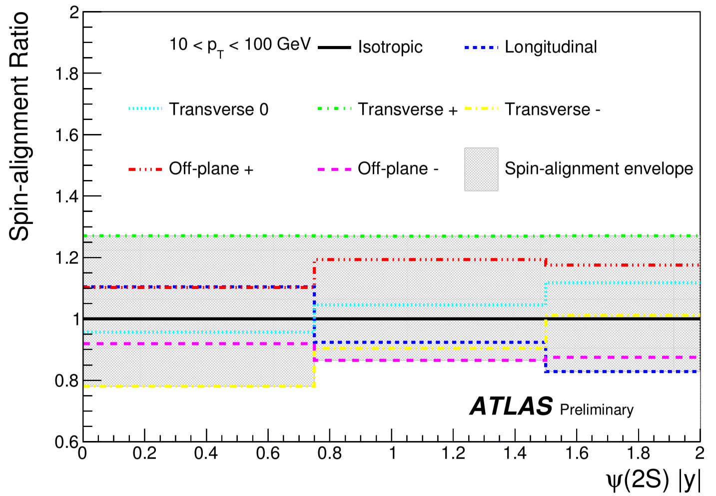

(d) $10 < |p_T| < 100$

Figure 5.4: Average acceptance correction relative to isotropic scenario for the seven extreme polarisation scenarios described in the text, versus p_T for the three rapidity regions (a,b,c) and versus rapidity, integrated over p_T (d).

5.2.2 Muon Reconstruction

As this analysis uses the same data with the same selections as in Ref. [64] the same muon reconstruction efficiency map, created for the $\Upsilon \to \mu^+\mu^-$ cross-section measurement, can be re-used without any modifications. The muon reconstruction efficiency is given by:

$$\epsilon_{reco} = \epsilon_{trk}(p_{\mathrm{T}1}, \eta_1) \cdot \epsilon_{trk}(p_{\mathrm{T}2}, \eta_2) \cdot \epsilon_{\mu}(p^{\mu}_{\mathrm{T}1},\, q_1 \cdot \eta^{\mu}_1) \cdot \epsilon_{\mu}(p^{\mu}_{\mathrm{T}2},\, q_2 \cdot \eta^{\mu}_2), \tag{5.5}$$

where q is the charge of the muon, ϵ_{trk} is the efficiency between the muon and a ID track, which was determined to be 99±1.0%, also obtained from [64]. Here, ϵ_{μ} is the efficiency to reconstruct a muon, which is extracted from the data by using the tag and probe method on $J/\psi \to \mu^+\mu^-$ events. A *tag* muon is a combined muon that is within the acceptance region $p_T > 4$ GeV and $|\eta| < 2.5$ and must have fired a single muon trigger. A *probe* track needs to pass the ID quality cuts, $p_T > 4$ GeV and $|\eta| < 2.5$ cuts and also have the same vertex as the *tag* muon.

After this the *probe* track is attempted to be matched to a combined muon. The resulting J/ψ candidates are then separated according to the p_T and $(q \cdot \eta)$ of the probe muon, and these distributions were then fitted. The single muon reconstruction efficiency is then defined as the ratio of J/ψ yields of events where the *probe* tracks are correctly matched to the J/ψ yield of all the *probe* tracks.

5.2.3 Pion Reconstruction Efficiency

The pion reconstruction efficiency map (Figure 5.6) was created using the same technique defined in existing track efficiency measurements, an example of which can be found in [65]. A sample of MC11 simulation was used to generate the map, by applying acceptance selection cuts to the generated charged tracks, which were $p_T > 0.5$ GeV and $|\eta| < 2.5$. These same acceptance selection cuts are also applied to the reconstructed track, as well as the tracking hit selection quality cuts, as shown in Table 5.2.

The track reconstruction efficiencies are calculated in bins of $(q \cdot \eta)$ and p_T^{trk}. In addition to the error due to the simulation statistics, each bin also contains an additional uncertainty term, which covers the discrepancy between MC and data,

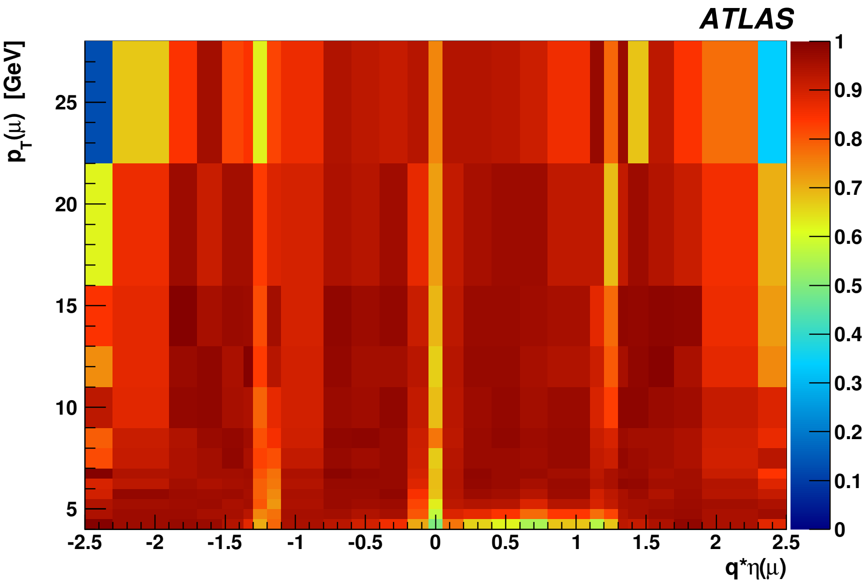

Figure 5.5: Muon reconstruction efficiency map, obtained from [64].

and is documented in Table 4 of the track reconstruction efficiency paper [66]. The track reconstruction efficiency is calculated by using the following equation:

$$\epsilon_{trk} = \frac{N_{\text{reco}}^{\text{matched}}}{N_{\text{gen}}} \tag{5.6}$$

where $N_{\text{reco}}^{\text{matched}}$ is the number of reconstructed tracks that have been matched to a same charged generated particle and N_{gen} is the number of generated particles that have passed the acceptance cuts. Matching between the generated particle and reconstructed track is done by using the cone matching algorithm in $\Delta R = \sqrt{(\Delta\phi)^2 + (\Delta\eta)^2}$. A match is defined as the reconstructed track with the smallest ΔR being within the cone radius of 0.05. The results of tests performed on the generation of the pion reconstruction efficiency can be found in Appendix D.

5.2.4 Trigger Efficiency

The EF_mu4 trigger efficiency maps were also created for the $\Upsilon \rightarrow \mu^+\mu^-$ cross-section measurement [64]. The trigger efficiency was determined from data, using

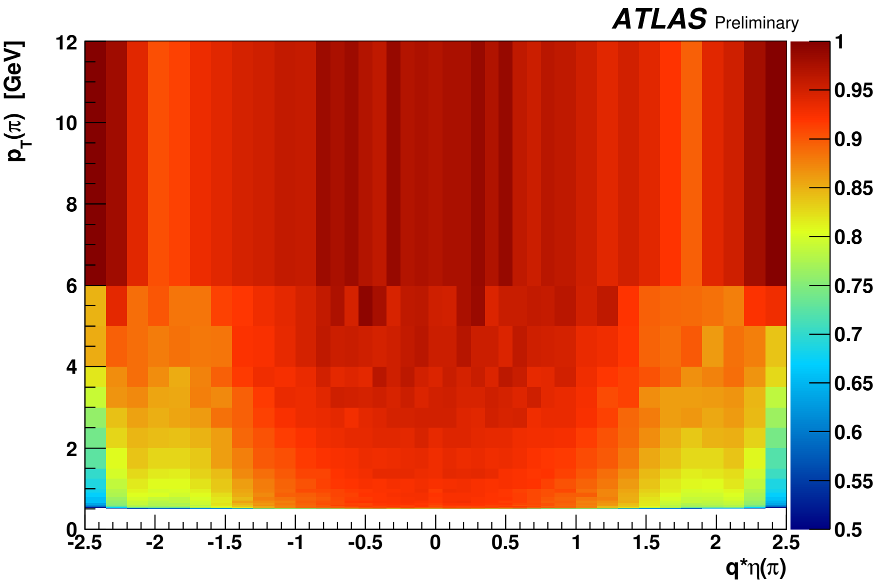

Figure 5.6: Pion reconstruction efficiency map, as function of pion charge-signed pseudorapdity and transverse momentum, obtained from simulation.

the following triggers:

- `EF_mu18` ,
- `EF_2mu4_DiMu_NoVtx_NoOS` and
- `EF_2mu4_DiMu`.

The only difference between EF_2mu4_DiMu and the trigger used in this analysis, EF_2mu4_Jpsimumu, is that it sub-selects a smaller invariant mass range. The trigger efficiency is given by:

$$\epsilon_{\text{trig}} = \epsilon_{\text{ROI}}(p_T^+, q_1, \eta^+) \cdot \epsilon_{ROI}(p_T^-, q_2, \eta^-) \cdot c_{\mu\mu}(\Delta R, |y_{\mu\mu}|) \tag{5.7}$$

where ϵ_{ROI} is the efficiency of the trigger system to find a Region of Interest (ROI) for a single muon and $c_{\mu\mu}$ is a correction term for the effects related to the di-muon components of the trigger. The factor $c_{\mu\mu}$ was calculated in three di-muon rapidity regions: barrel ($|y_{\mu\mu}| < 1.0$), barrel-endcap ($1.0 < |y_{\mu\mu}| < 1.2$), endcap ($1.2 < |y_{\mu\mu}| < 2.25$). This is due to the trigger behaving differently in each of these regions:

$$c_{\mu\mu} = c_a(y_{\mu\mu}) \cdot c_{\Delta R}(\Delta R, y_{\mu\mu}). \tag{5.8}$$

The first component $c_{\mu\mu}$ is the asymptotic value c_a, which is caused by the vertex and opposite sign requirement and is defined by the maximum efficiency for large di-muon angular separation. The second component of $c_{\mu\mu}$ is the spatial separation of the two muons $c_{\Delta R}$, which is caused by the two muons needing a large enough ΔR, so that they are identified as two separate RoIs.

Due to a change in the trigger algorithm during the data-taking period, two separate trigger efficiency maps are computed, which are illustrated in Figure 5.7.

5.2.5 Bin Migration Corrections

In order to account for bin migrations due to finite detector resolution, corrections in $\mathrm{p}_T(\mathrm{J}/\psi\pi\pi)$ are derived by comparing analytic functions fit to the $\mathrm{p}_T(\mathrm{J}/\psi\pi\pi)$ spectra of $\psi(2\mathrm{S})$ events in data, with and without convolution by the $\mathrm{p}_T(\mathrm{J}/\psi\pi\pi)$ resolution (determined from the fitted mass resolution and measured muon angular resolutions). These corrections factors are found to be no larger than $\mathcal{O}(10^{-4})$ across the range of p_T and rapidities and therefore no correction is required, and no systematic uncertainty need be considered.

5.2.6 Total Weight

The total weight w for each $J/\psi\pi\pi$ candidate was calculated as the inverse product of acceptance and efficiencies, as described by:

$$w^{-1} = \mathcal{A} \cdot \epsilon_{trk} \cdot \epsilon^{+}_{\mu}(p^{+}_{T}, \eta^{+}) \cdot \epsilon^{-}_{\mu}(p^{-}_{T}, \eta^{-}) \cdot \epsilon^{+}_{\pi}(p^{+}_{T}, \eta^{+}) \cdot \epsilon^{-}_{\pi}(p^{-}_{T}, \eta^{-}) \cdot \epsilon_{trig}, \tag{5.9}$$

where the acceptance $\mathcal{A}$ is parameterised in terms of the p_T and $|y|$ of the $\psi(2\mathrm{S})$, and the di-pion invariant mass, as described in Sec. 5.2.1. The other efficiency

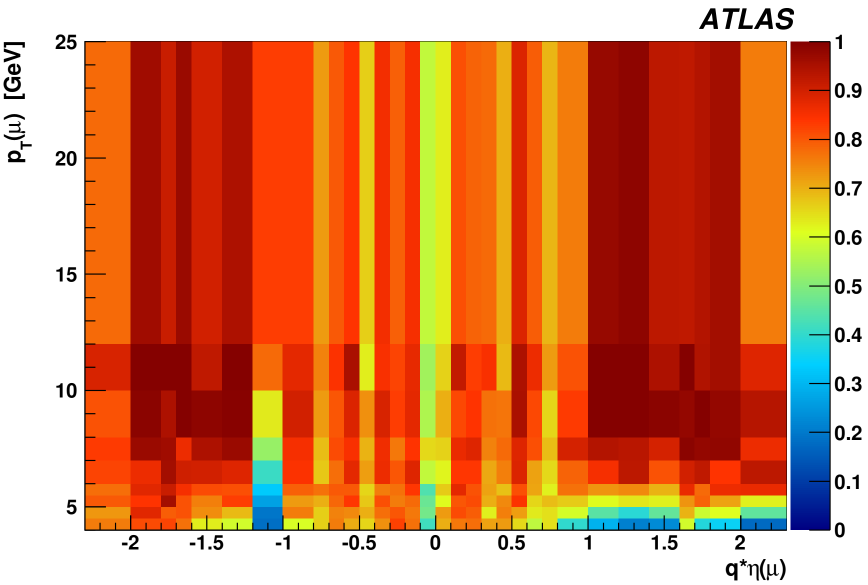

(a) Before Period H 2011

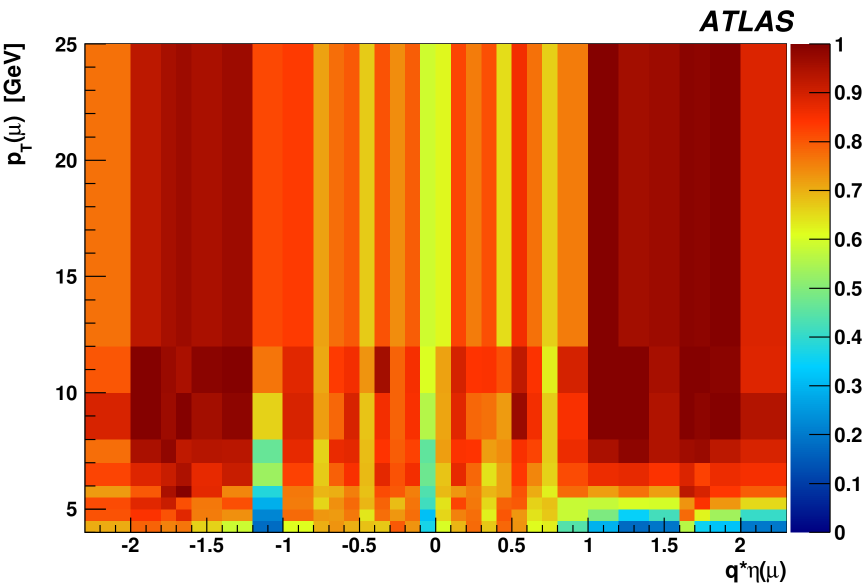

(b) After Period H 2011

Figure 5.7: Trigger reconstruction efficiency map, obtained from [64].

corrections for ϵ_{trk}, ϵ_{μ}, ϵ_{π} and ϵ_{trig} have been discussed above, and shown in Figs. 5.5, Fig. 5.6 and Fig. 5.7, respectively.

The average of the total weight and its component breakdown is illustrated by Fig. 5.8, shown for the three rapidity regions versus p_T and one for the average of the full p_T versus rapidity.

5.3 Fitting Procedure

A 2-dimensional weighted unbinned maximum likelihood fit is performed on the $J/\psi\pi\pi$ invariant mass and pseudo proper lifetime for each of the p_T and $|y|$ bins, where the fit model was defined by the Probability Density Function (PDF), which was defined as a normalised sum of terms, where each term is factorized into a mass-dependent and lifetime-dependent function. The PDF can be written in a compact form as:

$$\mathrm{PDF}(m,\tau) = \sum_{i=1}^{5} \oplus f_i(m) \cdot h_i(\tau) \otimes G(\tau). \tag{5.10}$$

Here the symbol $\oplus$ stands for a normalised sum of various terms, which is needed to modify the way the terms in the sum are added to each other, while $\otimes$ denotes a convolution between two functions. The functions f_i and h_i for the various terms of the sum, $i = 1, \ldots, 5$ are shown in Table 5.4, where G_k, C_k, and E_k stand for Guassians, 2-nd order Chebyshev polynomials and exponential functions, respectively, with different values of the index k corresponding to different sets of parameters, while δ stands for the Dirac delta function.

In Table 5.4 $\mathrm{G_1(m)} \oplus \mathrm{G_2(m)}$ represents the use of a double Gaussian to fit the signal, in which the Gaussians share the same mean. There are two non-prompt background terms (4,5), because one term models the positive component of the non-prompt background lifetime (term 4), and the other models the negative component of the non-prompt background lifetime (term 5), which is caused by

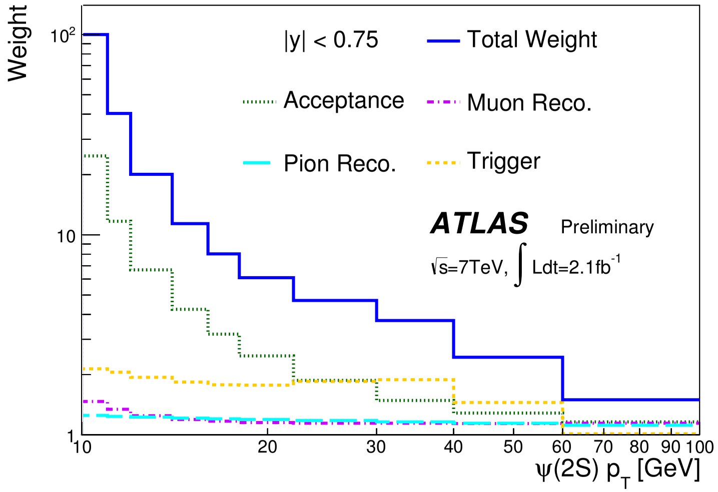

(a) $|y| < 0.75$

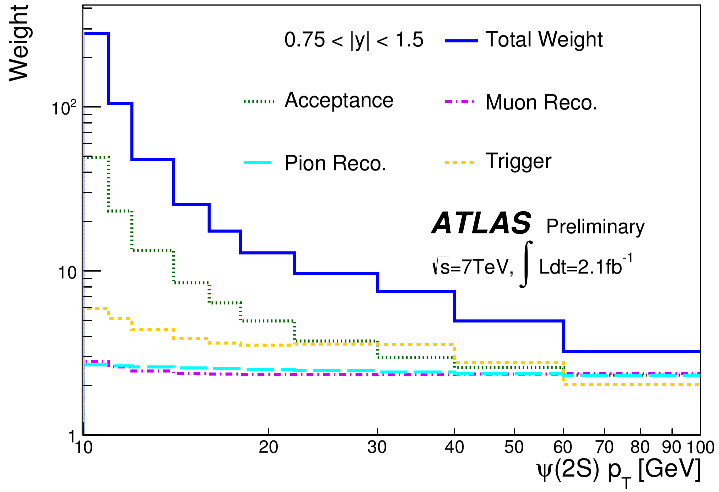

(b) $0.75 < |y| < 1.5$

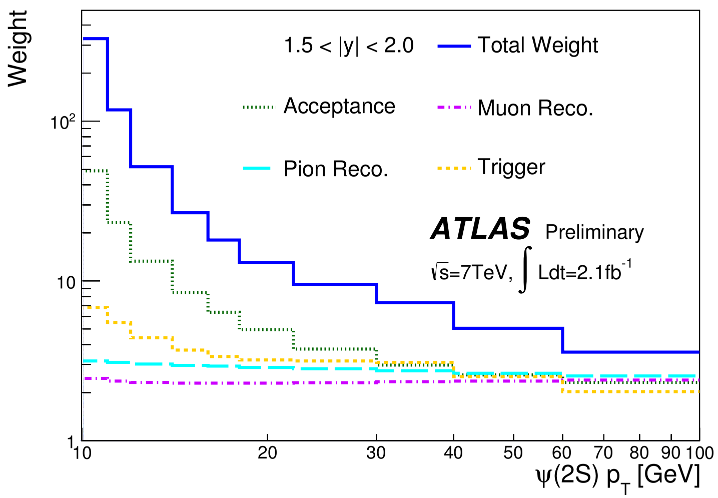

(c) $1.5 < |y| < 2.0$

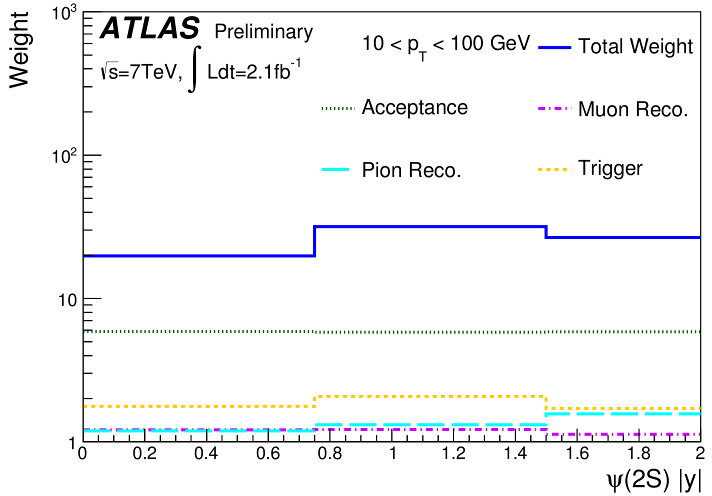

(d) $10 < |p_T| < 100$

Figure 5.8: Average weights for the three rapidity regions versus p_T (a,b,c) and for the full p_T region versus $|y|$ (d).

Table 5.4: Components of the PDF

i	Type	Source	$f_i(m)$	$h_i(\tau)$
1	Signal	Prompt	$\mathrm{G}_1(\mathrm{m}) \oplus \mathrm{G}_2(\mathrm{m})$	$\delta(\tau)$
2	Signal	Non-prompt	$\mathrm{G}_1(\mathrm{m}) \oplus \mathrm{G}_2(\mathrm{m})$	$\mathrm{E}_1(\tau)$
3	Background	Prompt	$\mathrm{C}_1(\mathrm{m})$	$\delta(\tau)$
4	Background	Non-prompt	$\mathrm{C}_2(\mathrm{m})$	$\mathrm{E}_2(\tau)\oplus\mathrm{E}_3(\tau)$
5	Background	Non-prompt	$\mathrm{C}_3(\mathrm{m})$	$\mathrm{E}_4(\lvert\tau\rvert)$

detector smearing. The lifetime resolution function, $G(\tau)$,is a Gaussian, whose mean is fixed to zero, and with a width that is free to be determined from the fit.

To better constrain the fit model at high p_T, the widths (σ) of the mass signal Gaussians (for prompt and non-prompt) are obtained from separate fits to the invariant mass distributions, using the same $f_i(m)$ terms. For each rapidity slice, the fit was performed to the measured widths as a function of p_T. In the full fitting procedure, the value of each σ is constrained to the value determined by the parameterisations. The results of the individual fits to the widths, and fitted parameterisations are shown in Figure E.1 (Appendix E).

Chapter 6

Results and Systematics

6.1 Systematic Uncertainties

6.1.1 Acceptance

The acceptance maps were generated using using high statistics Monte Carlo, with negligible statistical uncertainties. Other effects, such as smearing of the primary vertex position within the known beam spot, were studied and found to yield a negligible effect.

6.1.2 Reconstruction and Trigger Efficiencies

The systematics related to the muon reconstruction efficiency, pion reconstruction efficiency and trigger efficiency corrections were determined by using pseudo-experiments: for each map, the value in every bin is randomly varied within its uncertainty, thus creating a set of new efficiency maps, which are used one at a time to recalculate the total weight. The new total weights are then used to produce a new set of fit results. This was done 50 times for each of the three maps. The fit yields for each p_T and $|y|$ bin were plotted and fitted with a Gaussian, the width of which was used as the respective systematic uncertainty.

In addition to variations of the pion map efficiency terms, additional uncertainties exist, relating to data/MC discrepancies and uncertainties of hadronic interactions [66]. The data / MC differences are estimated to be 2%–3% per pion in the p_T ranges considered, which varies with rapidity, and a 1% contribution per pion for the hadronic uncertainty. As a conservative estimate, the two pions are treated coherently and the uncertainty due to each pion combined linearly. The total pion uncertainty is then the quadrature sum of the: pion efficiency map, Data/MC difference, and hadronic interactions uncertainties.

6.1.3 Fit Model Variations

The uncertainty on the fit was determined by changing one component at a time of the fit model described in Section. 5.3, creating a set of new fit models. For each new fit model the cross-section was calculated, and in each p_T and $|y|$ bin the maximum difference from the central fit model was used as its systematic uncertainty. In this case the central fit model is the double Gaussian mass signal and 2^{nd} order Chebyshev polynomial for mass background (Model 2 in Table 6.1). The full set of fit models used are described by Table 6.1. where G, C and E are

Table 6.1: Fit models used to test sensitivity of extracted $\psi(2S)$ yields to the signal and background modelling. The symbols are described in the text.

i	Signal	Background
0	DG(Fit σ_1&σ_2)	C
1	G(Free σ)	C
2	G(Fit σ)	C
3	DG(Fit σ_1&σ_2)	L
4	CB(Fit σ, Fixed α & n)	C
5	DG(Fit σ_1&σ_2)	C (τ background reduce to 1 E)

the same as defined in Section 5.3. DG is a double Gaussian, CB is a crystal ball function [67, 68, 69], with the α and n parameters fixed to 2 (determined from test fits), L is a linear Chebyshev polynomial, Fit σ is the result of the fitted σ (defined in Appendix E) and Free σ is when the σ is completely free. For all these models the lifetime component was varied by modifying the exponential terms for the background. The full set of cross-section variations for the models is shown in Appendix F.

6.1.4 Luminosity

The uncertainty in the luminosity is defined by the ATLAS Luminosity Group and for 2011 they determined a luminosity uncertainty of 1.8% [61].

6.1.5 Fit Results

For all bins of each of the fit models the goodness of fit (χ^2/ndf) was calculated using the fit results and the mass and pseudo-proper lifetime distributions, which are shown in Table E.1 (Appendix E). Shown in Figure 6.1 are examples of a low p_T and central $|y|$ bin, a mid-range p_T and transition $|y|$ bin and a high p_T and end-cap $|y|$ bin. For the three examples there is also the projection slices in mass and lifetime which are shown in Appendix E.

6.1.6 Selection Criteria

For the constrained $J/\psi\pi^+\pi^-$ fit quality cut, the efficiency was measured to vary between 93% and 97% as a function of p_T, with an uncertainty of about 2% estimated from the bin-to-bin variation of the efficiency. Other selection inefficiencies and their corresponding uncertainties were estimated using simulations to be at or below the 1% level. The systematic error on the selection efficiency was obtained by summing in quadrature all uncertainties.

6.1.7 Total Systematic Uncertainties

The summary of the statistical and systematic uncertainties for the non-prompt fraction results in each of the three rapidity slices are shown in Figure 6.2. As several of the uncertainties approximately cancel in the fraction, the fractional uncertainties are smaller, compared to the cross-section uncertainties.

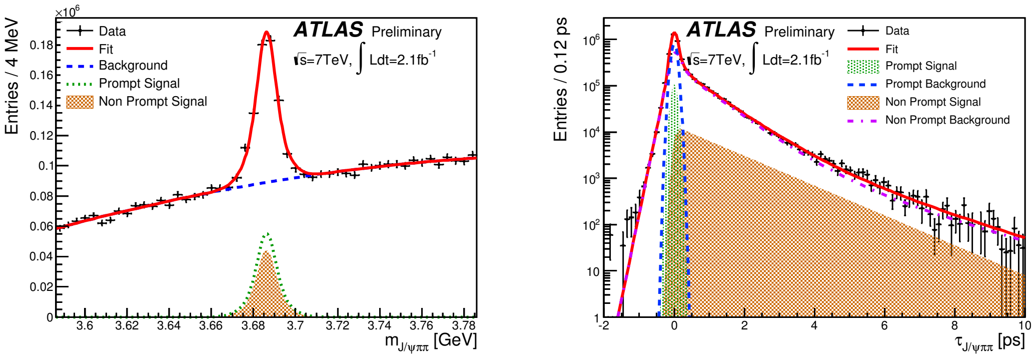

(a) $|y| < 0.75$, $11 < p_T < 12$ GeV

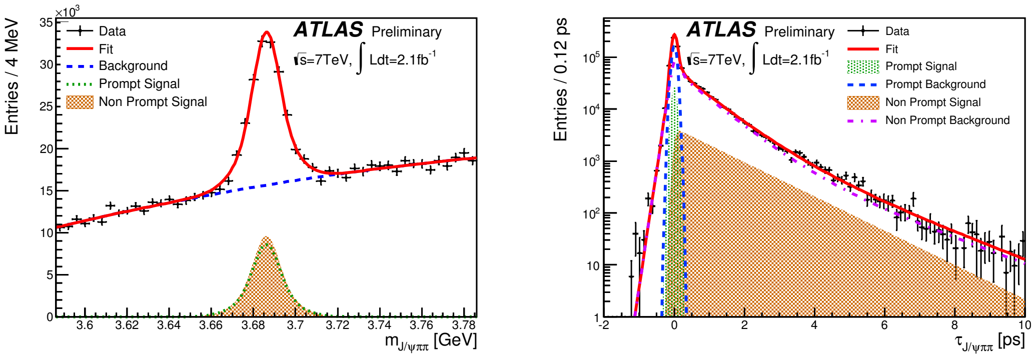

(b) $0.75 < |y| < 1.5$, $16 < p_T < 18$ GeV

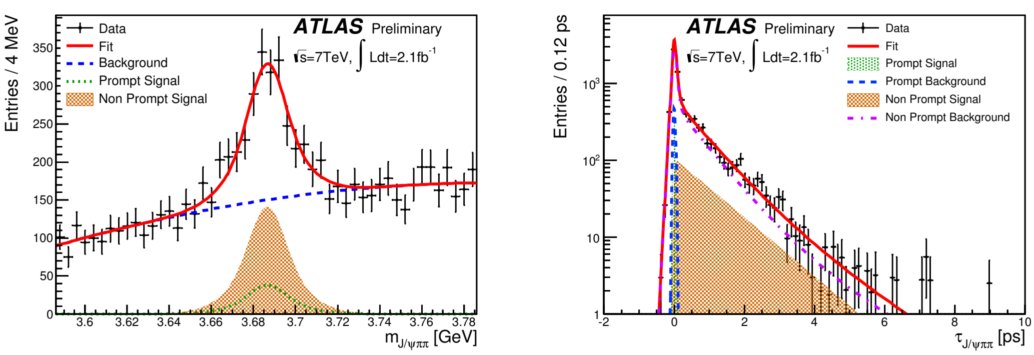

(c) $1.5 < |y| < 2.0$, $40 < p_T < 60$ GeV

Figure 6.1: Three example showing the fits of the $\psi(2S)$ and the pseudo-proper lifetime

A summary of the individual and total systematic uncertainties, the statistical uncertainties, and the total overall uncertainties are shown in Figs. 6.3 and 6.4 for the prompt and non-prompt cross-sections, respectively. Positive and negative one-sigma uncertainties are presented, accounting for the asymmetry of the fit model variations.

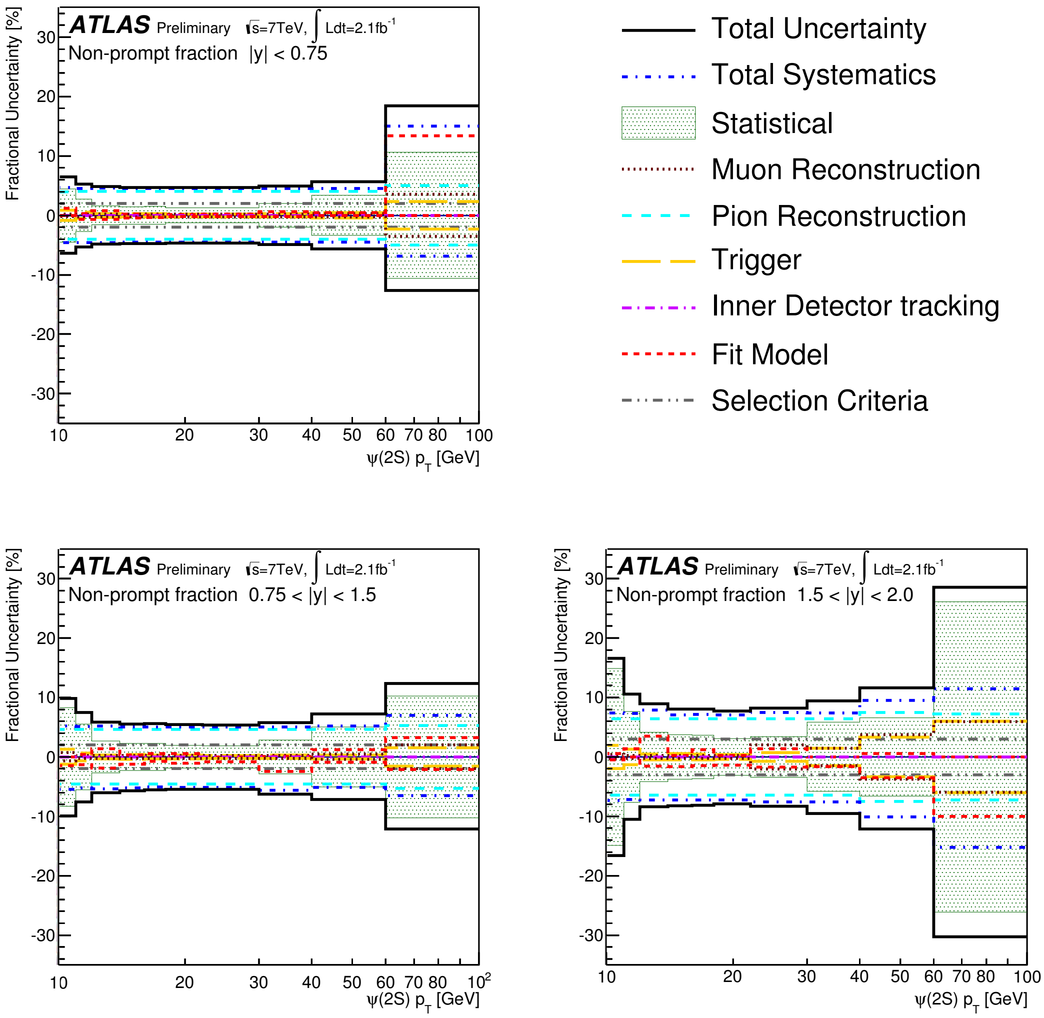

Figure 6.2: Summary of the positive and negative one-sigma uncertainties for the non-prompt fraction measurement.

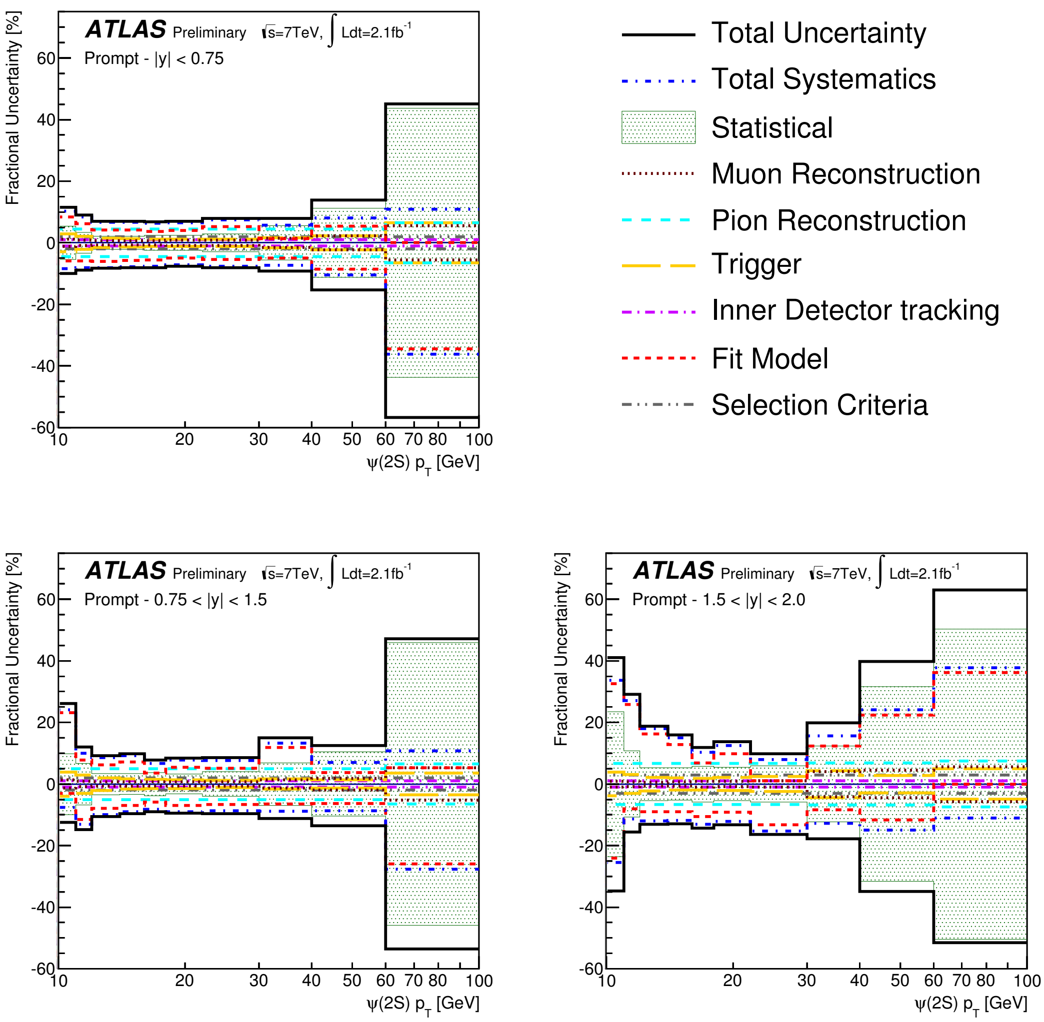

Figure 6.3: Summary of the positive and negative one-sigma uncertainties for prompt cross-section measurement. This plot does not include the 1.8% luminosity uncertainty.

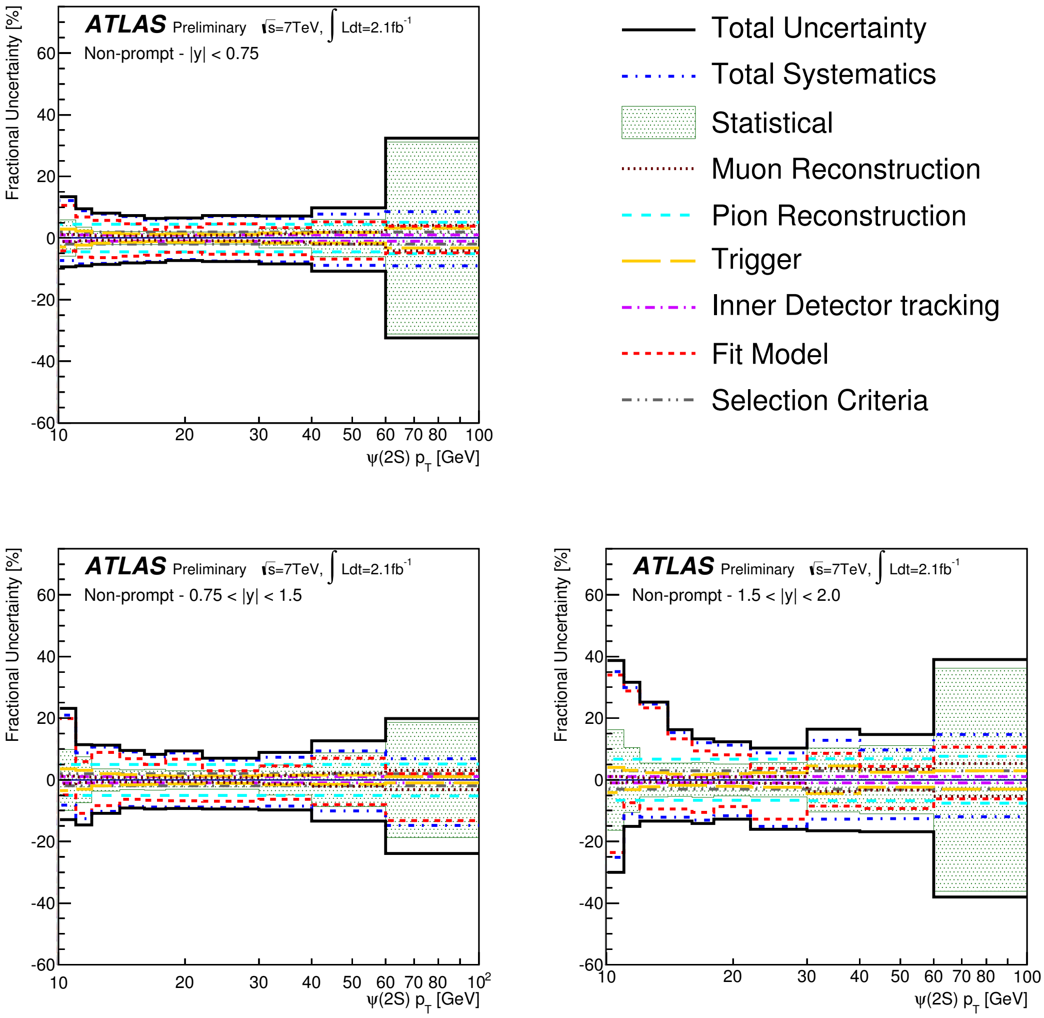

Figure 6.4: Summary of the positive and negative one-sigma uncertainties for the non-prompt cross-section measurement. This plot does not include the 1.8% luminosity uncertainty.

6.2 Non-Prompt fraction

Extracted from the fits is the non-prompt fraction, which shows that the fraction increases steadily with p_T in all three rapidity regions, Figure 6.5. Superimposed on the figure are the recent results from CMS [31], which extend coverage to lower-p_T. Good agreement is seen in the overlapping regions for all rapidity regions.

6.3 Cross Section Measurement

The corrected non-prompt $\psi(2S)$ production fraction, and the prompt and non-prompt $\psi(2S)$ production cross-sections have been measured in intervals of $\psi(2S)$ transverse momentum and three ranges of $\psi(2S)$ rapidity. All measurements presented assume the $\psi(2S)$ has isotropic acceptance.

Fully-corrected measurements of the differential prompt and non-prompt cross-sections are presented in Figures 6.6 and 6.7 and compared to earlier results from LHCb [70] and CMS [31] in similar or neighbouring rapidity intervals, which are also presented under the isotropic assumption. The ATLAS data points are placed at the mean of the weighted p_T distribution in each interval of p_T (indicated by the horizontal error bars).

6.4 Comparison with theoretical predictions

6.4.1 Prompt

Both LO and NLO NRQCD predictions are shown in comparison with the experimental data in Figure 6.8a. Uncertainties on the predictions come from the uncertainties on the choice of scale, charm quark mass and LDME as discussed in Ref. [71]. In the NLO results, NLO Colour Octet LDME from Ref. [72] are used. As Colour Octet LDME from NLO fits to data cannot reasonably be used for an LO calculation, the LO results are derived using the values in Table 1 of Reference [73], which are obtained by fitting the LO calculation to Tevatron

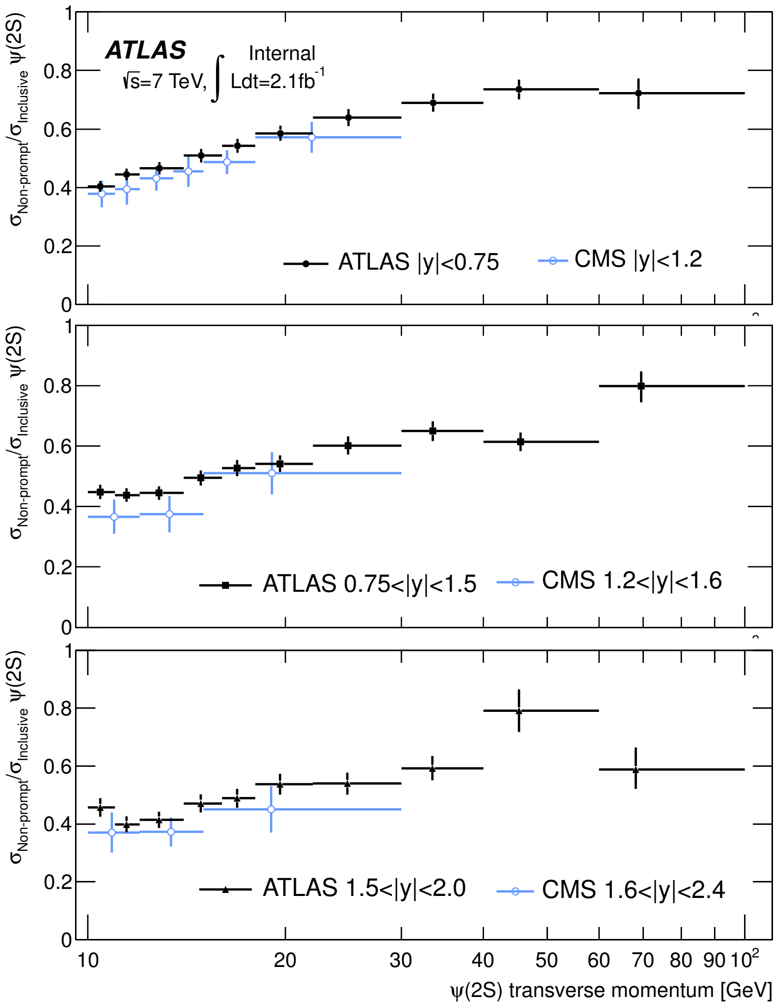

Figure 6.5: Non-prompt $\psi(2S)$ production fraction is calculated using Equation 5.4, and is shown here as a function of $\psi(2S)$ transverse momentum in three intervals of $\psi(2S)$ rapidity. The data points are at the mean of the weighted p_T distribution in each p_T interval, indicated by the horizontal error bars, and the vertical error bars represent the total statistical and systematic uncertainty (see Figure 6.2). Overlaid are previous results from the CMS experiment in similar rapidity intervals.

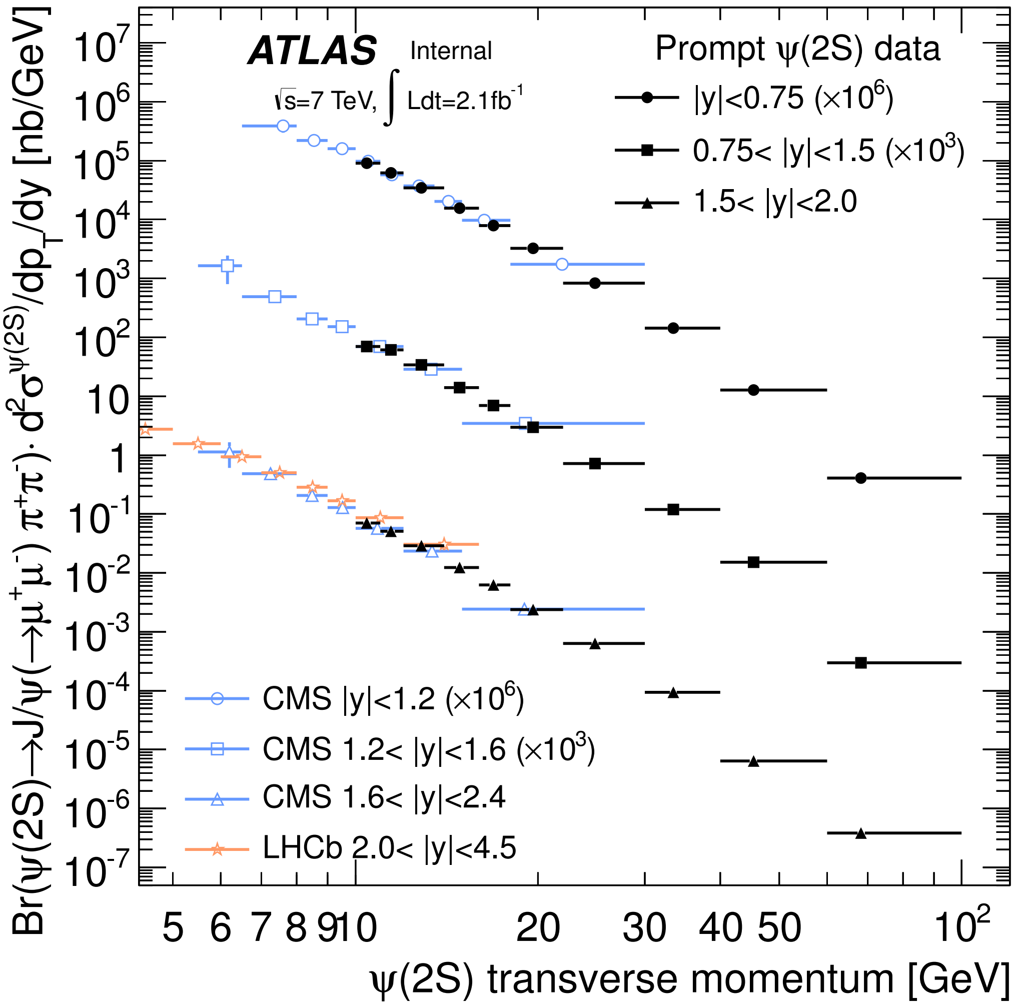

Figure 6.6: Measured differential cross-sections for prompt ψ(2S) production as a function of ψ(2S) transverse momentum for three ψ(2S) rapidity intervals. The results in the various rapidity intervals have been scaled by powers of ten for clarity of presentation. The data points are at the weighted mean of the p_T distribution in each p_T interval, indicated by the horizontal error bars, and the vertical error bars represent the total statistical and systematic uncertainty (see Figures 6.3 and 6.4). Overlaid are results from the CMS and LHCb experiments in the indicated rapidity intervals.

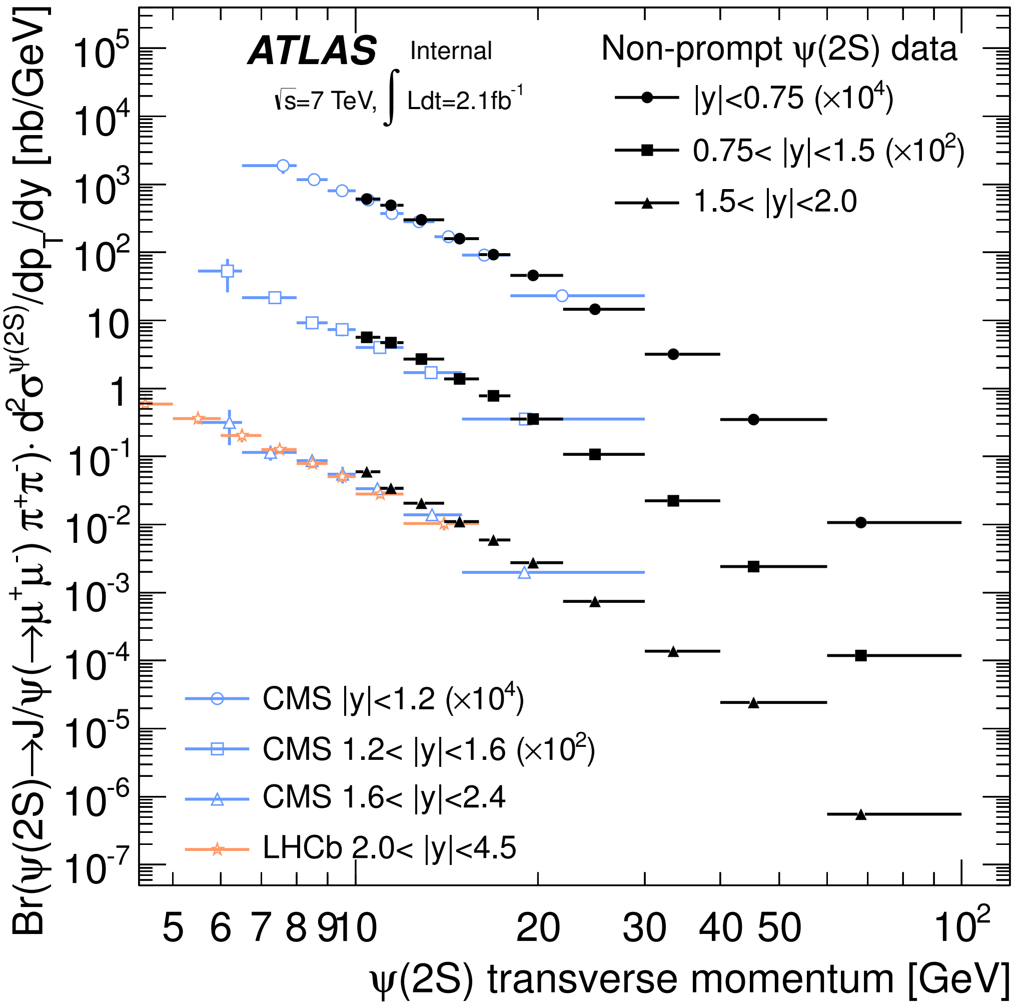

Figure 6.7: Measured differential cross-sections for non-prompt $\psi(2S)$ production as a function of $\psi(2S)$ transverse momentum for three $\psi(2S)$ rapidity intervals. The results in the various rapidity intervals have been scaled by powers of ten for clarity of presentation. The data points are at the weighted mean of the p_T distribution in each p_T interval, indicated by the horizontal error bars, and the vertical error bars represent the total statistical and systematic uncertainty (see Figures 6.3 and 6.4). Overlaid are results from the CMS and LHCb experiments in the indicated rapidity intervals.

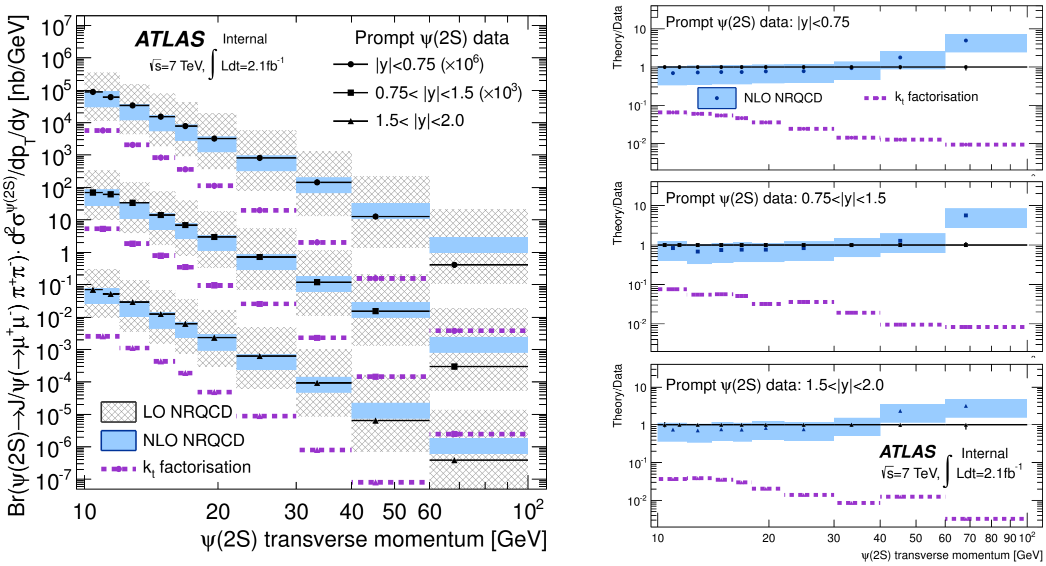

(a) Cross-sections

(b) Theory/Data ratio

Figure 6.8: Measured differential cross-sections (a) and ratios of the predicted to measured differential cross-sections (b) for prompt $\psi(2S)$ production as a function of $\psi(2S)$ transverse momentum for three $\psi(2S)$ rapidity intervals with comparison to theoretical predictions in the ATLAS fiducial region. The data points are at the weighted mean of the p_T distribution in each p_T interval, indicated by the horizontal error bars, and the vertical error bars represent the total statistical and systematic uncertainty (see Figure 6.3).

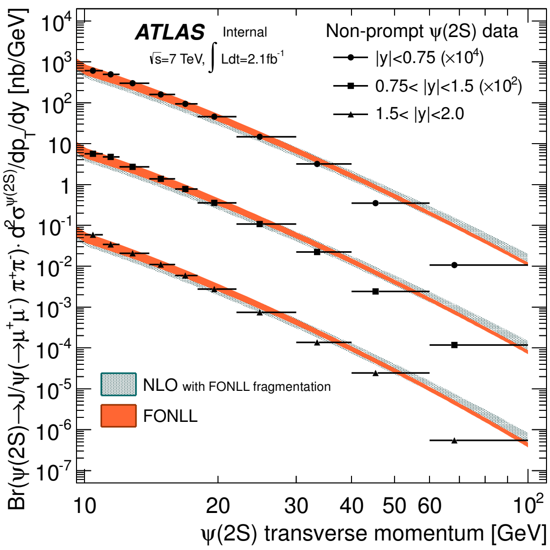

(a) Cross-sections

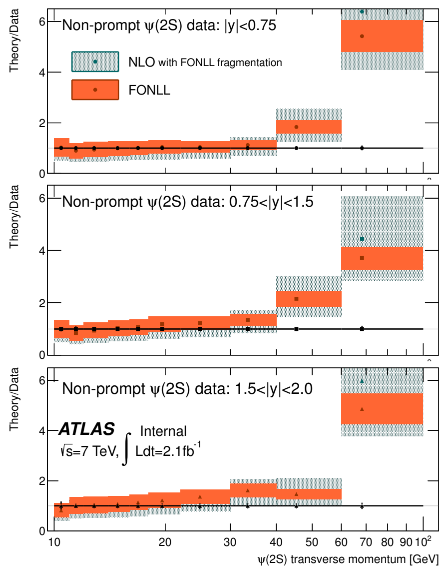

(b) Theory/Data ratio

Figure 6.9: Measured differential cross-sections (a) and ratios of the predicted to measured differential cross-sections (b) for non-prompt $\psi(2S)$ production as a function of $\psi(2S)$ transverse momentum for three $\psi(2S)$ rapidity intervals with comparison to theoretical predictions in the ATLAS fiducial region. The data points are at the weighted mean of the p_T distribution in each p_T interval, indicated by the horizontal error bars, and the vertical error bars represent the total statistical and systematic uncertainty (see Figure 6.4).

Run-1 data. LO predictions show agreement with the data, but have large uncertainties. NLO predictions do well at describing the shape and normalisation of prompt production data over a large range of transverse momenta. However, at the highest transverse momenta shown, NRQCD tends to predict a higher cross-section than observed. The ratio of theory to data is shown in Figure 6.8b where a deviation from the data at high p_T is clearly seen.

Parameter settings for the k_T-factorisation predictions shown here are described in [30], and make use of the CCFM A0 gluon parametrisation [74]. Comparison with data shows that the k_T factorisation approach significantly underestimates the prompt $\psi(2S)$ production rate. This underestimation may be related to the observation [75] that the same model overestimates the production of C-even (χ_c) charmonium states, a possible reason given for this may be that higher-order corrections are needed.

6.4.2 Non-prompt

For non-prompt production, comparison is made to theoretical predictions from FONLL calculations [32, 33] which have been successful in describing J/ψ [26] and B-meson production [76] at the LHC. Figure 6.9a shows a comparison of FONLL predictions to the non-prompt experimental data. A good agreement is observed, though FONLL slightly underestimates the data at low p_T and overestimates them at the highest p_T values studied, predicting an overall p_T distribution softer than observed. Figure 6.9b shows the theory to data ratio, in which the previously mentioned discrepancies are noticeable. The NLO non-prompt predictions shown in Figure 6.9a use the same non-perturbative fragmentation functions, PDF set and scale choices as the FONLL predictions.

In Figure 6.9b it can be seen that the resummed FONLL prediction shows better agreement than fixed-order NLO in the central value of the prediction, particularly at larger transverse momentum scales. In Ref. [33] it is mentioned that the differences between NLO and FONLL can be compensated by using a fragmentation function derived from an NLO fit to LEP data. Nonetheless, it is clear that both the FONLL and NLO approaches predict a p_T spectrum for non-prompt production, that is slightly underestimating the rate at low p_T and overestimating the rate at high p_T.

Chapter 7

Conclusions

The work presented in this thesis builds upon the first quarkonium results obtained from the early ATLAS data. During this period the amount of data was ever increasing, so the outline and limits of this analysis were continuously evolving. Once the final goal was decided, the work carried out on the early data proved to be a great testing ground, and helped to establish techniques that are currently used in many quarkonium studies.

The analysis was successful in producing a cross-section measurement of $\psi(2S) \rightarrow J/\psi(\rightarrow \mu^+\mu^-)\pi^+\pi^-$ with data from the ATLAS detector that covers the region $|y| < 2.0$, $10 < p_T < 100$ GeV. This measurement was made with the assumption that the spin-alignment is isotropic ($\lambda_\theta = \lambda_\phi = \lambda_{\theta\phi} = 0$). In case this assumption is proven to be incorrect, the spin-alignment envelope that was produced as part of the analysis will be useful in providing the necessary correction factor. The details of how the techniques and correction factors were used to obtain these results were presented in Chapter 5.

When compared to existing LHC results, the measurement was shown to have good agreement in the overlapping regions. It also expanded the range of current LHC results to a higher transverse momenta. When the prompt cross-section measurement was compared to k_T factorisation, it was shown that the results were about an order-of-magnitude above the predictions. LO NRQCD predicted that the cross-section should be larger than it is. The best prediction for the prompt production cross-section is the NLO NRQCD, which has a good agreement at lower p_T, but is larger than the results at high p_T.

The comparison of the non-prompt cross-section to the FONLLL prediction shows, that at low p_T the prediction matches the data, but at higher p_T the result drops below the expected prediction region. The fixed-order NLO prediction has a similar shaped distribution as the FONLL, but has larger uncertainties. All the comparisons to data and theoretical models were presented in Chapter 6.

The outlook for the future is good, as there is a number of quarkonium analyses ongoing that will become available in due course. Part of 2011 data, as well as the full set of 2012 data are still to be analysed for $J/\psi\pi\pi$ events. After the long shut-down there are many quarkonium studies planned, which will look for rarer processes, such as exotic states and double quarkonium production, and possibly even new states. So hopefully in the not too distant future this work will be built upon, just as this work built upon earlier studies.

Appendix A

Software and Data

A.1 Software

This section contains information about the software setup and finer details of the data. The analysis was perform using the ATLAS analysis software (Athena) release 17.0.6.3, with the following Good Run List (GRL), which requires the all luminosity blocks (a predefined amount of time of the run) used to have the data quality status flag set to good.

Muon good run list:

`data11_7TeV.periodAllYear_DetStatus-v36-pro10-02_CoolRunQuery-00-04-08_All_Good.xml`

A.2 Data

The analysis was carried out on LHC data periods B2-K4, which have luminosity and run range as shown in Table. A.1. The data used came from the physics_Muons stream and uses the DAOD_ONIAMUMU (data containers in which the di-muon events are already constructed) containers:

- data11_7TeV.periodB2.physics_Muons.PhysCont.DAOD_ONIAMUMU.pro10_01
- data11_7TeV.periodD.physics_Muons.PhysCont.DAOD_ONIAMUMU.pro10_01

- data11_7TeV.periodE.physics_Muons.PhysCont.DAOD_ONIAMUMU.pro10_01
- data11_7TeV.periodF2.physics_Muons.PhysCont.DAOD_ONIAMUMU.pro10_01
- data11_7TeV.periodF3.physics_Muons.PhysCont.DAOD_ONIAMUMU.pro10_01
- data11_7TeV.periodG.physics_Muons.PhysCont.DAOD_ONIAMUMU.pro10_01
- data11_7TeV.periodH.physics_Muons.PhysCont.DAOD_ONIAMUMU.pro10_01
- data11_7TeV.periodI.physics_Muons.PhysCont.DAOD_ONIAMUMU.pro10_01
- data11_7TeV.periodJ.physics_Muons.PhysCont.DAOD_ONIAMUMU.pro10_01
- data11_7TeV.periodK1.physics_Muons.PhysCont.DAOD_ONIAMUMU.pro10_01
- data11_7TeV.periodK2.physics_Muons.PhysCont.DAOD_ONIAMUMU.pro10_01
- data11_7TeV.periodK3.physics_Muons.PhysCont.DAOD_ONIAMUMU.pro10_01
- data11_7TeV.periodK4.physics_Muons.PhysCont.DAOD_ONIAMUMU.pro10_01

Table A.1: Total luminosity split into LHC data periods

Period	Run Range	Luminosity
B2	178044-178109	11.5745 pb^{-1}
D	179710-180481	156.453 pb^{-1}
E	180614-180776	47.0929 pb^{-1}
F2	182161-182486	115.647 pb^{-1}
F3	182516-182519	13.4135 pb^{-1}
G	182726-183462	495.019 pb^{-1}
H	183544-184169	252.911 pb^{-1}
I	185353-186493	316.22 pb^{-1}
J	186516-186755	220.384 pb^{-1}
K1	186873-186934	184.384 pb^{-1}
K2	186965-187219	196.394 pb^{-1}
K3	187453-187552	73.9473 pb^{-1}
K4	187763-187763	37.7513 pb^{-1}
Total	178044-187763	2121.1915 pb^{-1}
Total Corrected		2091.6986 pb^{-1}

Appendix B

Cut flow Evolution

The selection criteria not only reduce the background events, but they can also reduce the signal events, and these events need to be account for. This section investigates the amount of the signal events not passing the selection criteria.

B.1 Prob(χ^2) Selection Criteria

The Prob(χ^2) cut was used to significantly reduce the background, but it also slightly reduced the signal peak. The signal peak obtained from data was fitted before and after the cut in three p_T slices over the integrated rapidity, which is shown in Fig. B.1. The signal peaks are both fitted with the same double Gaussian, where the second sigma is fixed to 2.5 times the first sigma. The efficiency of the cut was calculated using the fit and is shown in Table. B.1.

Table B.1: Efficiency of the Prob(χ^2) quality selection cut applied to the $J/\psi\pi\pi$ vertex fit. The uncertainty shown is statistical only.

p_T	Signal Efficiency
10-16	$(93.2 \pm 0.2\%)$
16-30	$(95.0 \pm 0.2\%)$
30-100	$(96.8 \pm 0.3\%)$

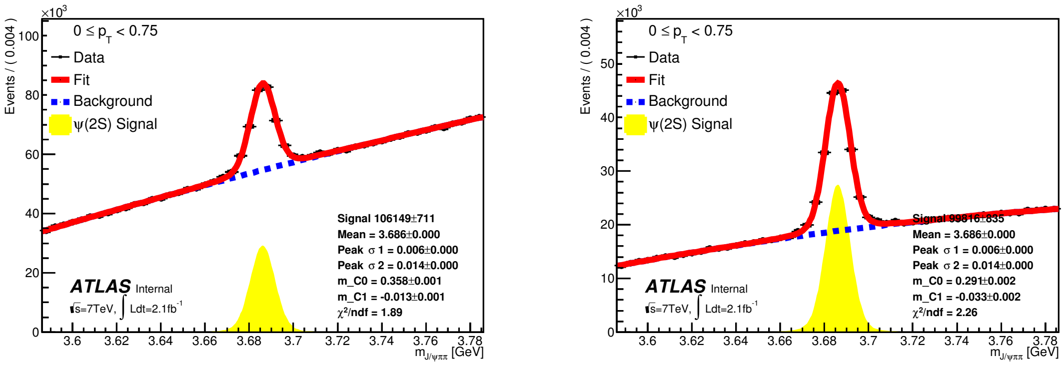

(a) $0 \leq |y| < 0.75$

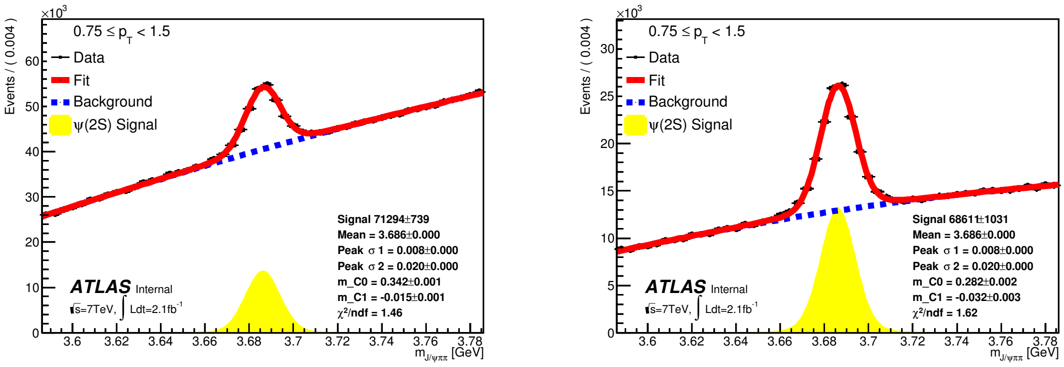

(b) $0.75 \leq |y| < 1.5$

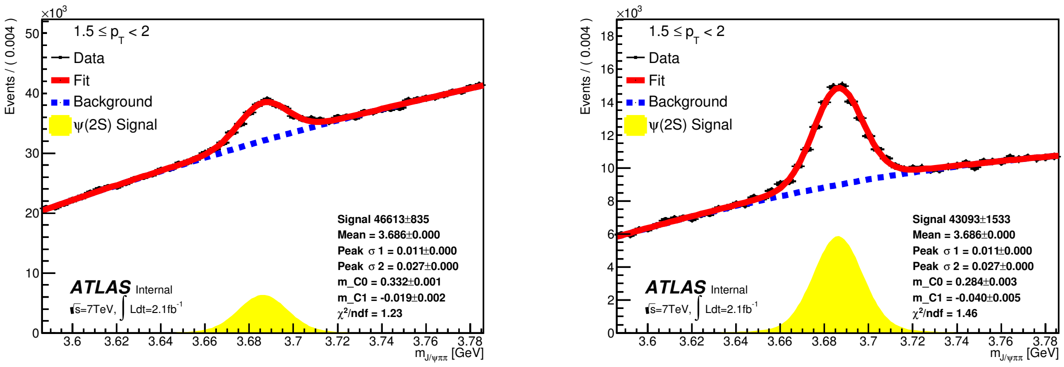

(c) $1.5 \leq |y| < 2.0$

Figure B.1: Fits of the mass distribution before(left) and after(right) applying the prob(χ^2) selection cut.

B.2 Cut flow Evolution

To estimate the effect of the selection criteria, presented in Table 5.3, which are not already covered in the muon, pion and trigger efficiency corrections. This investigated was carried out using the cut-flow procedure shown in Tables B.2-B.4, in which the numbers of events that pass or fail a given selection criteria are compared, based on a sample of Monte-Carlo ψ(2S) signal.

Table B.2: Cut flow table using Monte-Carlo to estimate the inefficiencies of specific selection requirements on the data. Yields are given for the three rapidity slices as each cut is applied (**Full cut flow**).

Selection	$\|y\| < 0.75$	$0.75 < \|y\| < 1.5$	$1.5 < \|y\| < 2.0$
All ψ(2S) Candidates (3.586 - 3.786 GeV)	4598	3930	2964
Passing Acc muons $p_T > 4$ GeV, $\|\eta\| < 2.3$	4354	3748	2773
Passing Acc pions $p_T > 0.5$ GeV, $\|\eta\| < 2.5$	4354	3748	2773
Passing Muon oppsitely charged	4354	3748	2773
Passing Pion oppsitely charged	4354	3748	2773
Passing Muon combined	4192	3526	2713
Passing Di-Muon $p_T > 8$ GeV	4161	3515	2677
Passing Di-Muon $\|y\| < 2.0$	4161	3515	2631
Passing Di-Muon $\chi^2 < 200$	4161	3515	2631
Passing $J/\psi\pi\pi$ Prob(χ^2) > 0.005	2491	2034	1338

B.2.1 ID tracking efficiency determination

The efficiency of the ID tracking of the two muons is conservatively estimated to be $(99 \pm 1)\%$, as used in Ref. [64]. The main reference would be the 2010 minbias paper, where the p_T–η dependence of their maps was very variable, but the figure $(99 \pm 1)\%$ fully bound all of these variations, leading to a conservative estimate on the uncertainty. Given that even this overestimated figure is one of the smallest individual systematics, applying the p_T–η map is not required. Additional information is available from [77].

Table B.3: Cut flow table using Monte-Carlo to estimate the inefficiencies of specific selection requirements on the data. Yields are given for the three rapidity slices as each cut is applied (**Without Di-Muon** p_T **> 8 GeV**).

Selection	$\|y\| < 0.75$	$0.75 < \|y\| < 1.5$	$1.5 < \|y\| < 2.0$
All $\psi(2S)$ Candidates (3.586 - 3.786 GeV)	4598	3930	2964
Passing Acc muons $p_T > 4$ GeV, $\|\eta\| < 2.3$	4354	3748	2773
Passing Acc pions $p_T > 0.5$ GeV, $\|\eta\| < 2.5$	4354	3748	2773
Passing Muon oppsitely charged	4354	3748	2773
Passing Pion oppsitely charged	4354	3748	2773
Passing Muon combined	4192	3526	2713
Passing Di-Muon $\|y\| < 2.0$	4192	3526	2667
Passing Di-Muon $\chi^2 < 200$	4192	3526	2667
Passing $J/\psi\pi\pi$ Prob(χ^2) > 0.005	2501	2041	1353
Difference to full cut flow	10	7	15

Table B.4: Cut flow table using Monte-Carlo to estimate the inefficiencies of specific selection requirements on the data. Yields are given for the three rapidity slices as each cut is applied (**Without Di-Muon** $|y| < 2.0$).

Selection	$\|y\| < 0.75$	$0.75 < \|y\| < 1.5$	$1.5 < \|y\| < 2.0$
All $\psi(2S)$ Candidates (3.586 - 3.786 GeV)	4598	3930	2964
Passing Acc muons $p_T > 4$ GeV, $\|\eta\| < 2.3$	4354	3748	2773
Passing Acc pions $p_T > 0.5$ GeV, $\|\eta\| < 2.5$	4354	3748	2773
Passing Muon oppsitely charged	4354	3748	2773
Passing Pion oppsitely charged	4354	3748	2773
Passing Muon combined	4192	3526	2713
Passing Di-Muon $p_T > 8$ GeV	4161	3515	2677
Passing Di-Muon $\chi^2 < 200$	4161	3515	2677
Passing $J/\psi\pi\pi$ Prob(χ^2) > 0.005	2491	2034	1356
Difference to full cut flow	0	0	18

Table B.5: Selection criteria efficiencies

	$\lvert y\rvert < 0.75$	$0.75 < \lvert y\rvert < 1.5$	$1.5 < \lvert y\rvert < 2.0$
p_T 10-16 GeV	92.8%	92.9%	90.8%
p_T 16-30 GeV	94.6%	94.7%	92.6%
p_T 30-100 GeV	96.4%	96.5%	94.4%
mean	94.6 ± 2.0 %	94.7 ± 2.0 %	92.6 ± 2.0 %

B.2.2 Di-muon χ^2 selection

It is shown in Reference [78], section K that the di-muon vertex $\chi^2 < 200$ requirement is known to have a negligible impact on the signal efficiency.

Appendix C

Acceptance

C.1 Acceptance

In this section the six anisotropic spin-alignment cases are considered. The acceptance maps for six cases are presented in Figures(C.1- C.6), which each show the lowest, highest di-pion masses and the ratio between the two. Table C.1 shows the numerical values of the ratios between the anisotropic cases and the isotropic, which was shown as a set of histograms in Figure 5.4.

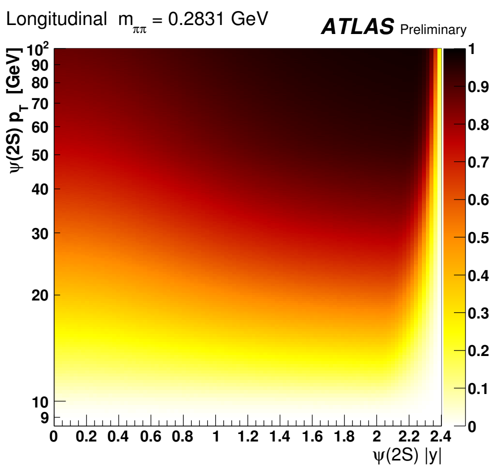

(a) Lowest di-pion bin - Longitudinal

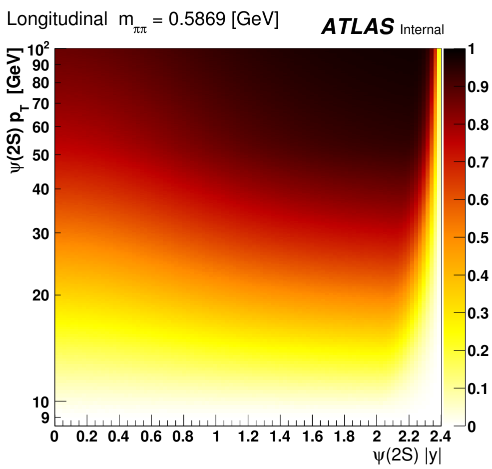

(b) Highest di-pion bin - Longitudinal

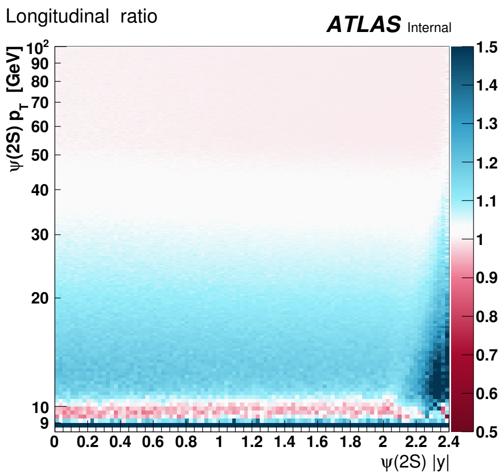

(c) Ratio - Longitudinal

Figure C.1: Examples of the longitudinal acceptance map

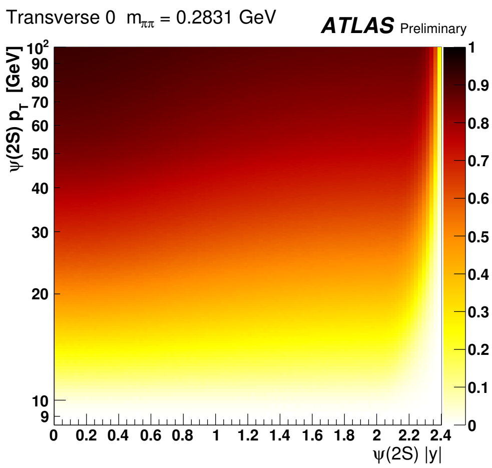

(a) Lowest di-pion bin - Transverse zero

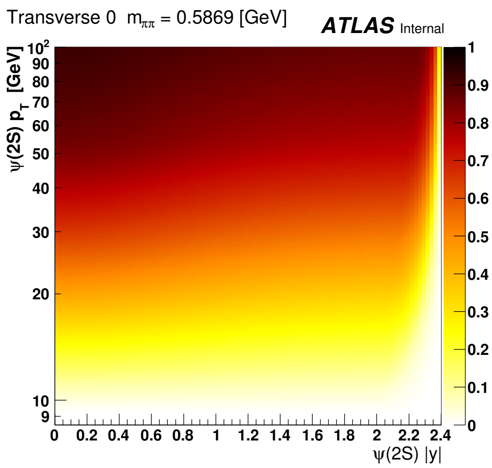

(b) Highest di-pion bin - Transverse zero

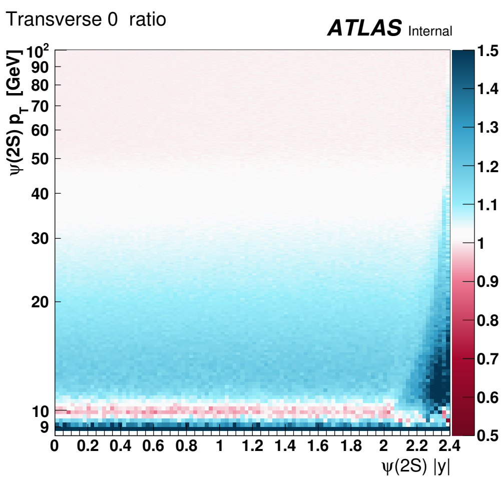

(c) Ratio - Transverse zero

Figure C.2: Examples of the transverse zero acceptance map

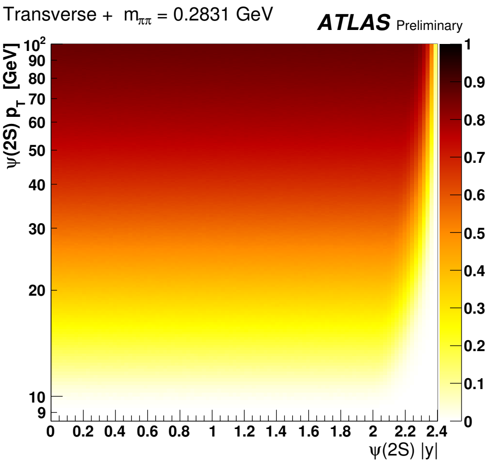

(a) Lowest di-pion bin - Transverse positive

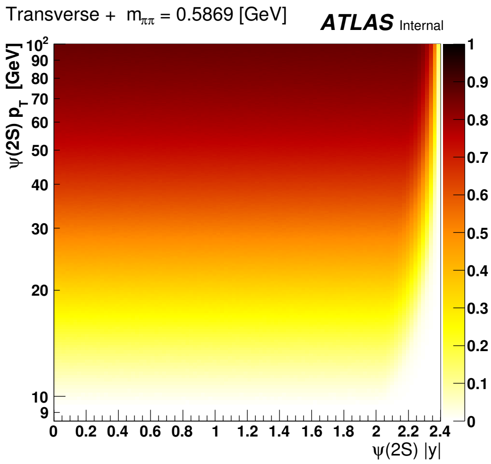

(b) Highest di-pion bin - Transverse positive

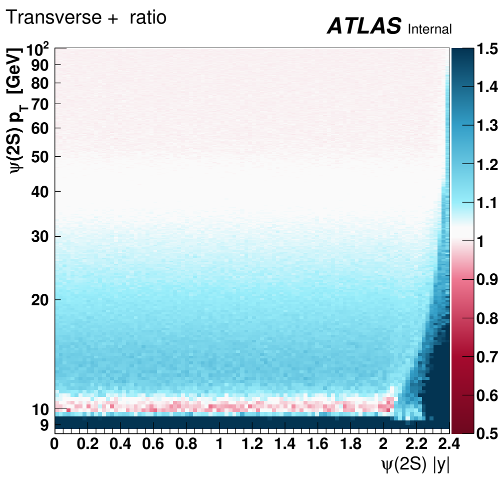

(c) Ratio - Transverse positive

Figure C.3: Examples of the transverse positive acceptance map

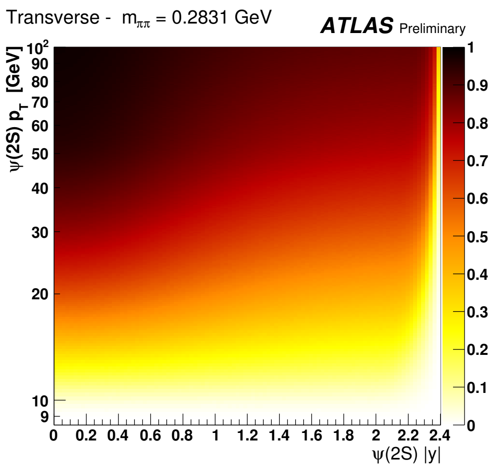

(a) Lowest di-pion bin - Transverse negative

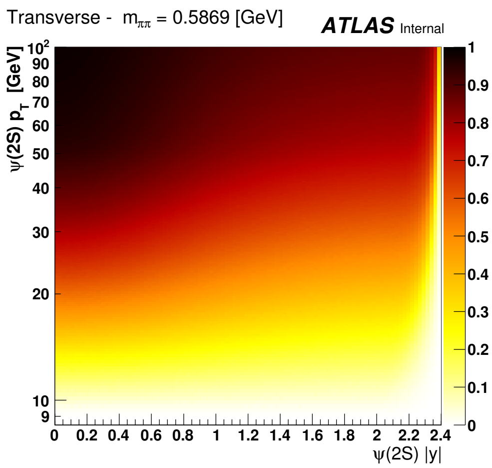

(b) Highest di-pion bin - Transverse negative

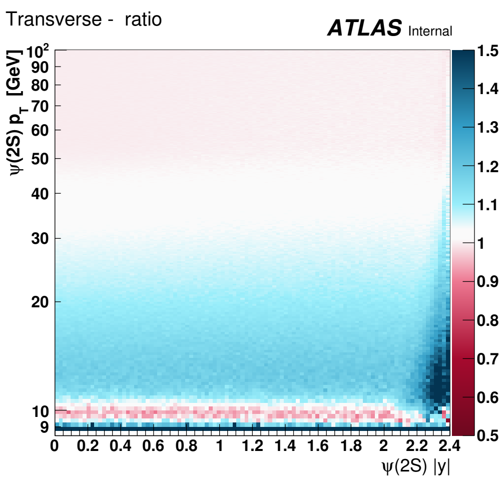

(c) Ratio - Transverse negative

Figure C.4: Examples of the transverse negative acceptance map

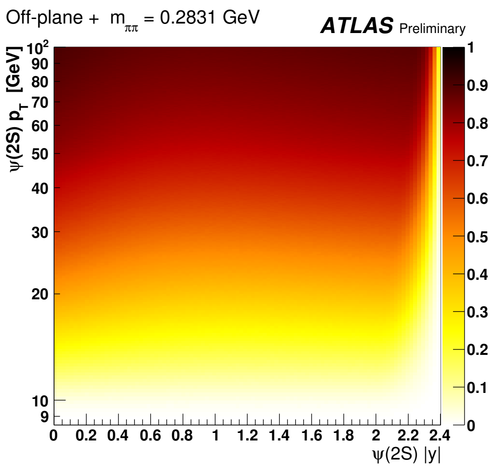

(a) Lowest di-pion bin - off-plane positive

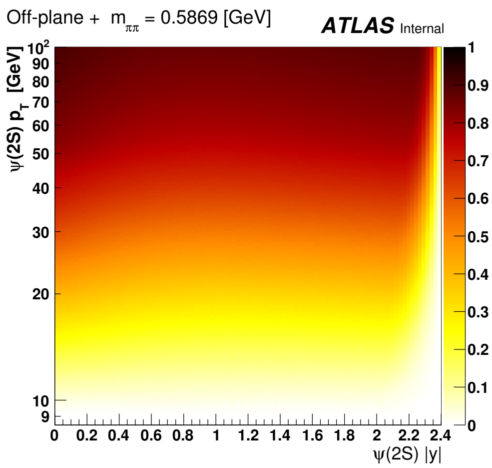

(b) Highest di-pion bin - off-plane positive

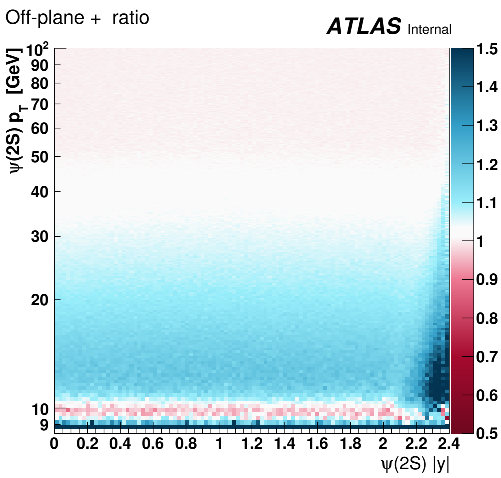

(c) Ratio - off-plane positive

Figure C.5: Examples of the off-plane positive acceptance map

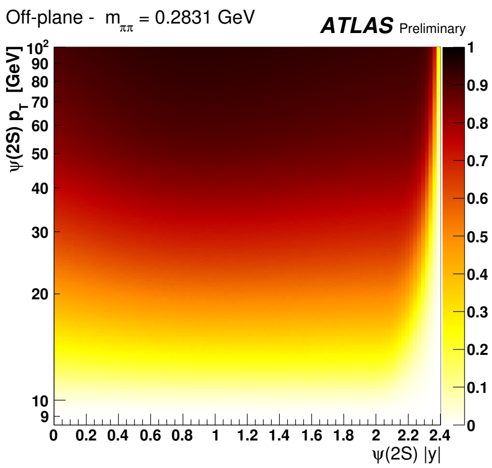

(a) Lowest di-pion bin - Off-plane negative

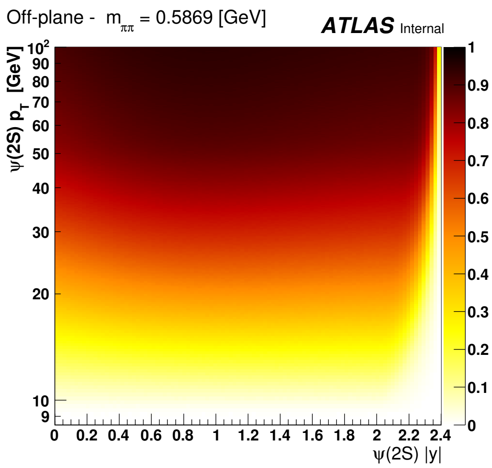

(b) Highest di-pion bin - Off-plane negative

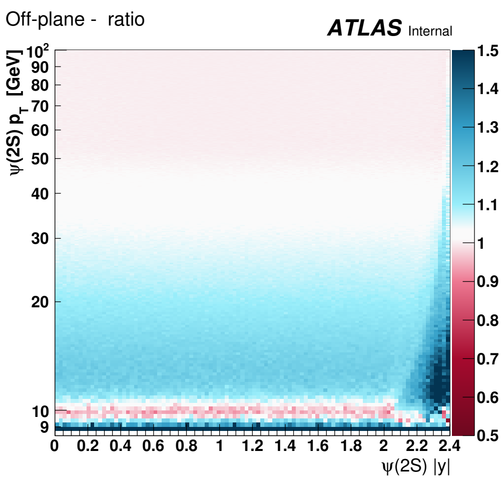

(c) Ratio - off-plane negative

Figure C.6: Examples of the off-plane negative acceptance map

Table C.1: Correction factors to correct measured prompt production cross-sections from isotropic production to an alternative spin-alignment scenario.

p_T	10-11	11-12	12-14	14-16	16-18	18-22	22-30	30-40	40-60	60-100	GeV
Longitudinal											
$\lvert y\rvert <0.75$	1.07	1.13	1.16	1.15	1.14	1.13	1.10	1.08	1.06	1.04	
$0.75< \lvert y\rvert <1.5$	0.89	0.92	0.92	0.92	0.92	0.92	0.92	0.93	0.94	0.95	
$1.5< \lvert y\rvert <2$	0.79	0.80	0.80	0.80	0.81	0.81	0.83	0.86	0.88	0.91	
Transverse zero											
$\lvert y\rvert <0.75$	0.97	0.95	0.94	0.94	0.94	0.95	0.96	0.97	0.98	0.98	
$0.75< \lvert y\rvert <1.5$	1.07	1.05	1.05	1.05	1.05	1.05	1.05	1.04	1.03	1.03	
$1.5< \lvert y\rvert <2$	1.16	1.15	1.14	1.14	1.14	1.13	1.11	1.09	1.07	1.05	
Transverse positive											
$\lvert y\rvert <0.75$	1.62	1.43	1.36	1.30	1.27	1.23	1.19	1.14	1.10	1.07	
$0.75< \lvert y\rvert <1.5$	1.60	1.43	1.36	1.30	1.27	1.23	1.19	1.14	1.10	1.07	
$1.5< \lvert y\rvert <2$	1.60	1.43	1.36	1.30	1.27	1.23	1.19	1.14	1.10	1.07	
Transverse negative											
$\lvert y\rvert <0.75$	0.70	0.71	0.72	0.74	0.75	0.77	0.80	0.84	0.88	0.91	
$0.75< \lvert y\rvert <1.5$	0.80	0.83	0.86	0.88	0.70	0.91	0.94	0.96	0.97	0.99	
$1.5< \lvert y\rvert <2$	0.91	0.96	0.99	1.02	1.03	1.04	1.05	1.05	1.04	1.03	
Off-plane positive											
$\lvert y\rvert <0.75$	1.11	1.13	1.13	1.13	1.13	1.12	1.10	1.08	1.06	1.04	
$0.75< \lvert y\rvert <1.5$	1.24	1.26	1.27	1.25	1.24	1.21	1.17	1.13	1.10	1.06	
$1.5< \lvert y\rvert <2$	1.24	1.26	1.25	1.23	1.21	1.18	1.14	1.10	1.08	1.06	
Off-plane negative											
$\lvert y\rvert <0.75$	0.92	0.90	0.90	0.90	0.90	0.91	0.92	0.93	0.95	0.96	
$0.75< \lvert y\rvert <1.5$	0.84	0.83	0.82	0.83	0.84	0.85	0.87	0.90	0.92	0.95	
$1.5< \lvert y\rvert <2$	0.84	0.83	0.83	0.84	0.85	0.87	0.89	0.91	0.93	0.95	

Appendix D

Pion Studies

D.1 Pion Reconstruction

In this section the details are given of the steps and checks used in the creation of the pion reconstruction efficiency map. The pion reconstruction efficiency map was created using an 80% sample of the MC, and the remaining 20% of the MC was used to perform a closure test, which is when the pion reconstruction efficiency map is used to correct the reconstruction data and then compared to the truth. The closure distribution is shown in Figure D.1. The MC used was:
`mc11_7TeV.108529.Pythia_Psi2S_Jsipipi_mu0mu0.merge.AOD.e1039_a131_s1353_a146_r2993`

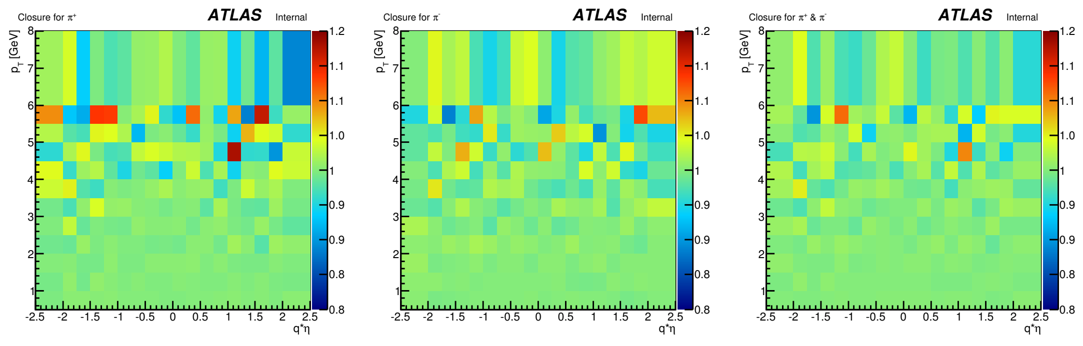

Figure D.1: Closure test of the pion reconstruction map, for π^+, π^- and both $\pi^+ \& \pi^-$

D.2 Primary Vertex Z0 Distribution

There was concern that the difference between the data and MC distribution of the Primary Vertex (PV) in the z direction from the center of the detector (z0), could cause a meaningful shift in the pion reconstruction efficiency. This was investigated, and the results are shown in Figure D.2. In the end it was found that the shift was less than 0.25%, as can be seen in Figure D.3.

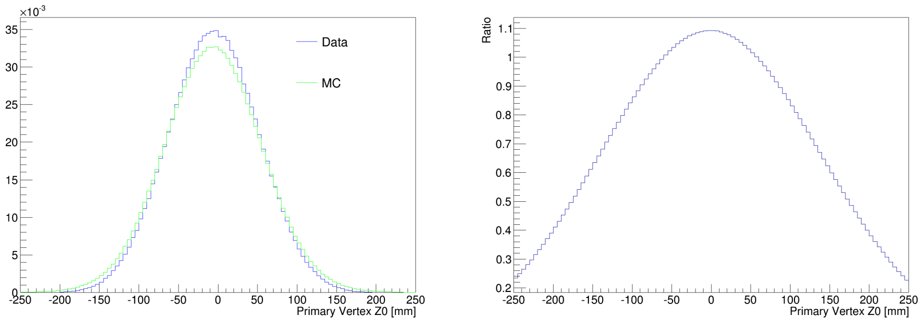

(a) The distribution of the PV z0 for MC and Data, which have been normalised to each other

(b) The ratio of of the PV z0 for MC and Data

Figure D.2: The distribution of the PV z0 for data and MC and the ratio between them.

D.3 Di-Pion Distribution

The di-pion distribution for the signal is obtained by spliting the di-pion events from data into a mass signal region ($3.646 < m_{\psi(2S)} < 3.726$) and upper ($3.736 < m_{\psi(2S)} < 3.776$) and lower ($3.596 < m_{\psi(2S)} < 3.636$) sidebands. The di-pion distribution of the sidebands and signal region were rescaled to range between $2 \cdot m_\pi (0.279$ GeV$)$ - $\Delta m_{(\psi(2S)-J/\psi)}$ (0.589 GeV). This has to be done, due to the shifting maximum of the allowed $m_{\pi\pi}$ (Figure D.4a). After the distributions were corrected (Figure D.4b), it was assumed that the di-pion background distribution under the signal peak and the sidebands is the same. Finally it was possible to use the sideband subtraction method to produce a di-pion distribution for the

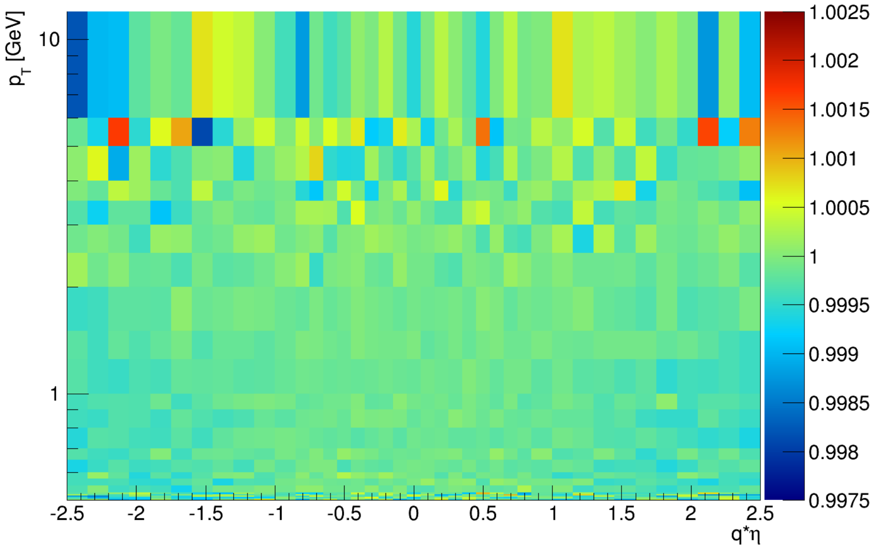

Figure D.3: Bin by bin difference between the original map and the re-weighted map.

signal events, seen in Figure D.5. The di-pion distribution has been fitted with the Voloshin-Zakharov model in results from other experiments, and the model is decribed by:

$$\frac{d\sigma}{dm_{\pi\pi}} \propto (PS) \times \left[m_{\pi\pi}^2 - \lambda m_\pi^2\right]^2 \tag{D.1}$$

where PS is the phase space factor (see Ref. [37]) and λ is the phenomenological parameter.

The result of LHCb [70] is $\lambda = 4.46 \pm 0.25$ and the result of BES [37] is $\lambda = 4.36 \pm 0.23$.

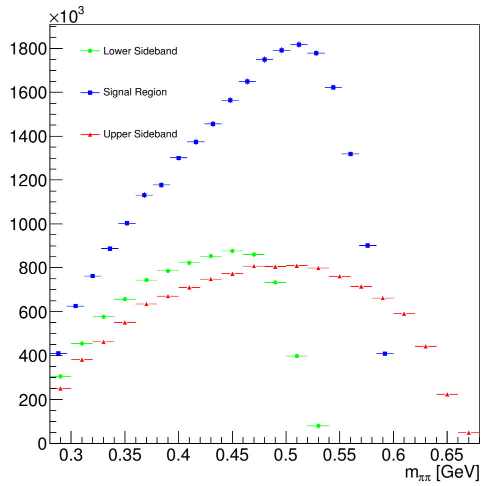

(a) Observed sidband and signal region di-pion distributions

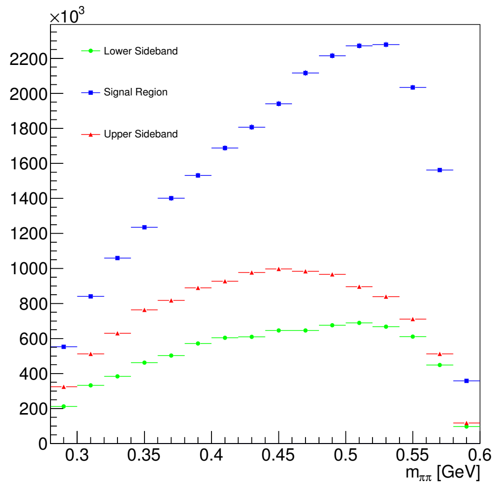

(b) Corrected sidband and signal region di-pion distributions

Figure D.4: Di-pion mass distributions for signal and sideband regions

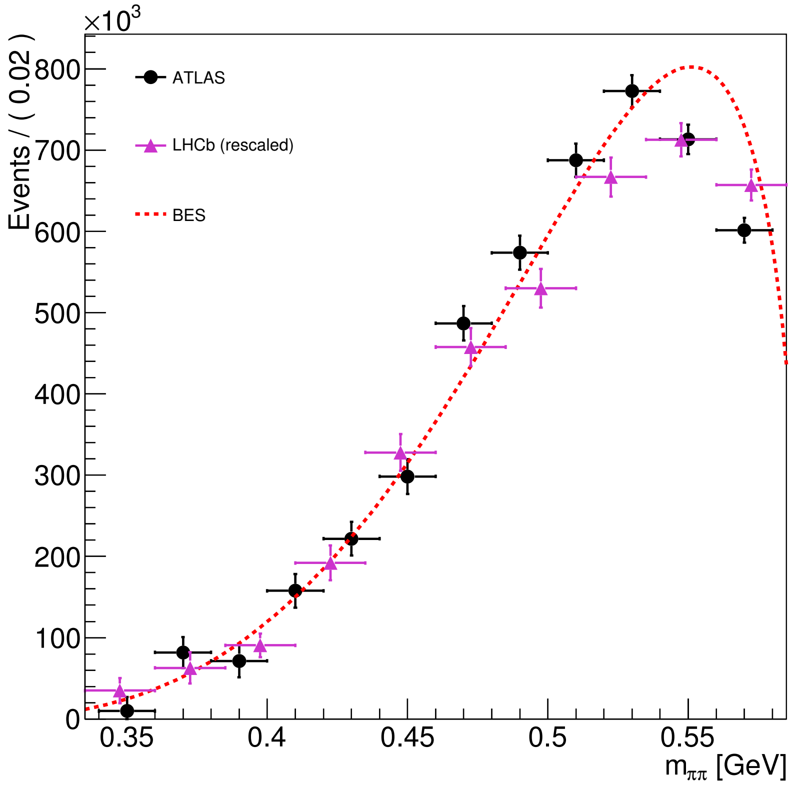

Figure D.5: Final di-pion mass distributions, compared to existing results.

Appendix E

Fit Results

This section covers the setup, checks and results of the fitting studies. The fitting code has to be stable and reliable, producing a model that matches the shapes of the data and provides a good goodness-of-fit (χ^2/ndf).

E.1 Fit Setup

The fits were performed using multiple CPUs, and a set of test fits were performed using only a single CPU. It was found that there was no discrepancy between the two results; this was checked because earlier versions of ROOT had a bug that produced a slight discrepancy. The ROOT setup used was:
ROOT Version: `5.34/07`
RooFit Version: `3.56`

E.2 Fit Sigma

It was found that the Gaussian width (σ) varied wildly in the lowest and highest p_T bins. To stabilise the fits, a first order polynomial was used to fit σ distribution for the three $|y|$ regions. In Chapters 5 and 6 when this function is used for the

Gaussian's width, it is denoted by (Fit σ). The result of the fits are shown in Figure E.1.

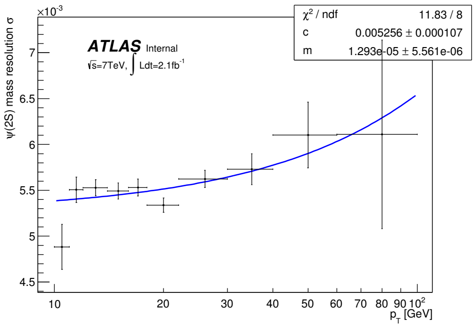

(a) $0 \leq |y| < 0.75$

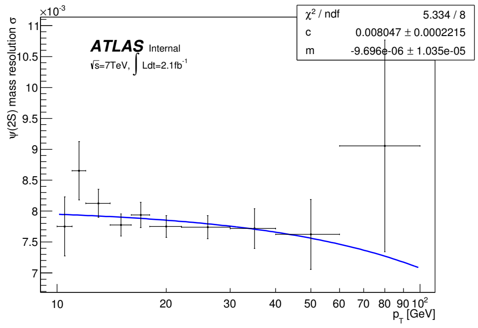

(b) $0.75 \leq |y| < 1.5$

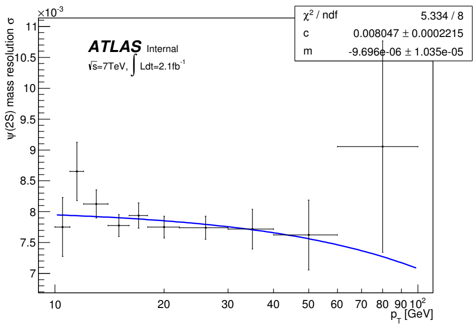

(c) $1.5 \leq |y| < 2.0$

Figure E.1: The $\psi(2S)$ mass resolution σ from central fit model without terms fixed.

E.3 Central Fit Result

The plots in Figures E.2, E.3 & E.4 are the central fit model results for all $p_T - |y|$ bins. The χ^2/ndf of all fit models are given in Table E.1, where the fit models match the one defined in Table 6.1.

Table E.1: Table of χ^2/ndf for fits.

$\|y\|$	10-11	11-12	12-14	14-16	16-18	18-22	22-30	30-40	40-60	60-100
Fit Model 0										
0.0-0.75	1.767	1.325	1.396	1.34	1.281	1.198	1.185	0.9657	1.123	1.426
0.75-1.5	3.185	1.837	1.733	1.477	1.423	1.232	1.125	1.075	0.9526	1.149
1.5-2.0	1.528	1.364	1.399	1.313	1.41	1.163	1.105	1.049	0.8476	1.652
Fit Model 1										
0.0-0.75	1.772	1.326	1.398	1.34	1.281	1.2	1.184	0.9648	1.123	1.386
0.75-1.5	3.178	1.825	1.733	1.476	1.423	1.231	1.125	1.074	0.9508	1.142
1.5-2.0	1.537	1.362	1.398	1.312	1.411	1.162	1.103	1.047	0.8451	1.503
Fit Model 2										
0.0-0.75	1.895	1.313	1.388	1.315	1.274	1.194	1.182	0.9482	1.121	1.365
0.75-1.5	3.155	1.84	1.72	1.471	1.431	1.229	1.1	1.067	0.9491	1.142
1.5-2.0	1.526	1.362	1.392	1.313	1.405	1.161	1.09	1.049	0.8425	1.662
Fit Model 3										
0.0-0.75	1.955	1.332	1.436	1.337	1.289	1.229	1.242	0.9593	1.121	1.315
0.75-1.5	3.163	1.84	1.747	1.488	1.44	1.231	1.113	1.098	0.948	1.083
1.5-2.0	1.535	1.394	1.434	1.321	1.402	1.17	1.097	1.043	0.8388	1.284
Fit Model 4										
0.0-0.75	1.889	1.321	1.394	1.336	1.275	1.196	1.178	0.9633	1.132	1.428
0.75-1.5	3.189	1.838	1.726	1.474	1.422	1.223	1.12	1.076	0.9514	1.148
1.5-2.0	1.526	1.363	1.397	1.313	1.41	1.166	1.104	1.046	0.8479	1.65
Fit Model 5										
0.0-0.75	1.892	1.472	1.643	1.649	1.589	1.574	1.652	1.368	1.263	1.367
0.75-1.5	3.149	1.99	1.904	1.686	1.656	1.541	1.448	1.377	1.003	1.127
1.5-2.0	1.523	1.36	1.462	1.416	1.551	1.287	1.259	1.155	0.8145	1.444

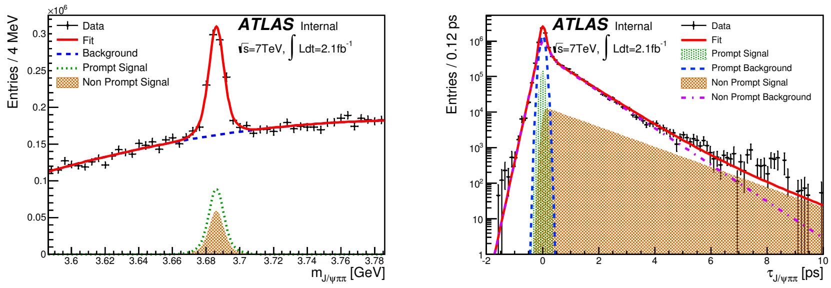

(a) $10 < |p_T| < 11$

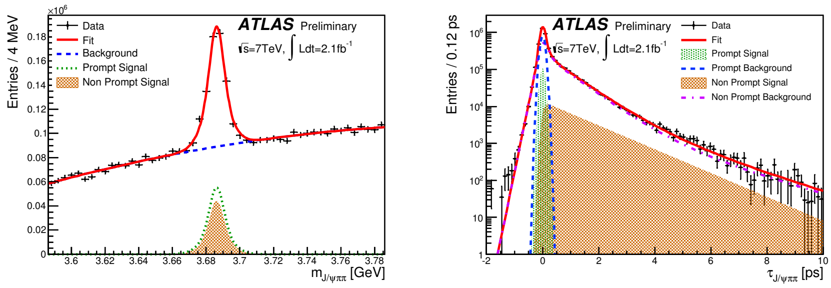

(b) $11 < |p_T| < 12$

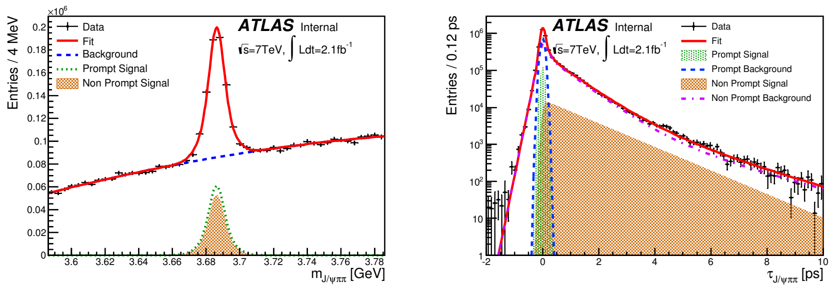

(c) $12 < |p_T| < 14$

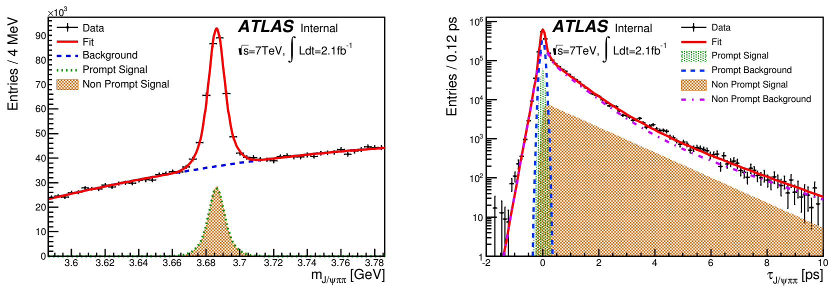

(d) $14 < |p_T| < 16$

Figure E.2: Central Fit Results for $0.00 < |y| < 0.75$.

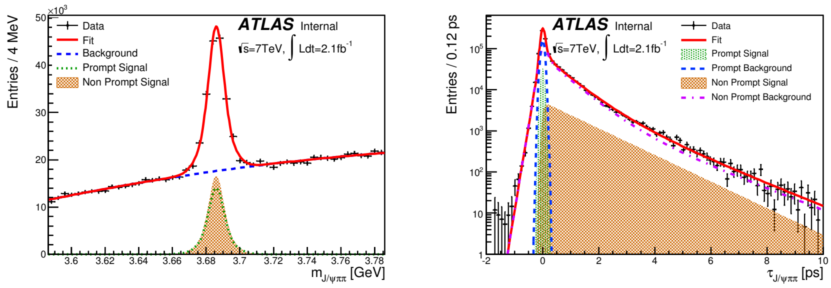

(e) $16 < |p_T| < 18$

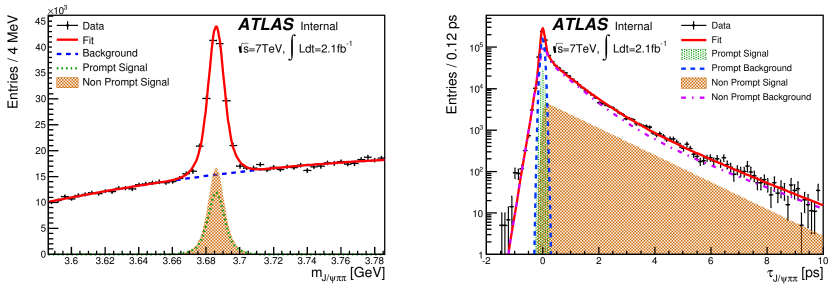

(f) $18 < |p_T| < 22$

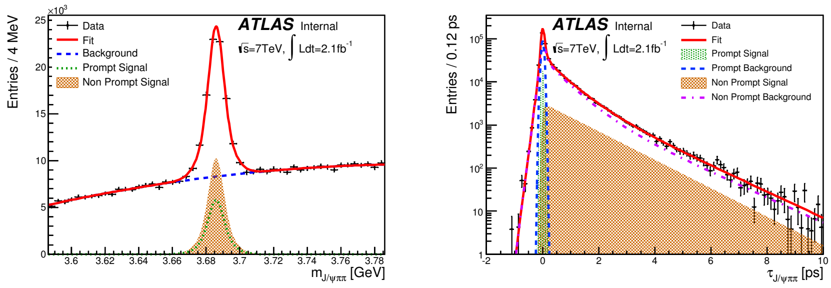

(g) $22 < |p_T| < 30$

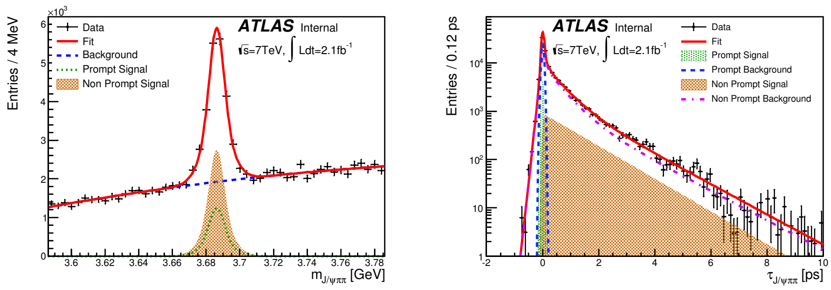

(h) $30 < |p_T| < 40$

Figure E.2: Central Fit Results for $0.00 < |y| < 0.75$ (Continued).

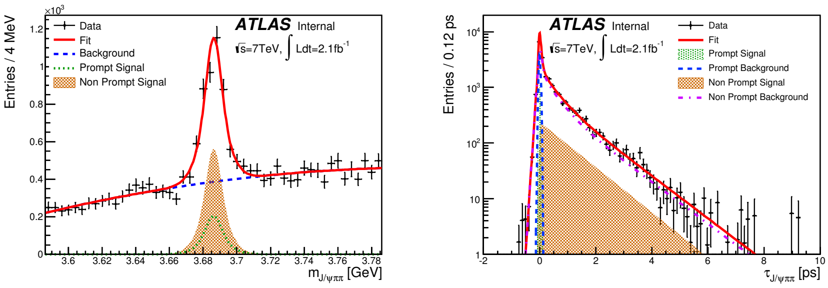

(i) $40 < |p_T| < 60$

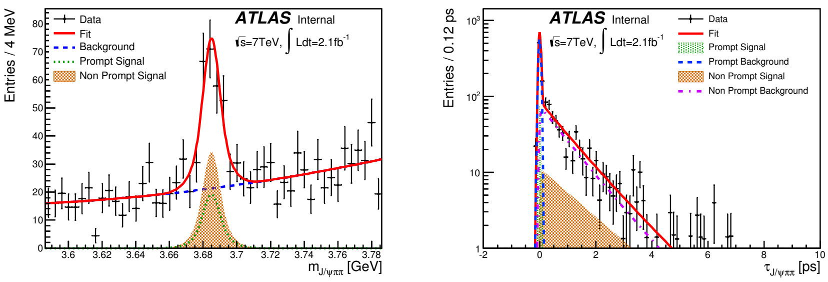

(j) $60 < |p_T| < 100$

Figure E.2: Central Fit Results for $0.00 < |y| < 0.75$ (Continued).

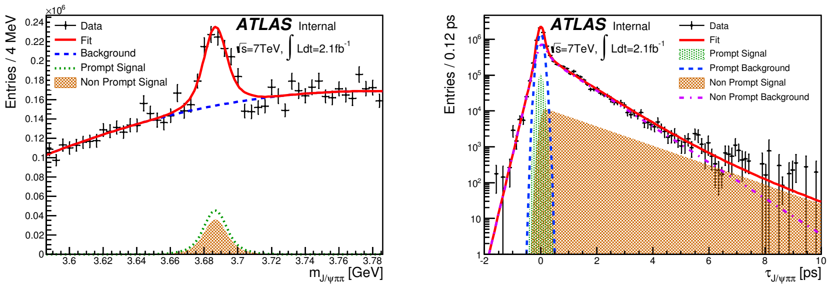

(a) $10 < |p_T| < 11$

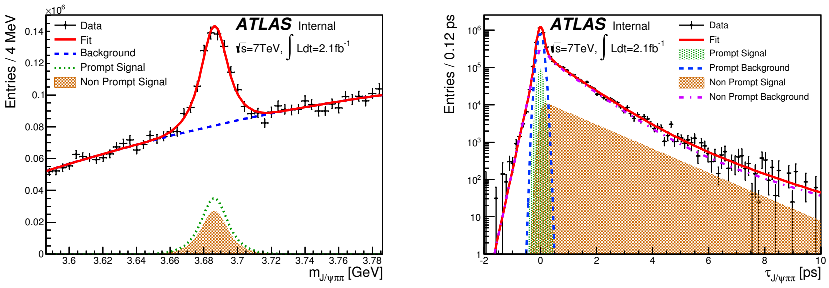

(b) $11 < |p_T| < 12$

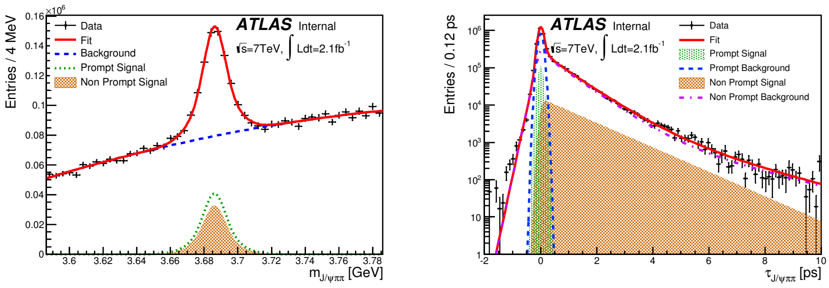

(c) $12 < |p_T| < 14$

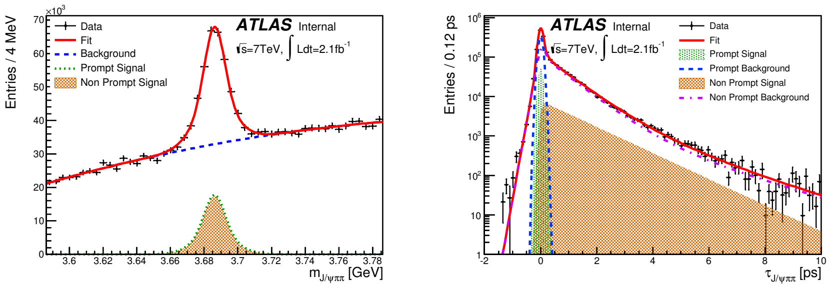

(d) $14 < |p_T| < 16$

Figure E.3: Central Fit Results for $0.75 < |y| < 1.50$.

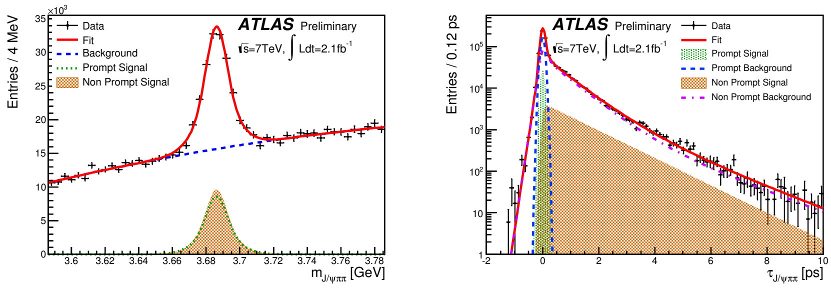

(e) $16 < |p_T| < 18$

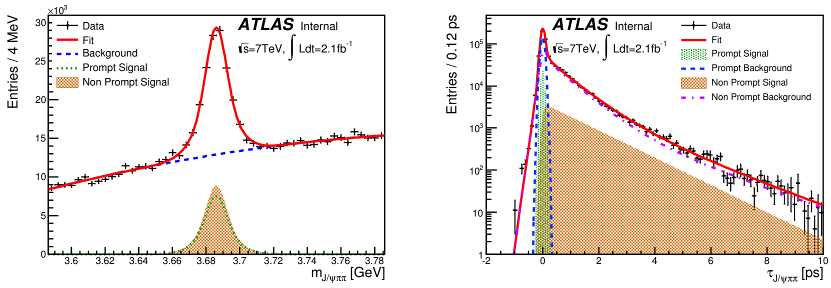

(f) $18 < |p_T| < 22$

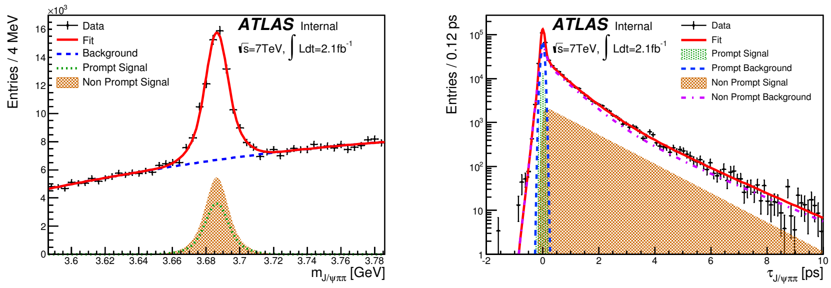

(g) $22 < |p_T| < 30$

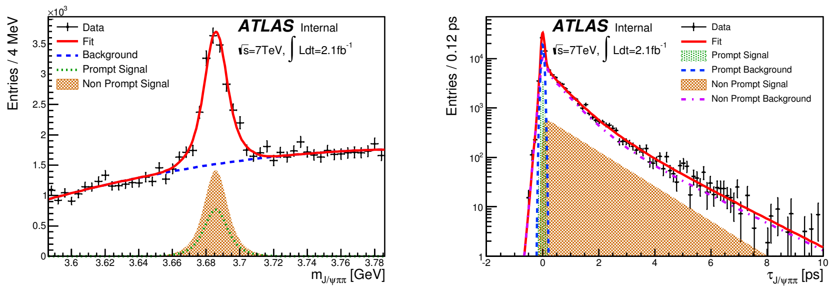

(h) $30 < |p_T| < 40$

Figure E.3: Central Fit Results for $0.75 < |y| < 1.50$ (Continued).

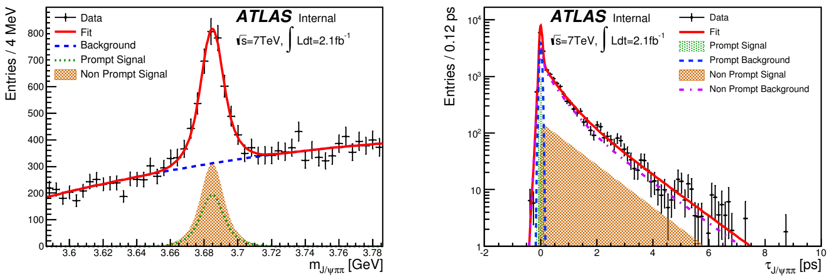

(i) $40 < |p_T| < 60$

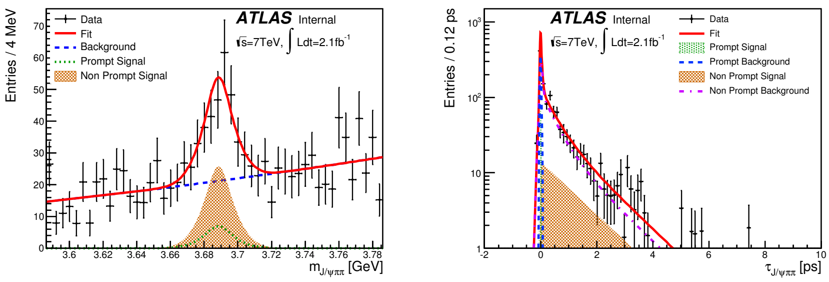

(j) $60 < |p_T| < 100$

Figure E.3: Central Fit Results for $0.75 < |y| < 1.50$ (Continued).

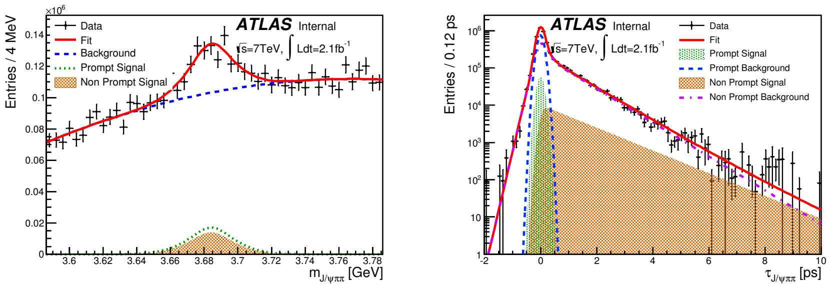

(a) $10 < |p_T| < 11$

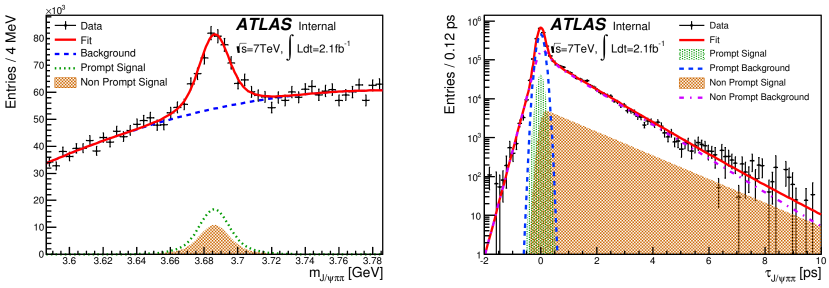

(b) $11 < |p_T| < 12$

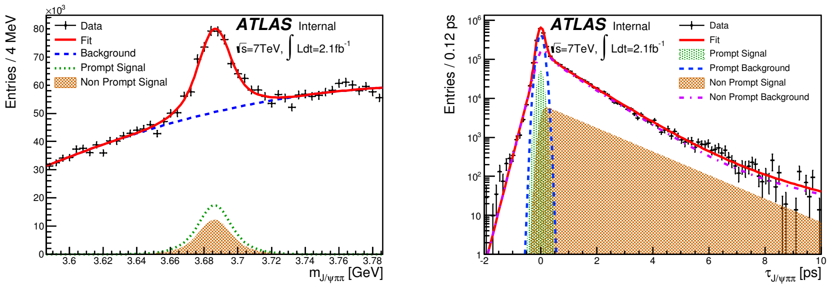

(c) $12 < |p_T| < 14$

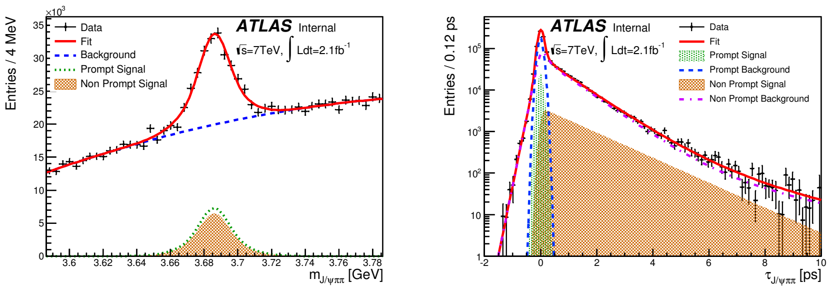

(d) $14 < |p_T| < 16$

Figure E.4: Central Fit Results for $1.50 < |y| < 2.00$.

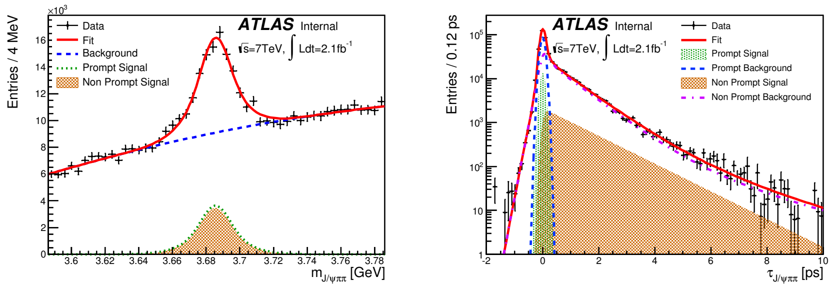

(e) $16 < |p_T| < 18$

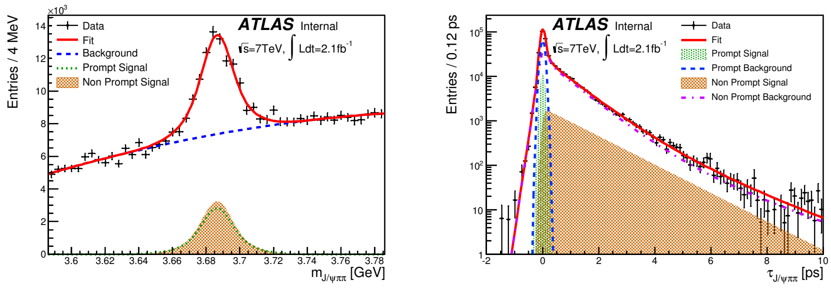

(f) $18 < |p_T| < 22$

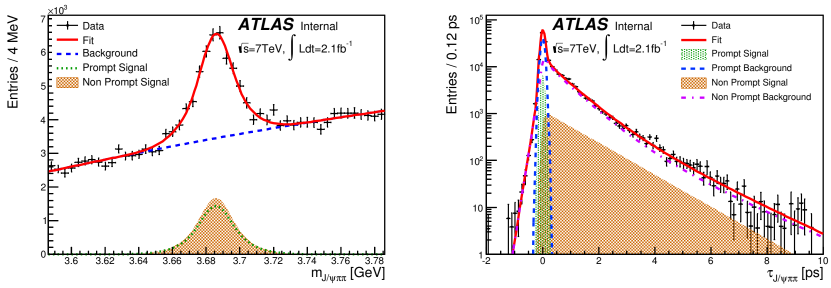

(g) $22 < |p_T| < 30$

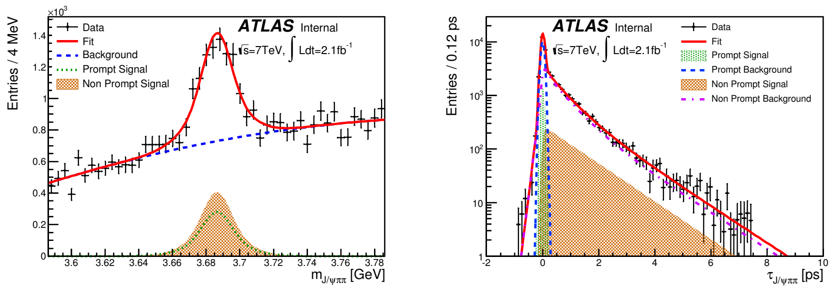

(h) $30 < |p_T| < 40$

Figure E.4: Central Fit Results for $1.50 < |y| < 2.00$ (Continued).

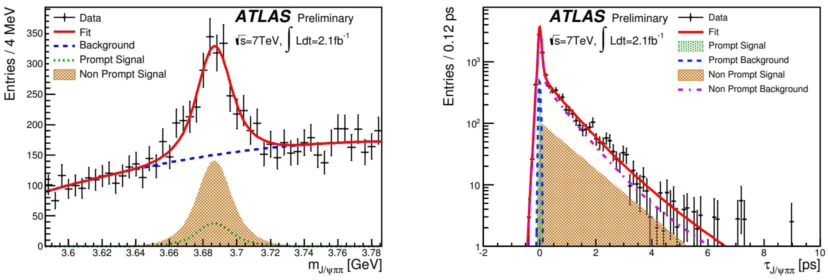

(i) $40 < |p_T| < 60$

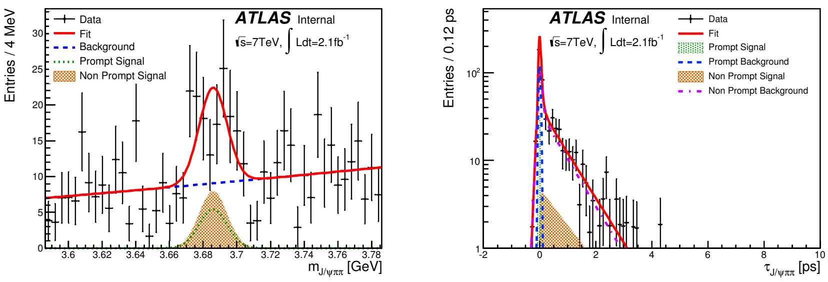

(j) $60 < |p_T| < 100$

Figure E.4: Central Fit Results for $1.50 < |y| < 2.00$ (Continued).

E.4 Example Projection

The plots in Figures E.5, E.6 and E.7 show the fitted mass distribution in slices of lifetime for the example fit plot shown in Figure 6.1. These plots are to illustrate that the mass fits is good throughout the lifetime distribution.

The plots Figures E.8, E.9 and E.10 show the fitted life distribution in slices of mass for the example fit plot shown in Figure 6.1. These plots are to illustrate that the lifetime fits is good throughout the mass distribution.

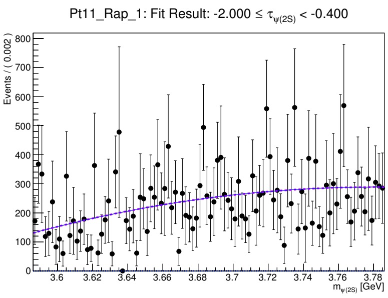

(a) $-2.0 < \tau_{\psi(2S)} < -0.4$

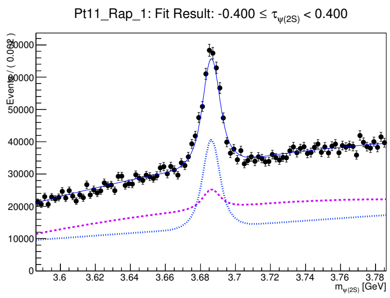

(b) $-0.4 < \tau_{\psi(2S)} < 0.4$

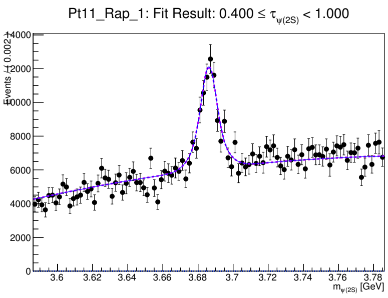

(c) $0.4 < \tau_{\psi(2S)} < 1.0$

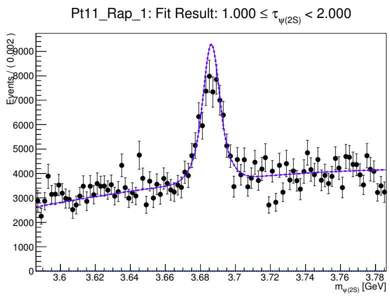

(d) $1.0 < \tau_{\psi(2S)} < 2.0$

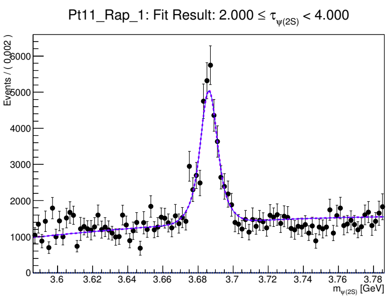

(e) $2.0 < \tau_{\psi(2S)} < 4.0$

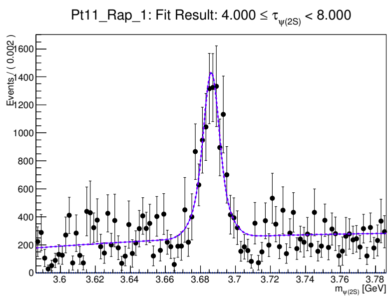

(f) $4.0 < \tau_{\psi(2S)} < 8.0$

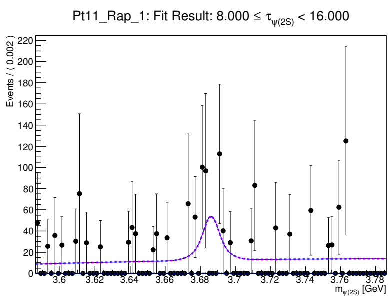

(g) $8.0 < \tau_{\psi(2S)} < 16.0$

Figure E.5: Mass distribution in projection of lifetime for the bin $11 < |p_T| < 12$, $0.00 < |y| < 0.75$.

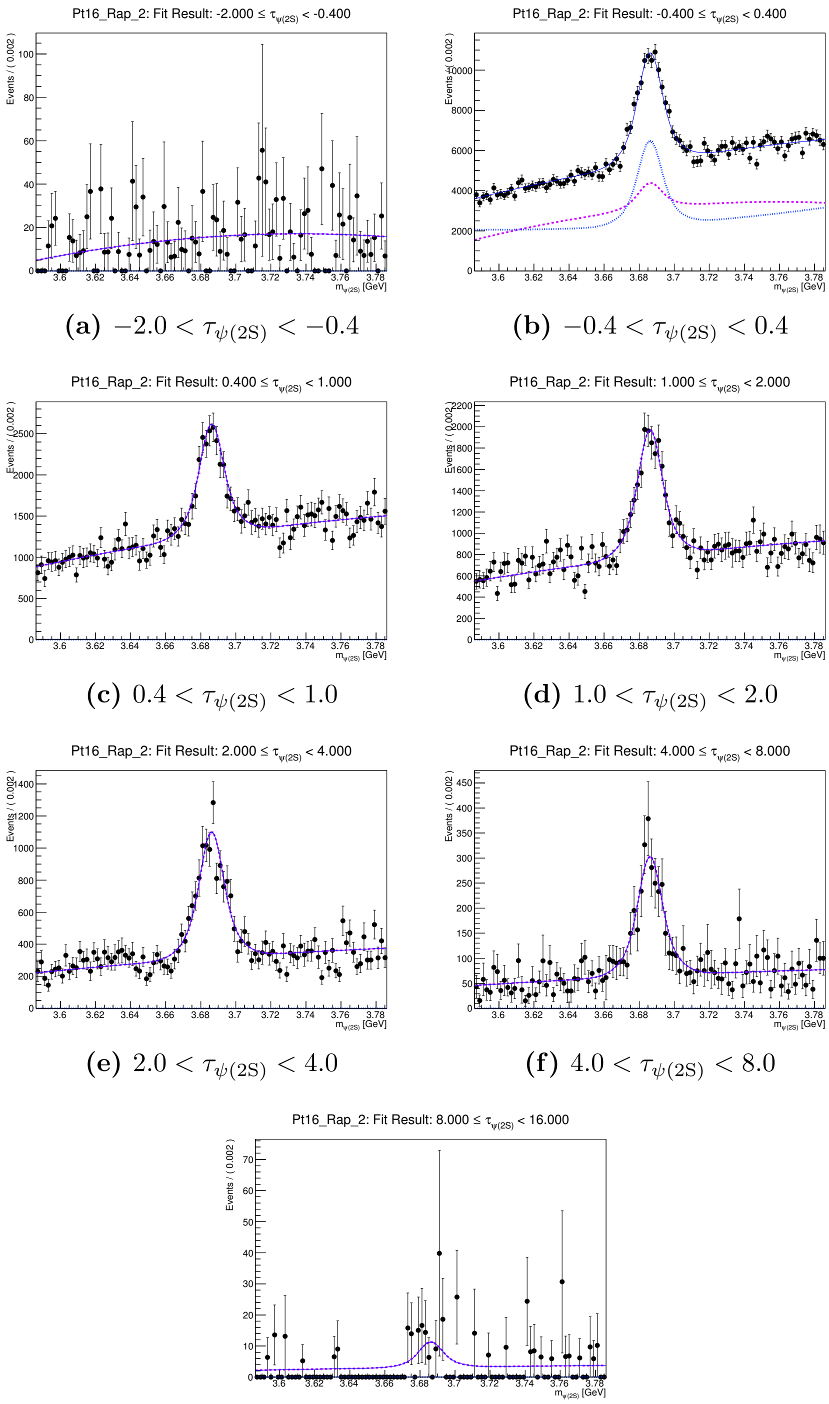

(a) $-2.0 < \tau_{\psi(2S)} < -0.4$

(b) $-0.4 < \tau_{\psi(2S)} < 0.4$

(c) $0.4 < \tau_{\psi(2S)} < 1.0$

(d) $1.0 < \tau_{\psi(2S)} < 2.0$

(e) $2.0 < \tau_{\psi(2S)} < 4.0$

(f) $4.0 < \tau_{\psi(2S)} < 8.0$

(g) $8.0 < \tau_{\psi(2S)} < 16.0$

Figure E.6: Mass distribution in projection of lifetime for the bin $16 < |p_T| < 18$, $0.75 < |y| < 1.5$.

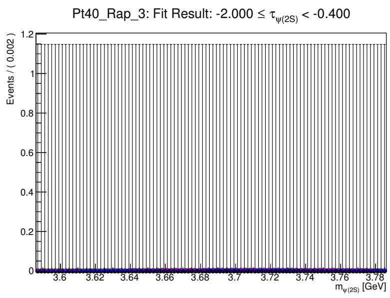

(a) $-2.0 < \tau_{\psi(2\mathrm{S})} < -0.4$

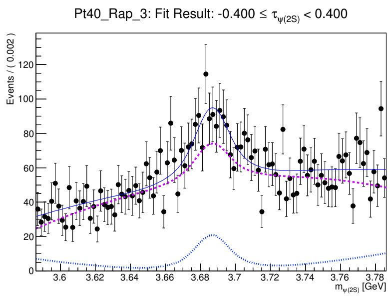

(b) $-0.4 < \tau_{\psi(2\mathrm{S})} < 0.4$

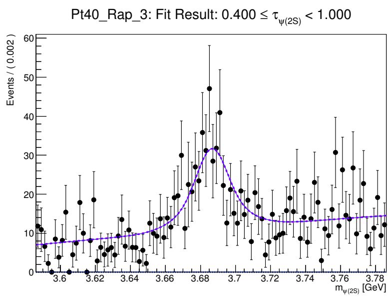

(c) $0.4 < \tau_{\psi(2\mathrm{S})} < 1.0$

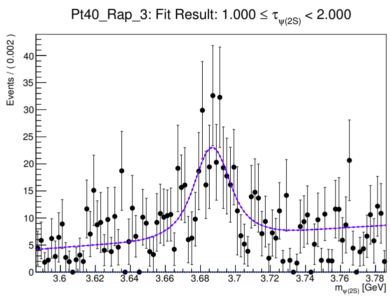

(d) $1.0 < \tau_{\psi(2\mathrm{S})} < 2.0$

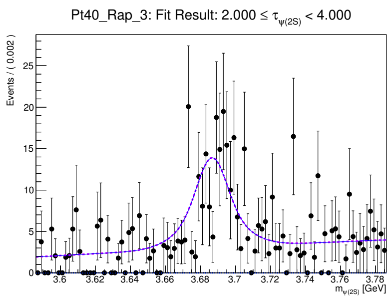

(e) $2.0 < \tau_{\psi(2\mathrm{S})} < 4.0$

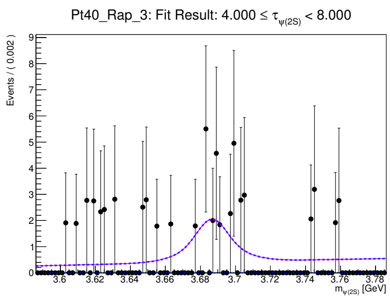

(f) $4.0 < \tau_{\psi(2\mathrm{S})} < 8.0$

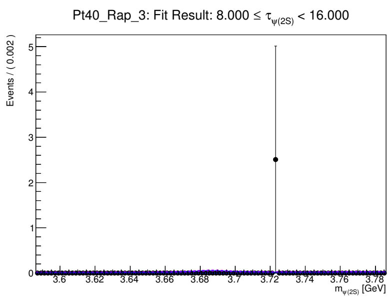

(g) $8.0 < \tau_{\psi(2\mathrm{S})} < 16.0$

Figure E.7: Mass distribution in projection of lifetime for the bin $40 < |p_T| < 60$, $1.5 < |y| < 2.0$.

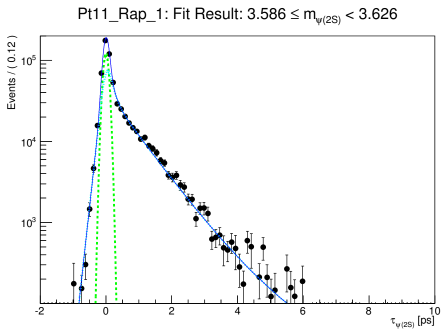

(a) $3.586 < m_{\psi(2S)} < 3.626$

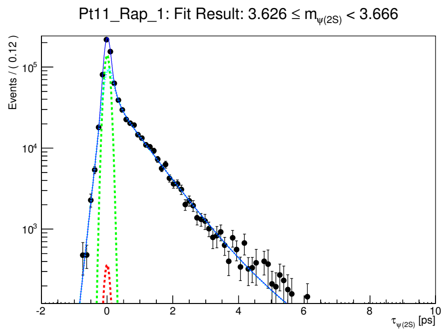

(b) $3.626 < m_{\psi(2S)} < 3.666$

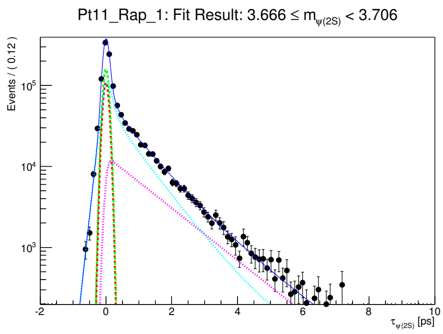

(c) $3.666 < m_{\psi(2S)} < 3.706$

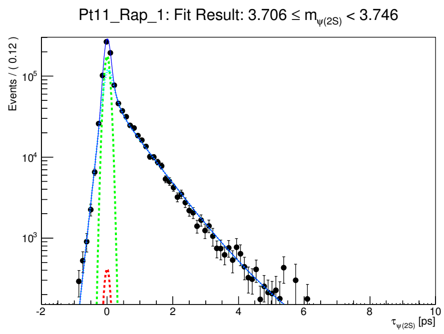

(d) $3.706 < m_{\psi(2S)} < 3.746$

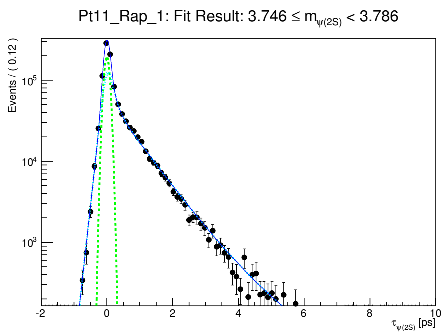

(e) $3.746 < m_{\psi(2S)} < 3.786$

Figure E.8: Lifetime distribution in projection on mass for the bin $11 < |p_T| < 12$, $0.00 < |y| < 0.75$.

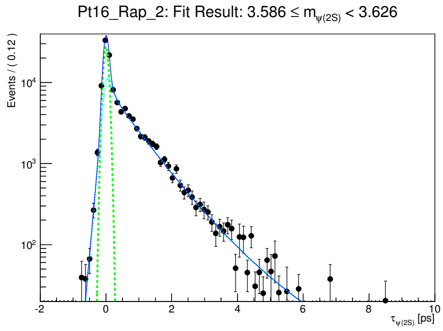

(a) $3.586 < m_{\psi(2S)} < 3.626$

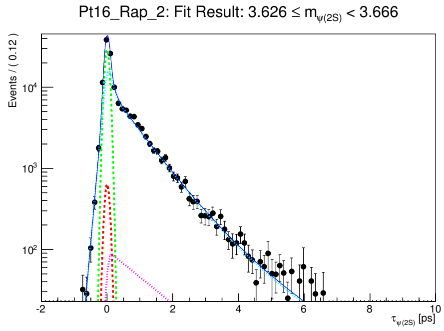

(b) $3.626 < m_{\psi(2S)} < 3.666$

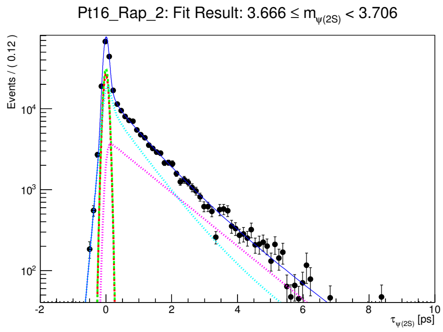

(c) $3.666 < m_{\psi(2S)} < 3.706$

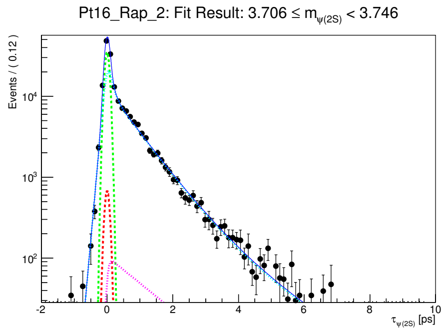

(d) $3.706 < m_{\psi(2S)} < 3.746$

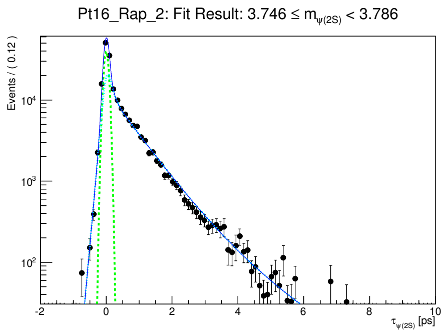

(e) $3.746 < m_{\psi(2S)} < 3.786$

Figure E.9: Lifetime distribution in projection on mass for the bin $16 < |p_T| < 18$, $0.75 < |y| < 1.5$.

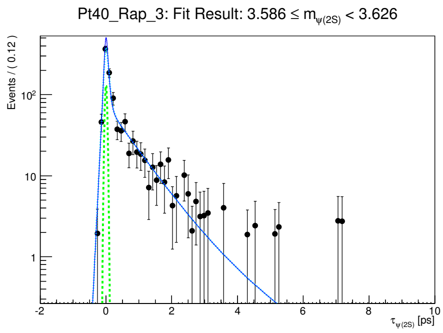

(a) $3.586 < m_{\psi(2S)} < 3.626$

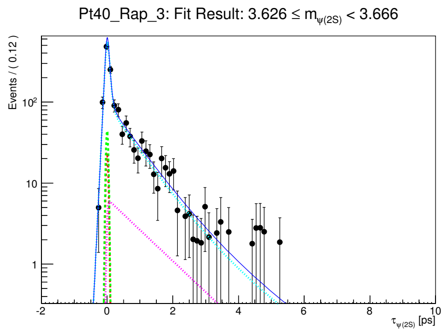

(b) $3.626 < m_{\psi(2S)} < 3.666$

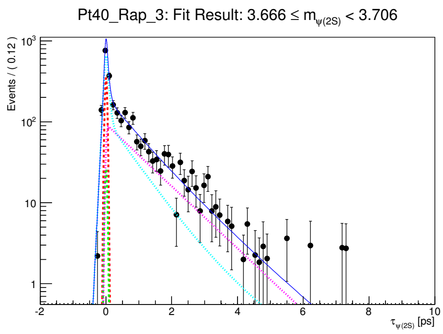

(c) $3.666 < m_{\psi(2S)} < 3.706$

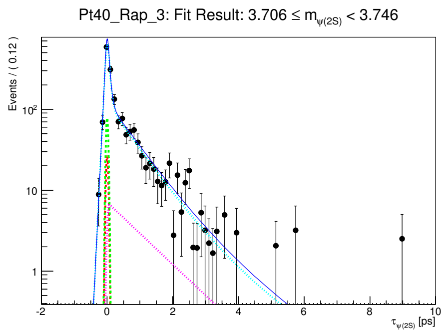

(d) $3.706 < m_{\psi(2S)} < 3.746$

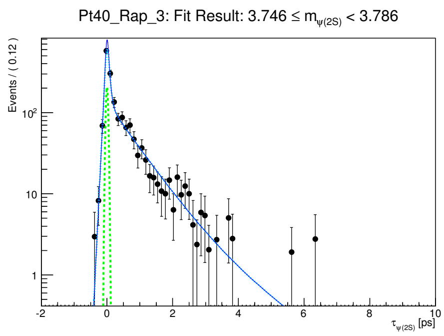

(e) $3.746 < m_{\psi(2S)} < 3.786$

Figure E.10: Lifetime distribution in projection on mass for the bin $40 < |p_T| < 60$, $1.5 < |y| < 2.0$.

E.5 Systematic Fits

Shown in this section are the fitted yield distributions for prompt (left) and non-prompt (right), from the pseudo-experiments for the muon reconstruction, pion reconstruction and trigger efficiencies. The results of these fits are incorporated into Figures 6.2, 6.3 and 6.4.

E.5.1 Muons

The fitted yields from the muon reconstruction efficiency map created by the pseudo-experiments, Figures E.11, E.12 & E.13.

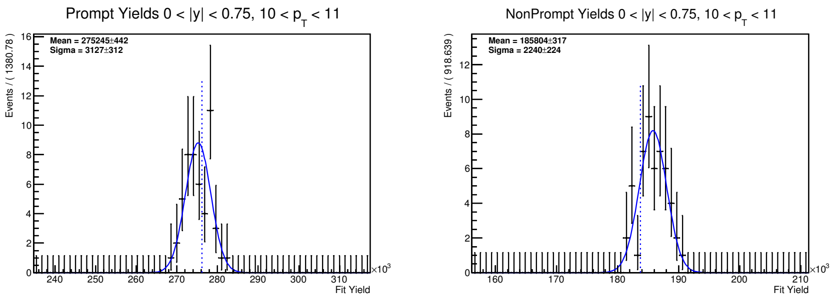

(a) $10 < |p_T| < 11$

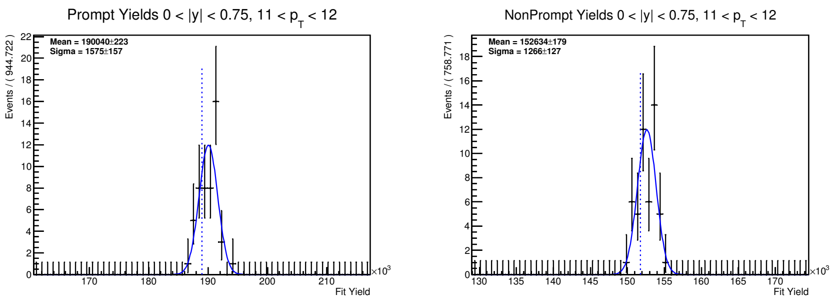

(b) $11 < |p_T| < 12$

Figure E.11: Muon Reconstruction Uncertainty for $0.00 < |y| < 0.75$.

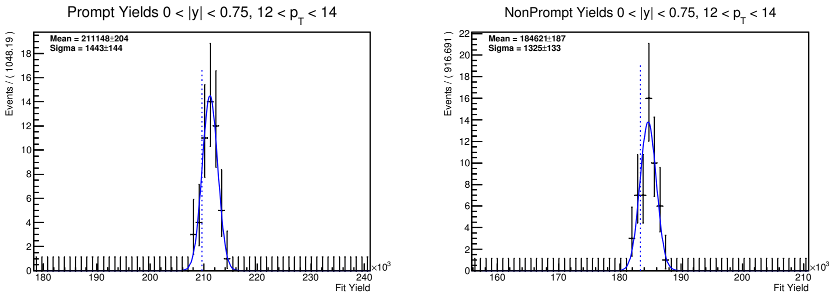

(c) $12 < |p_T| < 14$

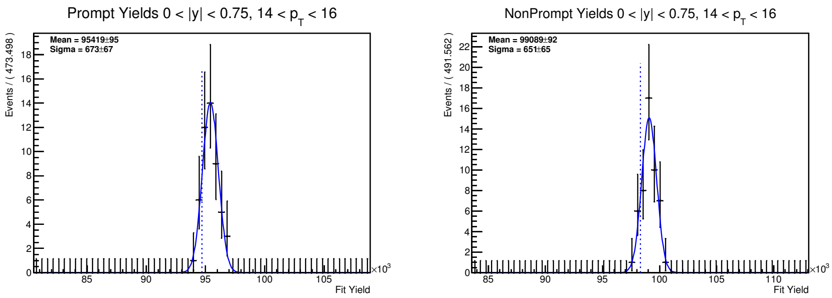

(d) $14 < |p_T| < 16$

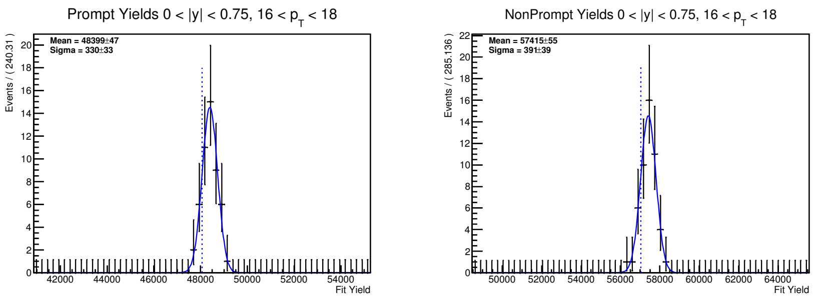

(e) $16 < |p_T| < 18$

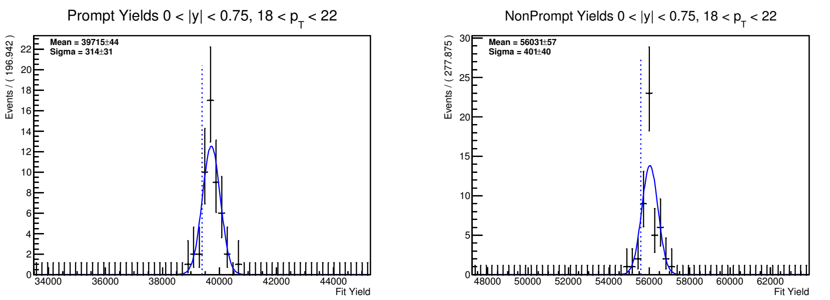

(f) $18 < |p_T| < 22$

Figure E.11: Muon Reconstruction Uncertainty for $0.00 < |y| < 0.75$ (Continued).

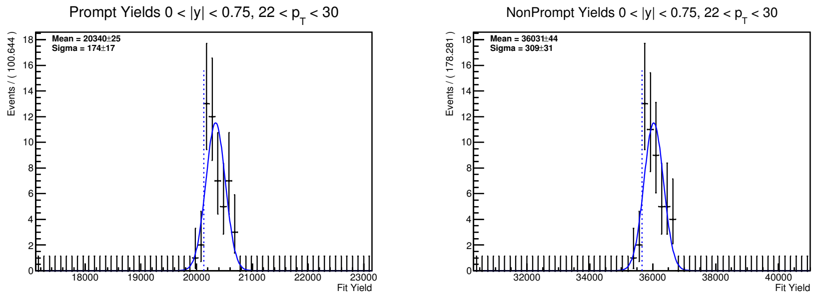

(g) $22 < |p_T| < 30$

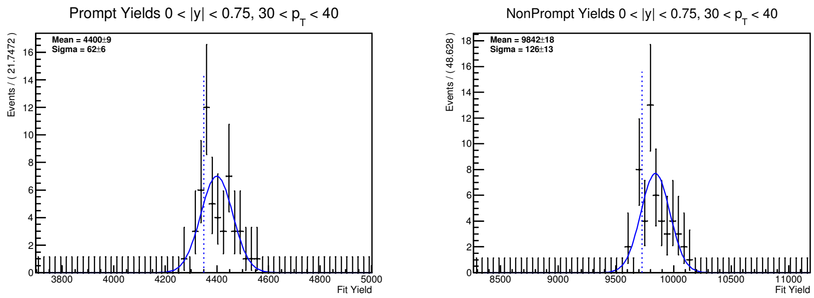

(h) $30 < |p_T| < 40$

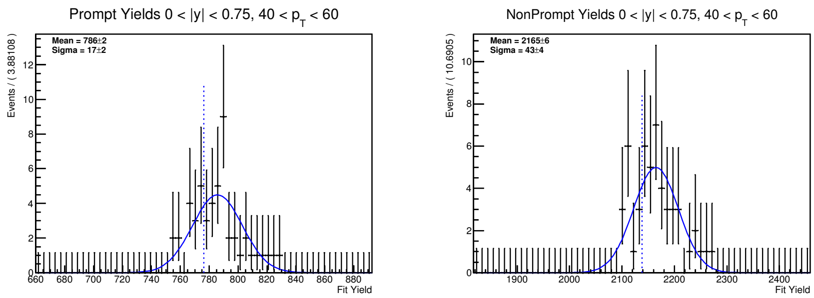

(i) $40 < |p_T| < 60$

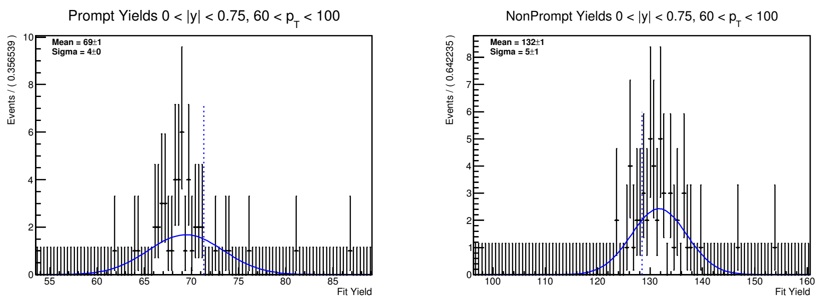

(j) $60 < |p_T| < 100$

Figure E.11: Muon Reconstruction Uncertainty for $0.00 < |y| < 0.75$ (Continued).

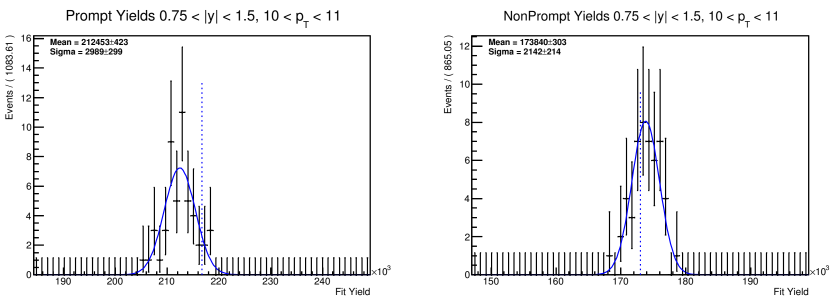

(a) $10 < |p_T| < 11$

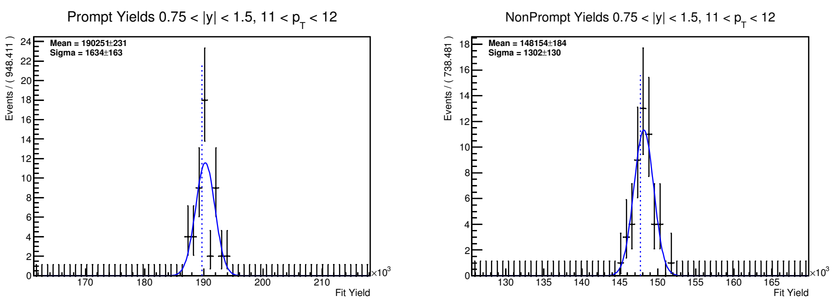

(b) $11 < |p_T| < 12$

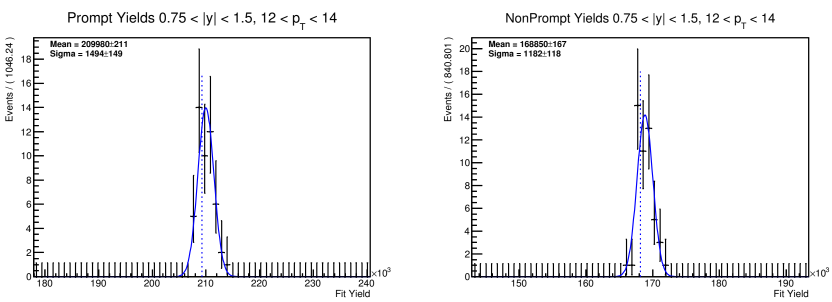

(c) $12 < |p_T| < 14$

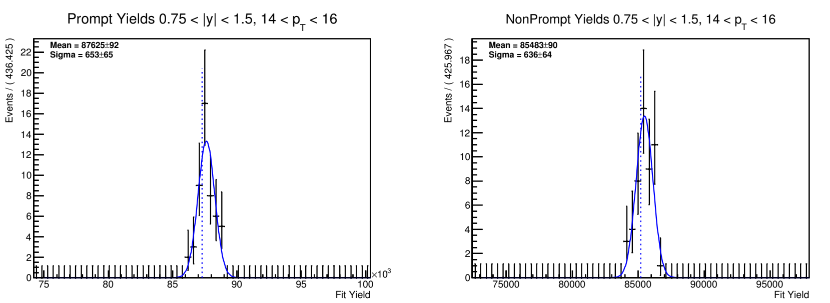

(d) $14 < |p_T| < 16$

Figure E.12: Muon Reconstruction Uncertainty for $0.75 < |y| < 1.50$.

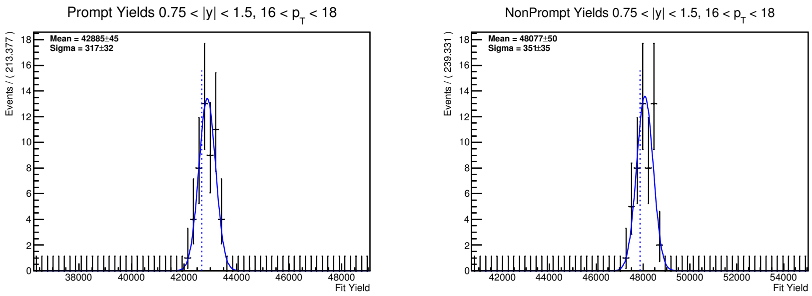

(e) $16 < |p_T| < 18$

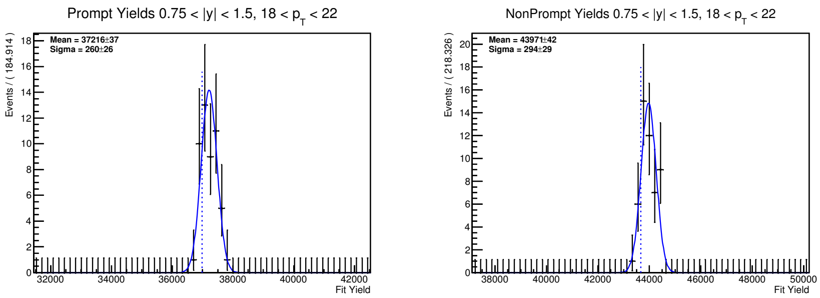

(f) $18 < |p_T| < 22$

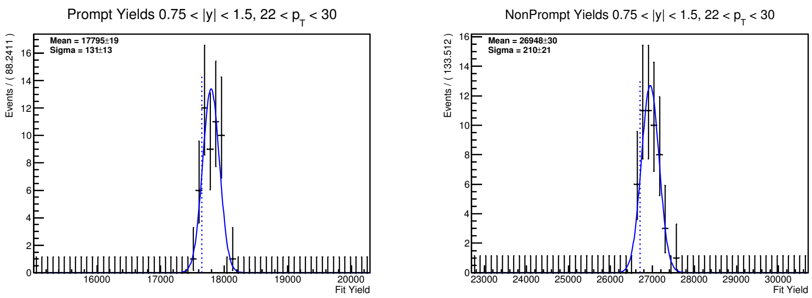

(g) $22 < |p_T| < 30$

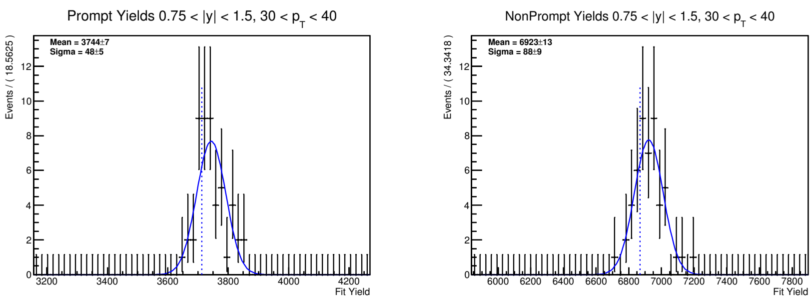

(h) $30 < |p_T| < 40$

Figure E.12: Muon Reconstruction Uncertainty for $0.75 < |y| < 1.50$ (Continued).

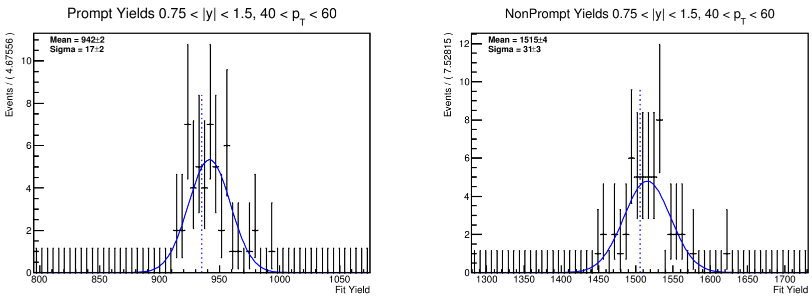

(i) $40 < |p_T| < 60$

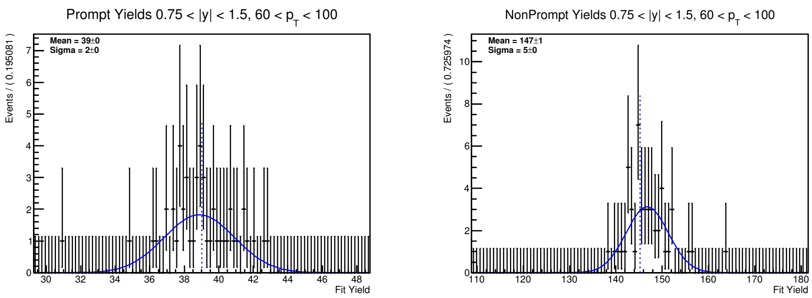

(j) $60 < |p_T| < 100$

Figure E.12: Muon Reconstruction Uncertainty for $0.75 < |y| < 1.50$ (Continued).

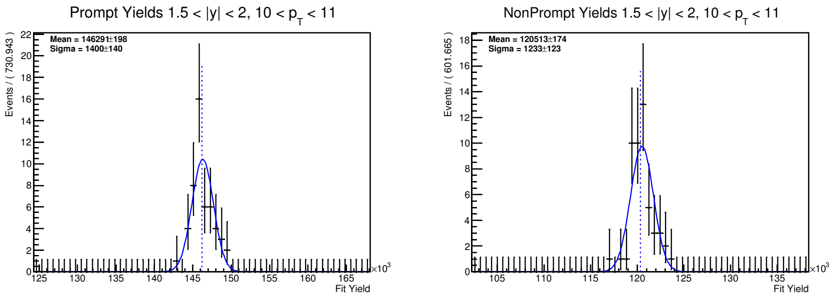

(a) $10 < |p_T| < 11$

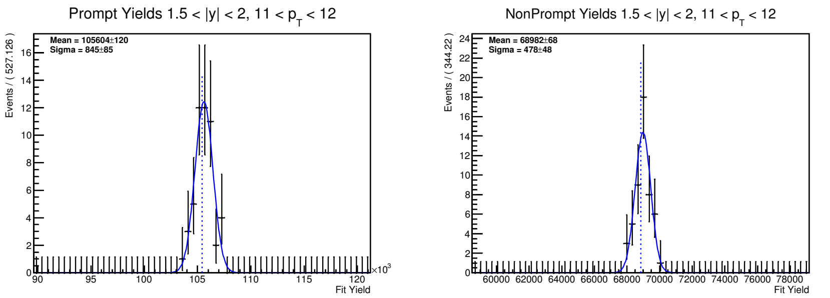

(b) $11 < |p_T| < 12$

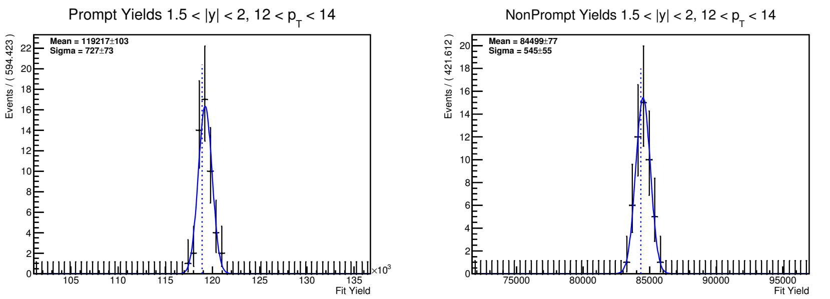

(c) $12 < |p_T| < 14$

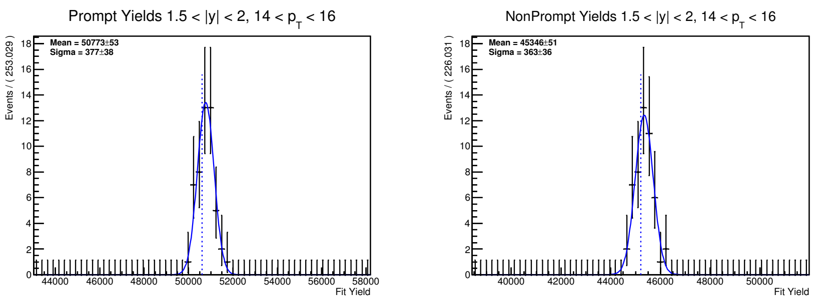

(d) $14 < |p_T| < 16$

Figure E.13: Muon Reconstruction Uncertainty for $1.50 < |y| < 2.00$.

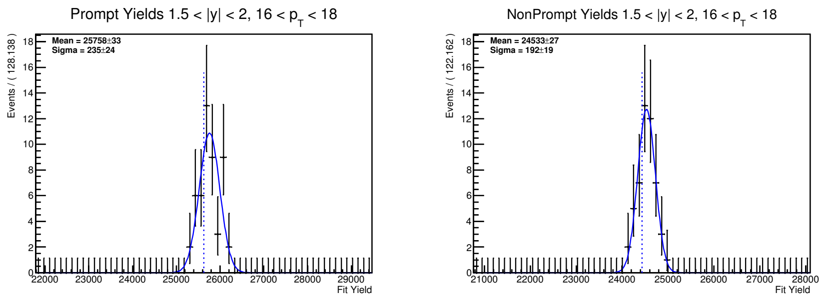

(e) $16 < |p_T| < 18$

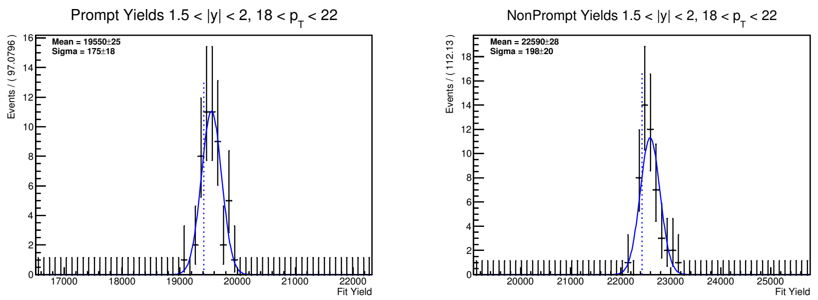

(f) $18 < |p_T| < 22$

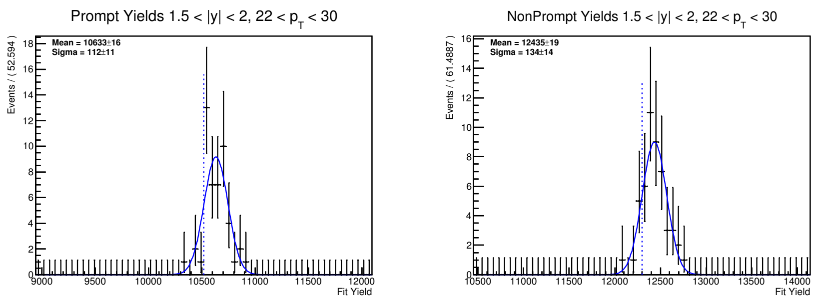

(g) $22 < |p_T| < 30$

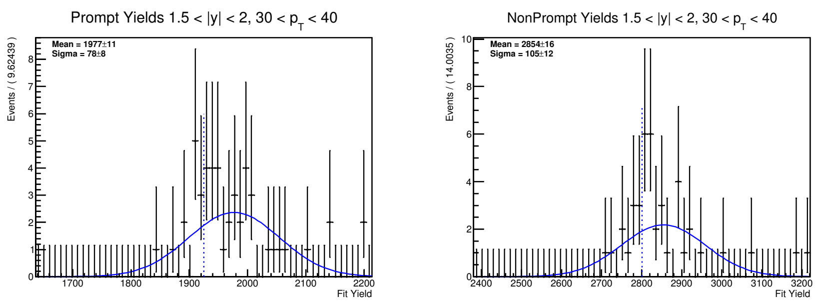

(h) $30 < |p_T| < 40$

Figure E.13: Muon Reconstruction Uncertainty for $1.50 < |y| < 2.00$ (Continued).

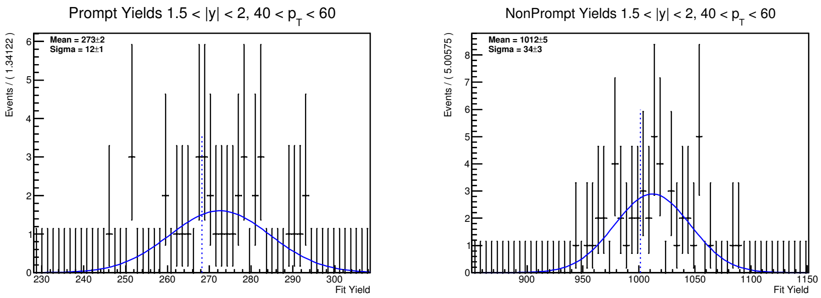

(i) $40 < |p_T| < 60$

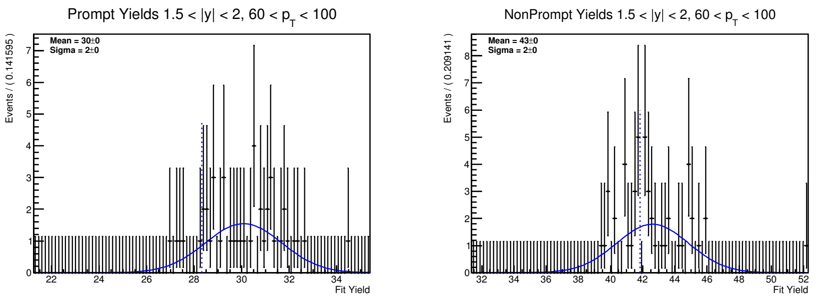

(j) $60 < |p_T| < 100$

Figure E.13: Muon Reconstruction Uncertainty for $1.50 < |y| < 2.00$ (Continued).

E.5.2 Pions

The fitted yields from the pion reconstruction efficiency map created by the pseudo-experiments, Figures E.14, E.15 & E.16.

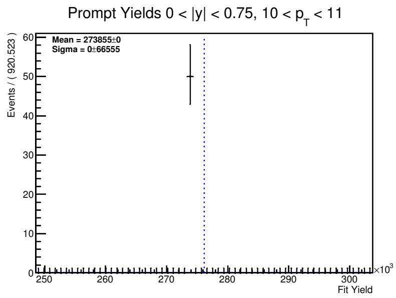

(a) $10 < |p_T| < 11$

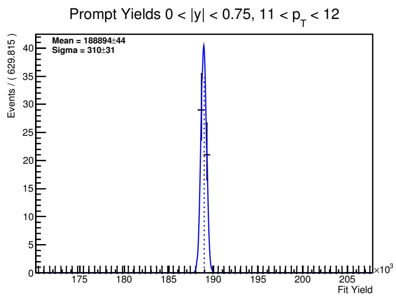

(b) $11 < |p_T| < 12$

Figure E.14: Pion Reconstruction Uncertainty for $0.00 < |y| < 0.75$.

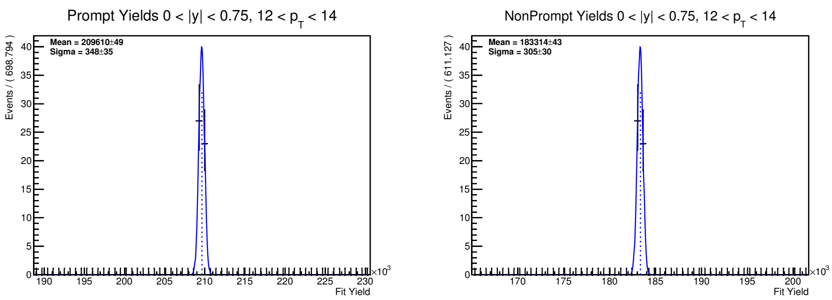

(c) $12 < |p_T| < 14$

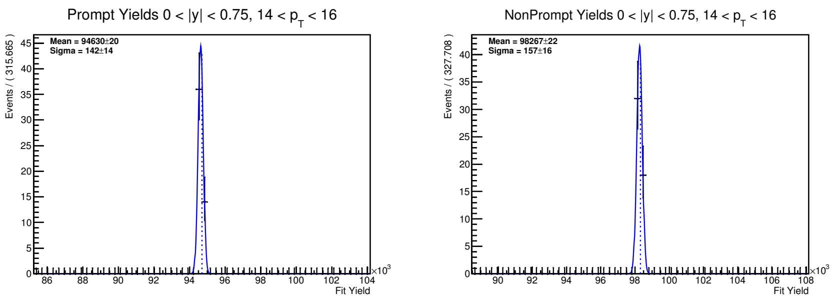

(d) $14 < |p_T| < 16$

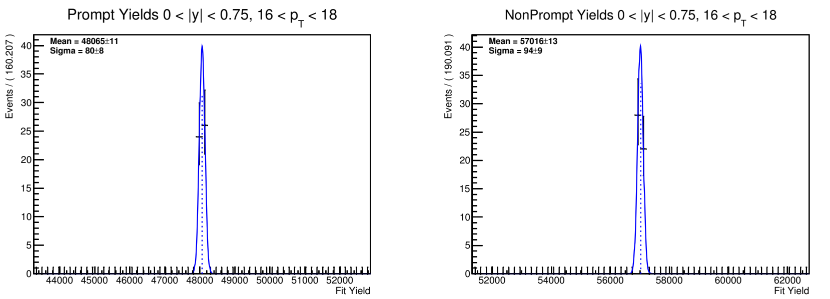

(e) $16 < |p_T| < 18$

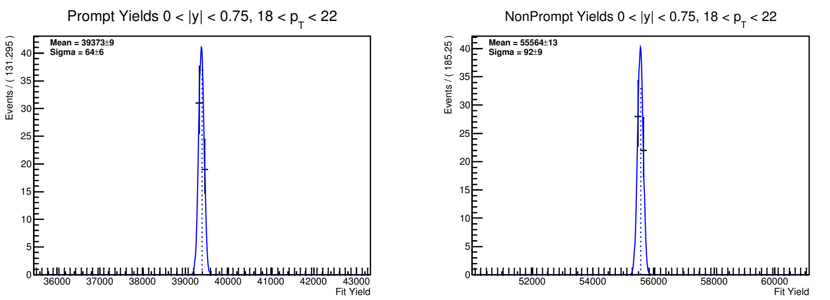

(f) $18 < |p_T| < 22$

Figure E.14: Pion Reconstruction Uncertainty for $0.00 < |y| < 0.75$ (Continued).

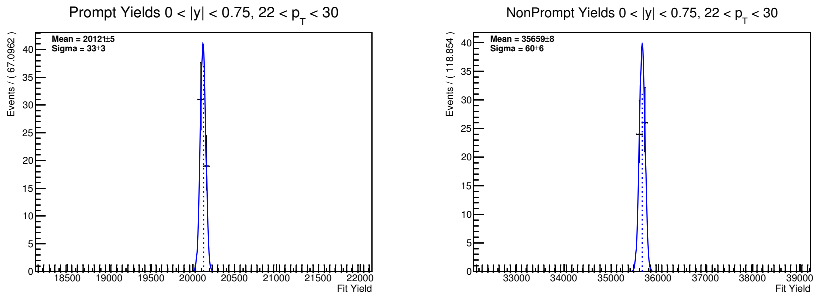

(g) $22 < |p_T| < 30$

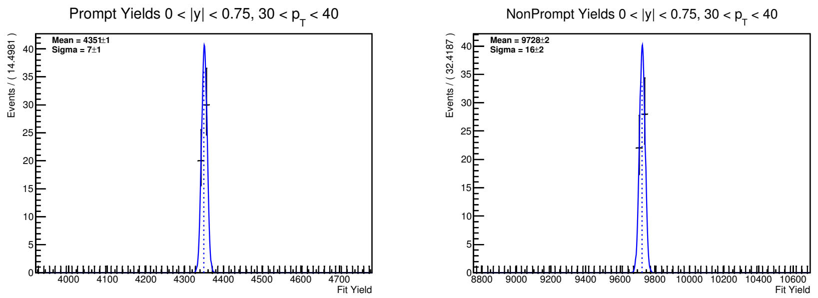

(h) $30 < |p_T| < 40$

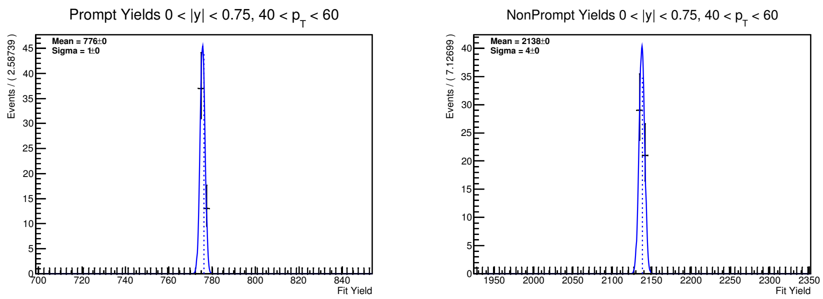

(i) $40 < |p_T| < 60$

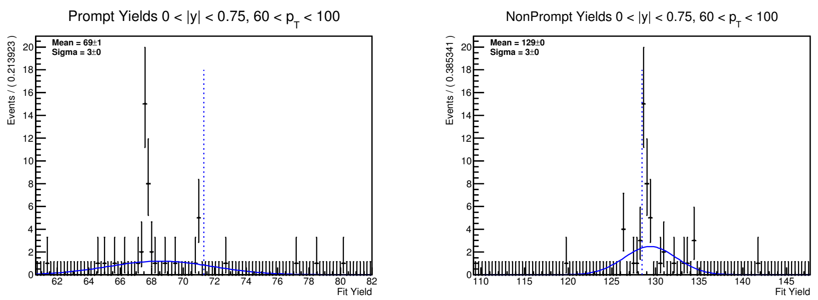

(j) $60 < |p_T| < 100$

Figure E.14: Pion Reconstruction Uncertainty for $0.00 < |y| < 0.75$ (Continued).

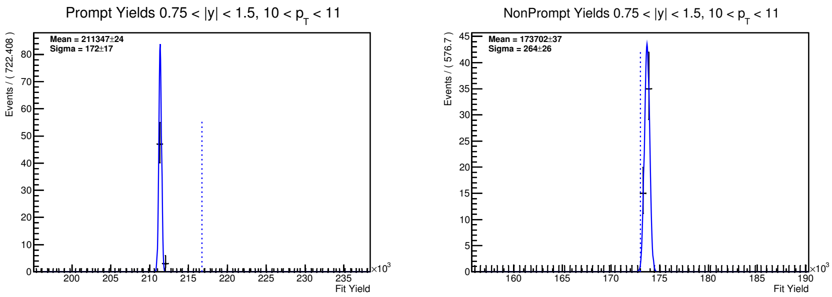

(a) $10 < |p_T| < 11$

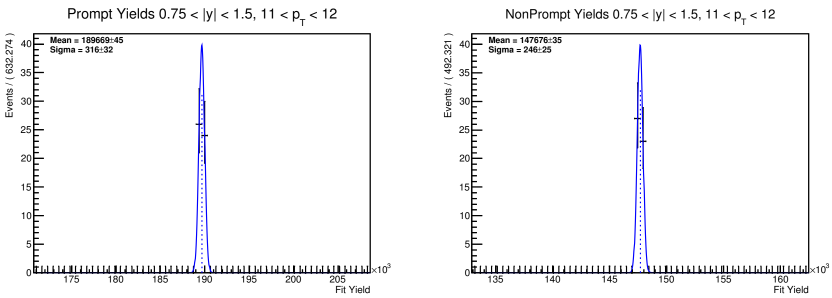

(b) $11 < |p_T| < 12$

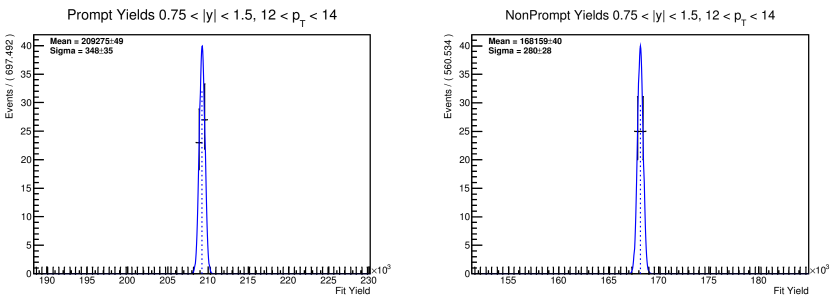

(c) $12 < |p_T| < 14$

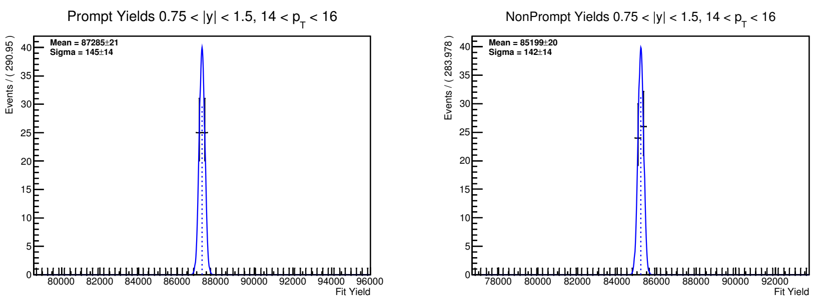

(d) $14 < |p_T| < 16$

Figure E.15: Pion Reconstruction Uncertainty for $0.75 < |y| < 1.50$.

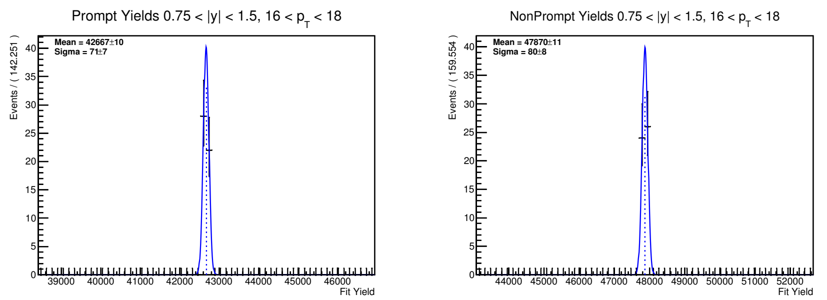

(e) $16 < |p_T| < 18$

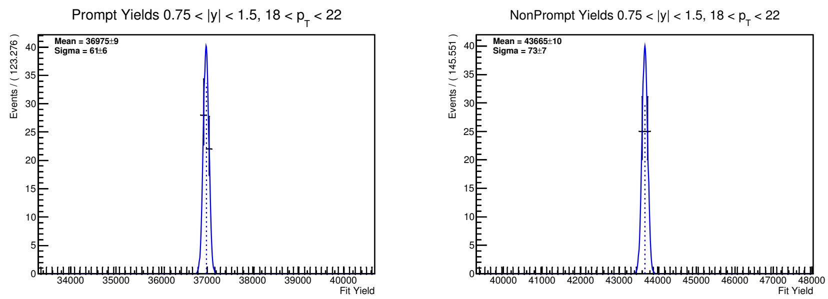

(f) $18 < |p_T| < 22$

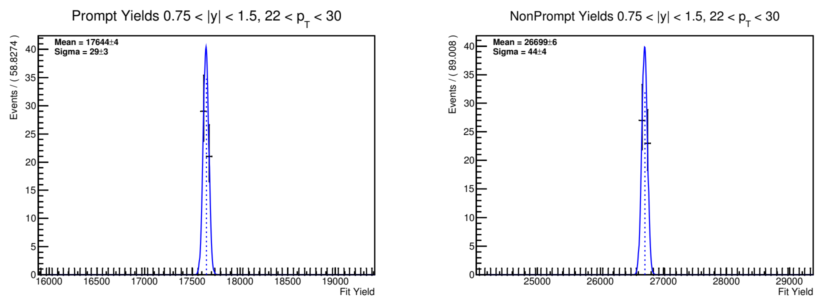

(g) $22 < |p_T| < 30$

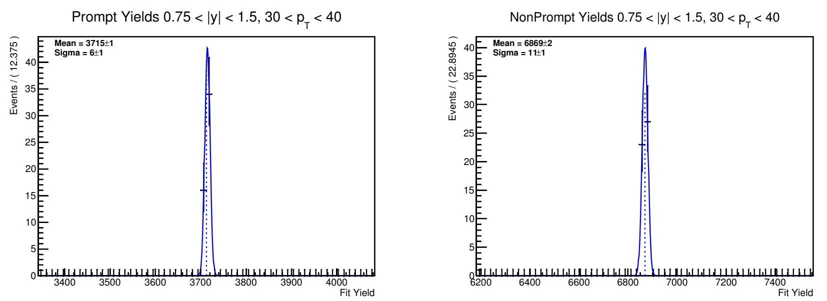

(h) $30 < |p_T| < 40$

Figure E.15: Pion Reconstruction Uncertainty for $0.75 < |y| < 1.50$ (Continued).

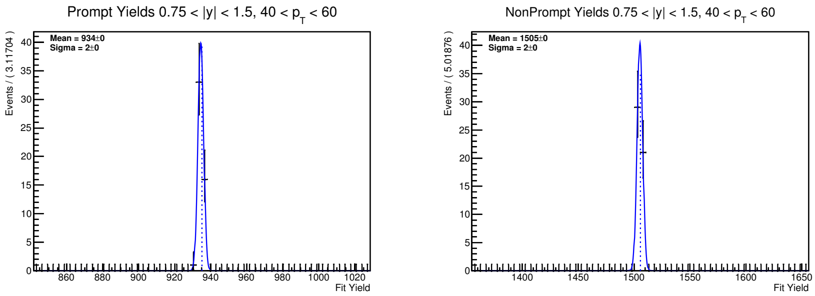

(i) $40 < |p_T| < 60$

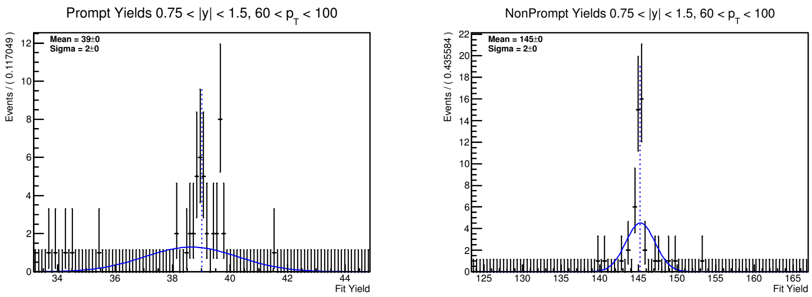

(j) $60 < |p_T| < 100$

Figure E.15: Pion Reconstruction Uncertainty for $0.75 < |y| < 1.50$ (Continued).

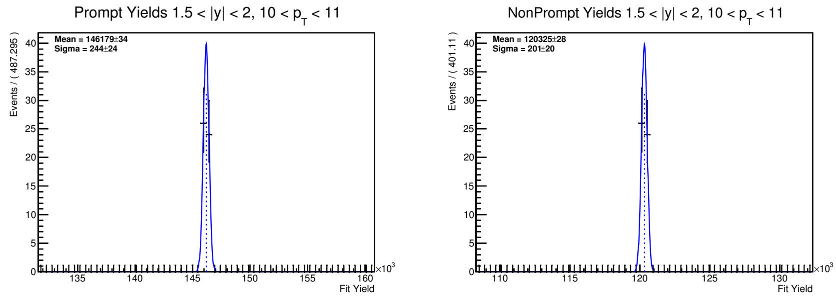

(a) $10 < |p_T| < 11$

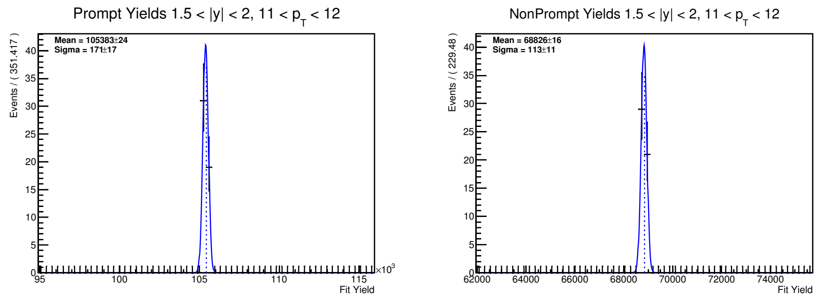

(b) $11 < |p_T| < 12$

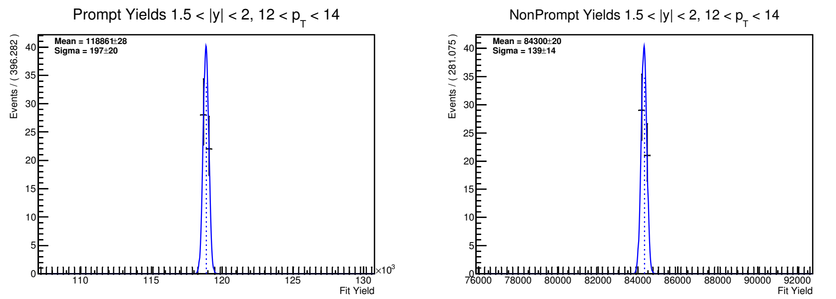

(c) $12 < |p_T| < 14$

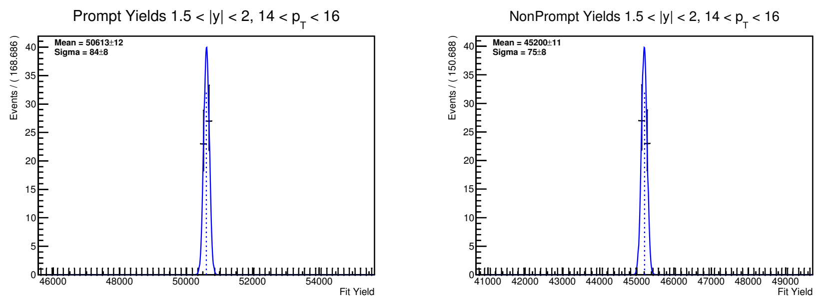

(d) $14 < |p_T| < 16$

Figure E.16: Pion Reconstruction Uncertainty for $1.50 < |y| < 2.00$.

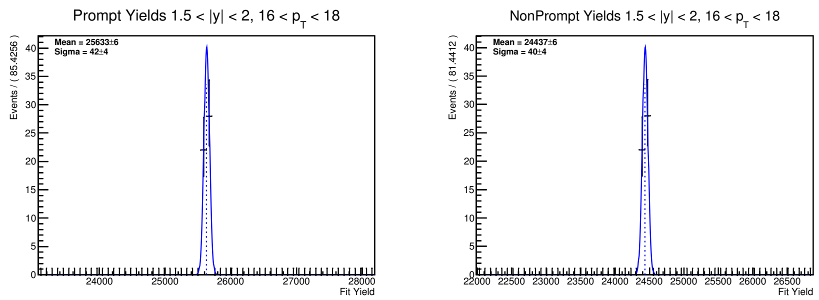

(e) $16 < |p_T| < 18$

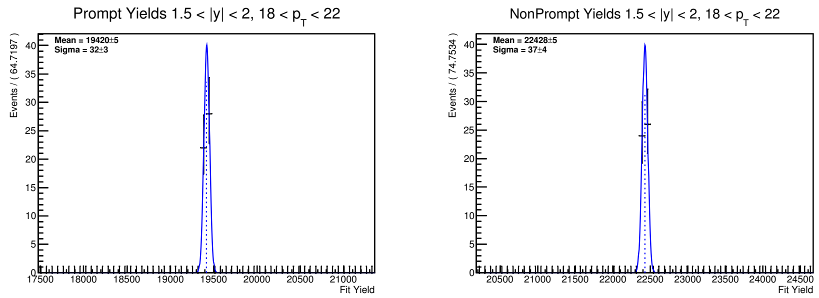

(f) $18 < |p_T| < 22$

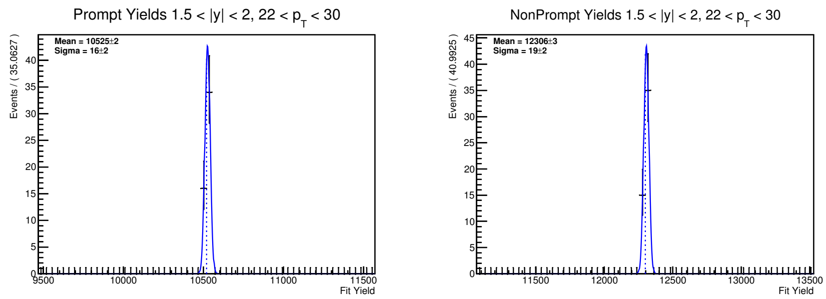

(g) $22 < |p_T| < 30$

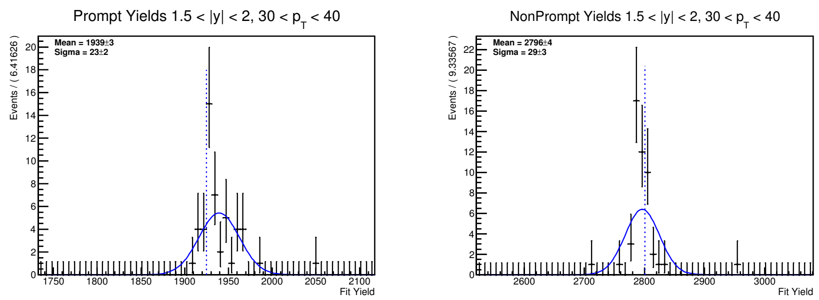

(h) $30 < |p_T| < 40$

Figure E.16: Pion Reconstruction Uncertainty for $1.50 < |y| < 2.00$ (Continued).

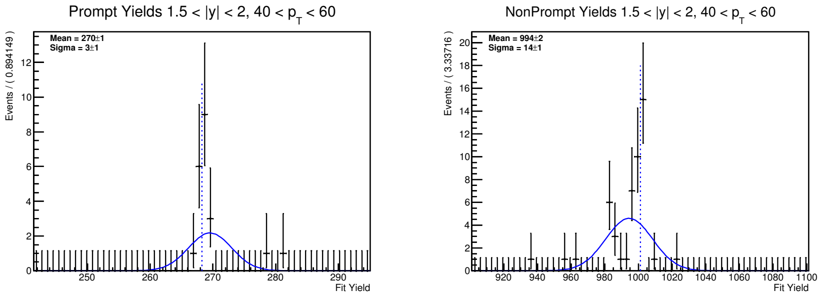

(i) $40 < |p_T| < 60$

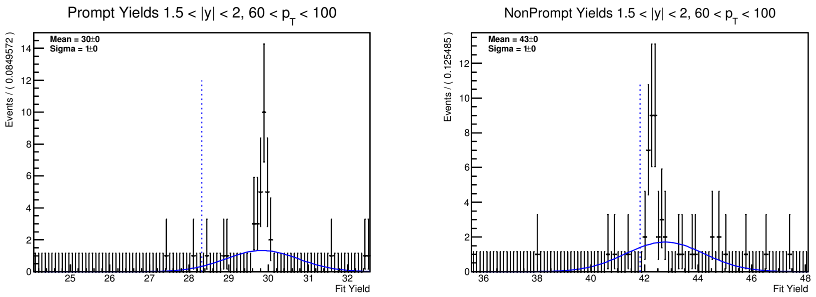

(j) $60 < |p_T| < 100$

Figure E.16: Pion Reconstruction Uncertainty for $1.50 < |y| < 2.00$ (Continued).

E.5.3 Trigger

The fitted yields from the trigger efficiency map created by the pseudo-experiments, Figures E.17, E.18 & E.19.

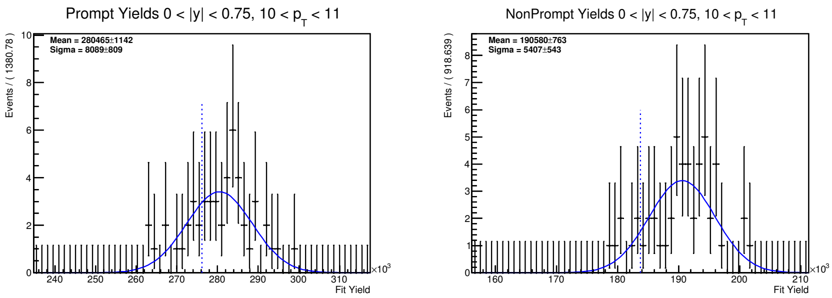

(a) $10 < |p_T| < 11$

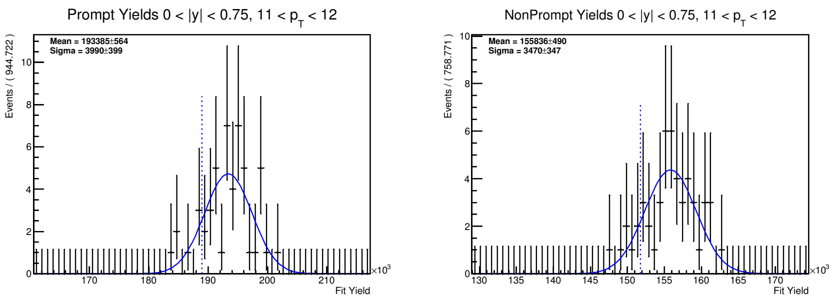

(b) $11 < |p_T| < 12$

Figure E.17: Trigger Reconstruction Uncertainty for $0.00 < |y| < 0.75$.

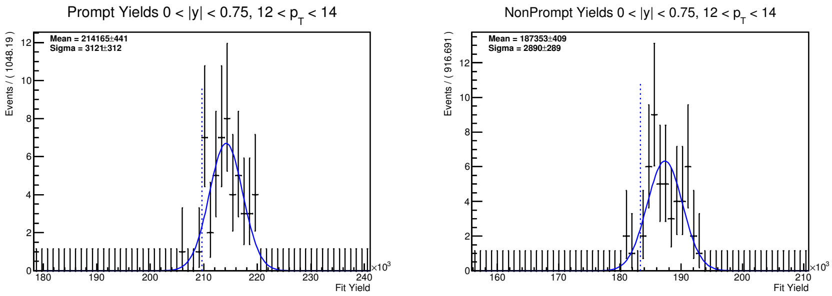

(c) $12 < |p_T| < 14$

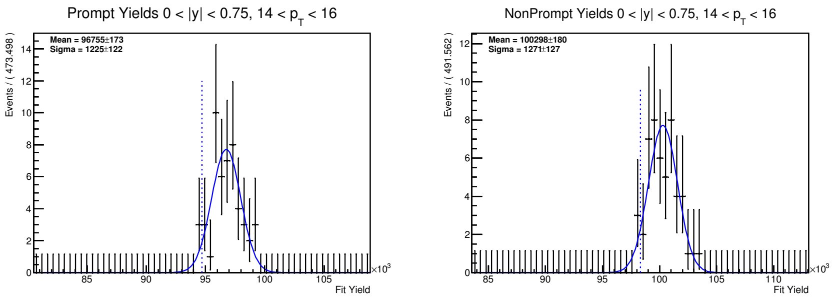

(d) $14 < |p_T| < 16$

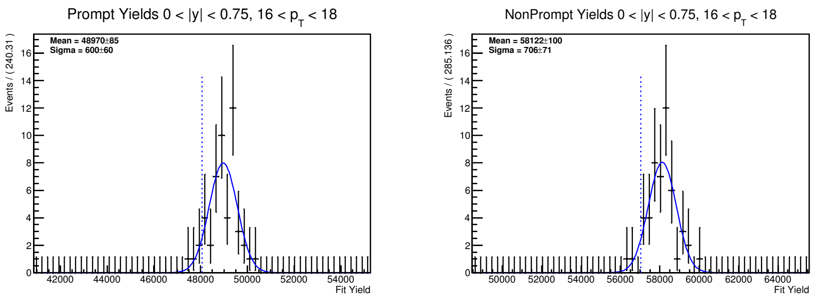

(e) $16 < |p_T| < 18$

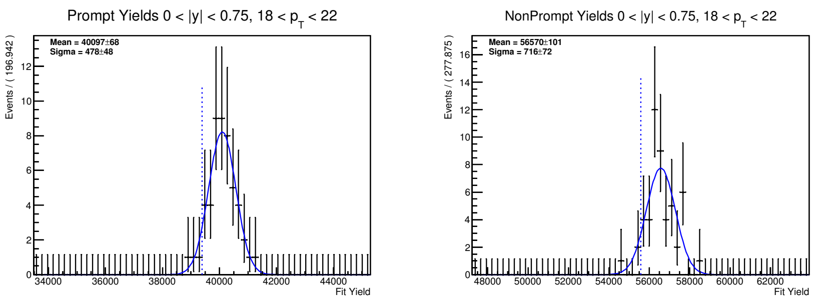

(f) $18 < |p_T| < 22$

Figure E.17: Trigger Reconstruction Uncertainty for $0.00 < |y| < 0.75$ (Continued).

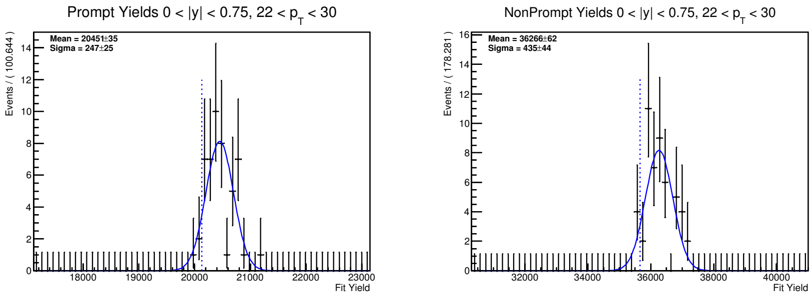

(g) $22 < |p_T| < 30$

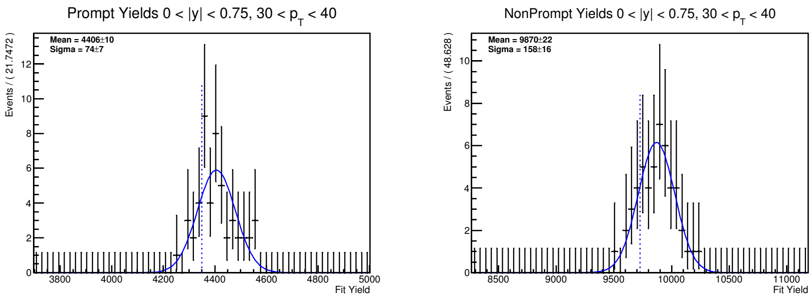

(h) $30 < |p_T| < 40$

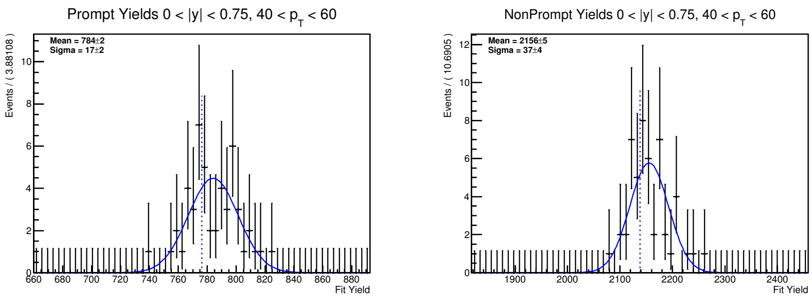

(i) $40 < |p_T| < 60$

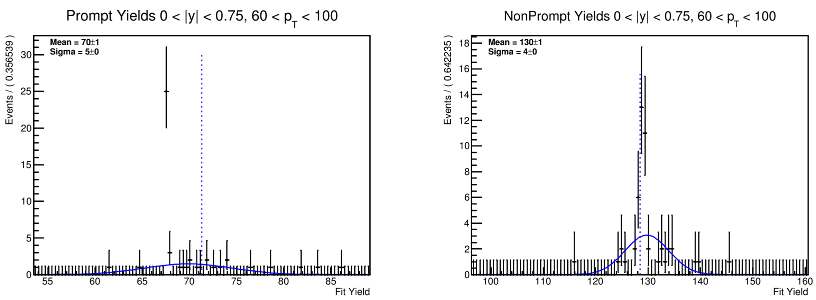

(j) $60 < |p_T| < 100$

Figure E.17: Trigger Reconstruction Uncertainty for $0.00 < |y| < 0.75$ (Continued).

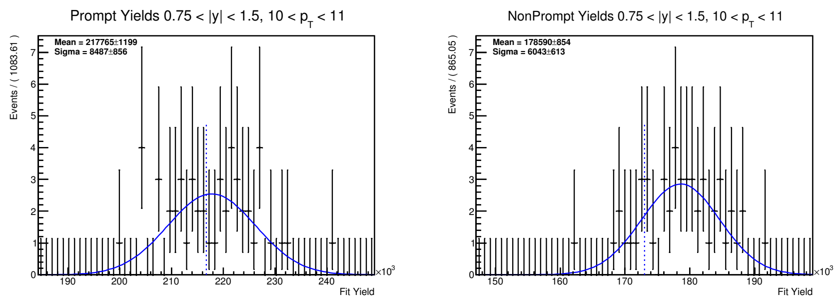

(a) $10 < |p_T| < 11$

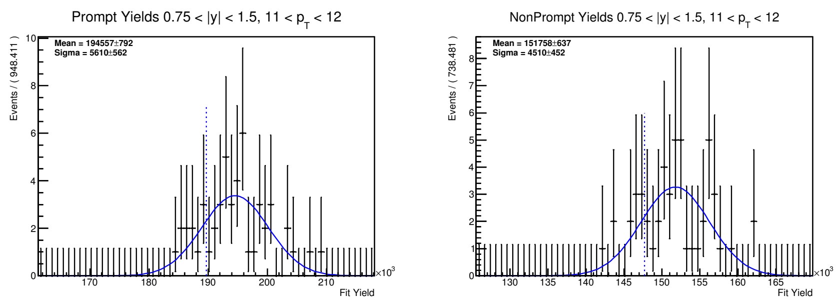

(b) $11 < |p_T| < 12$

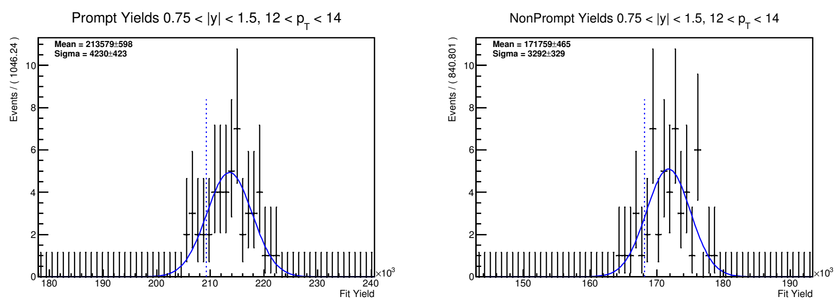

(c) $12 < |p_T| < 14$

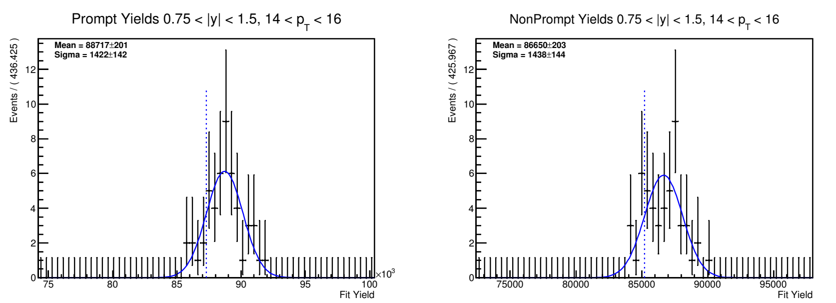

(d) $14 < |p_T| < 16$

Figure E.18: Trigger Reconstruction Uncertainty for $0.75 < |y| < 1.50$.

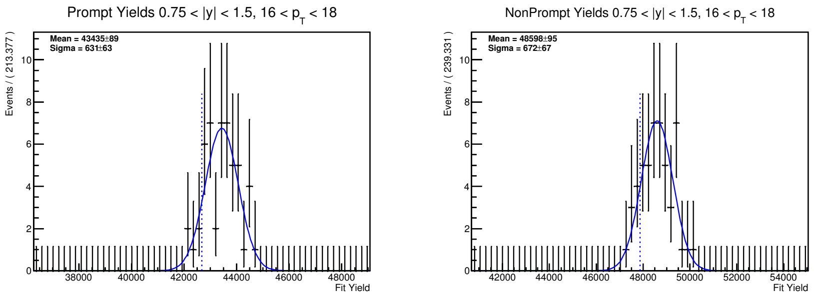

(e) $16 < |p_T| < 18$

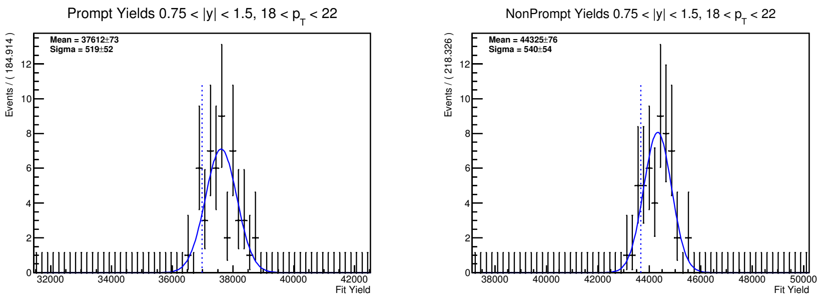

(f) $18 < |p_T| < 22$

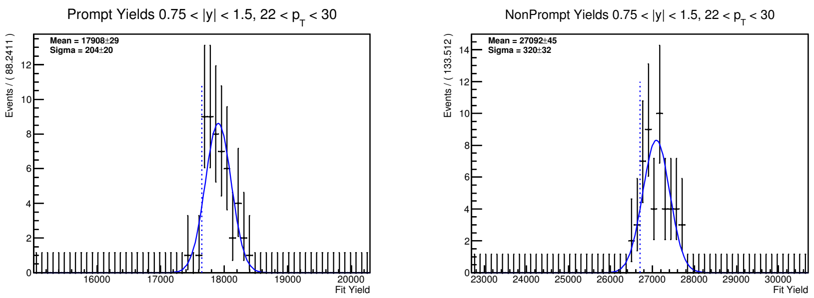

(g) $22 < |p_T| < 30$

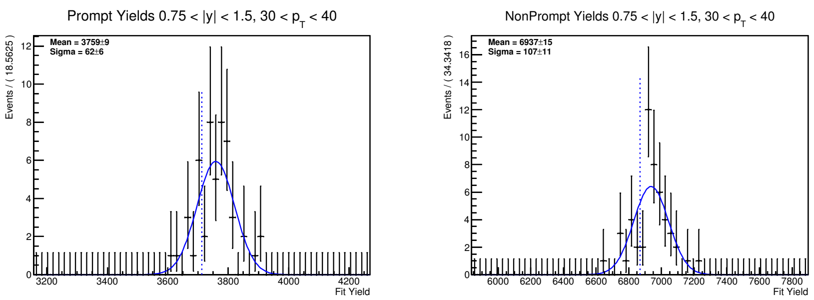

(h) $30 < |p_T| < 40$

Figure E.18: Trigger Reconstruction Uncertainty for $0.75 < |y| < 1.50$ (Continued).

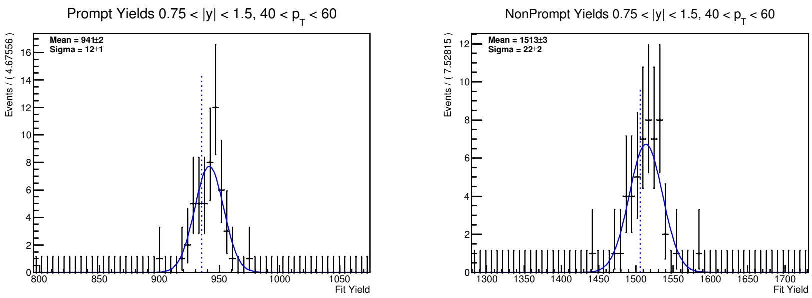

(i) $40 < |p_T| < 60$

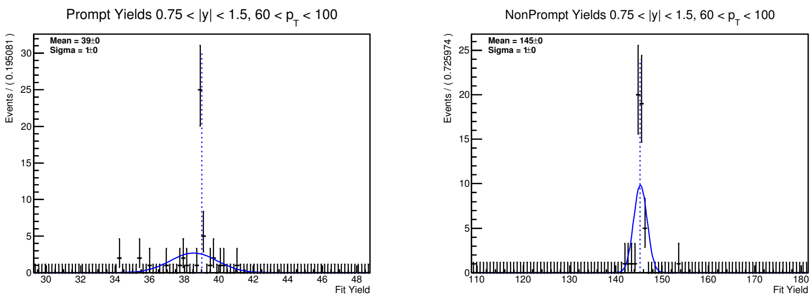

(j) $60 < |p_T| < 100$

Figure E.18: Trigger Reconstruction Uncertainty for $0.75 < |y| < 1.50$ (Continued).

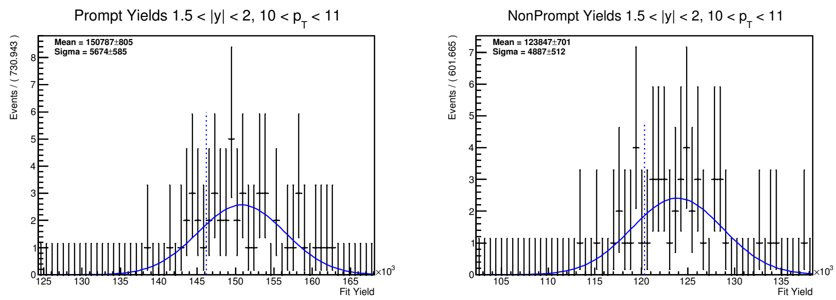

(a) $10 < |p_T| < 11$

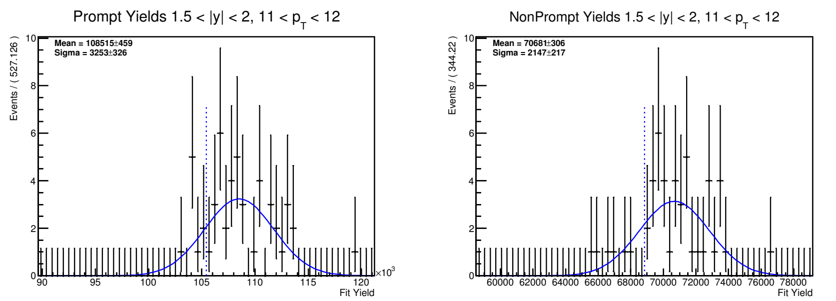

(b) $11 < |p_T| < 12$

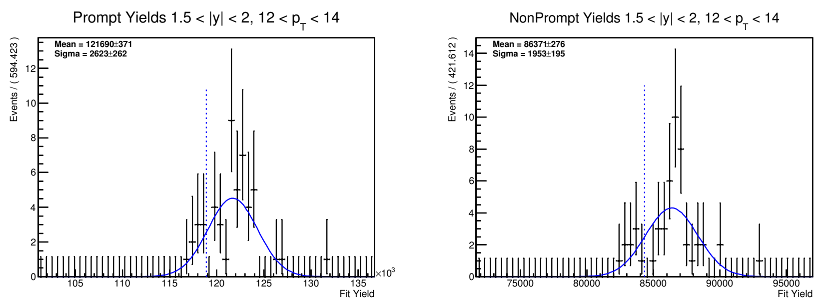

(c) $12 < |p_T| < 14$

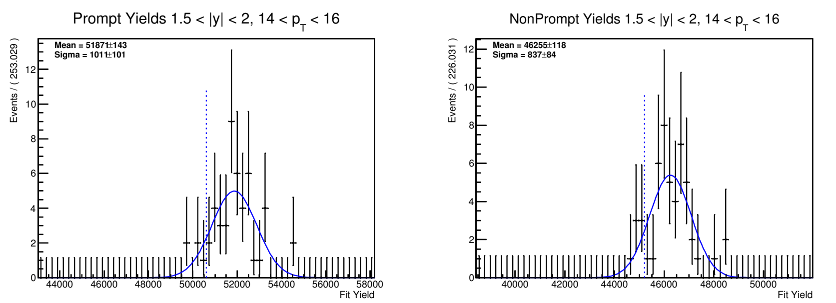

(d) $14 < |p_T| < 16$

Figure E.19: Trigger Reconstruction Uncertainty for $1.50 < |y| < 2.00$.

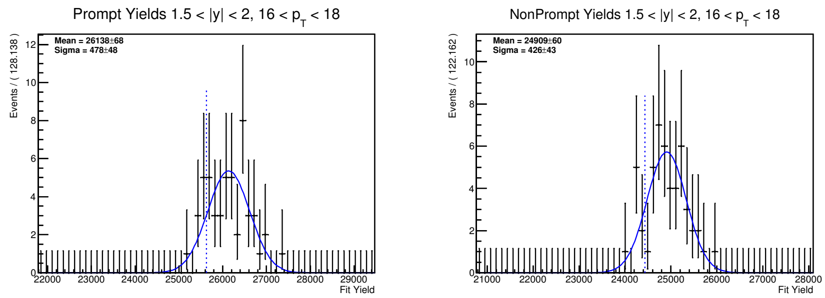

(e) $16 < |p_T| < 18$

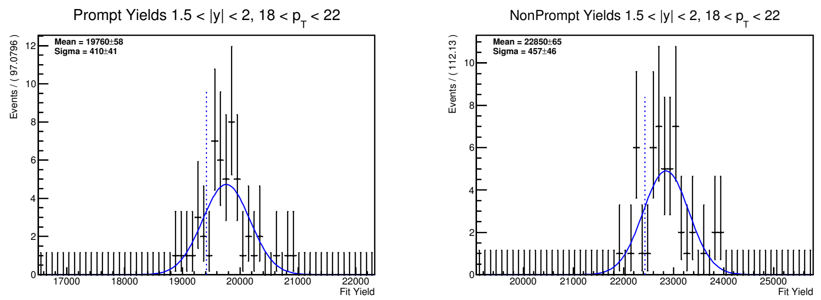

(f) $18 < |p_T| < 22$

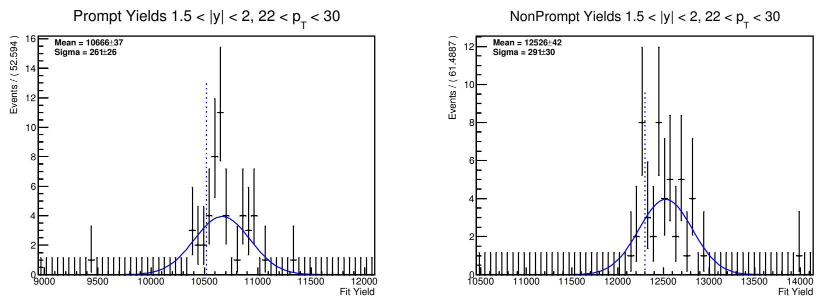

(g) $22 < |p_T| < 30$

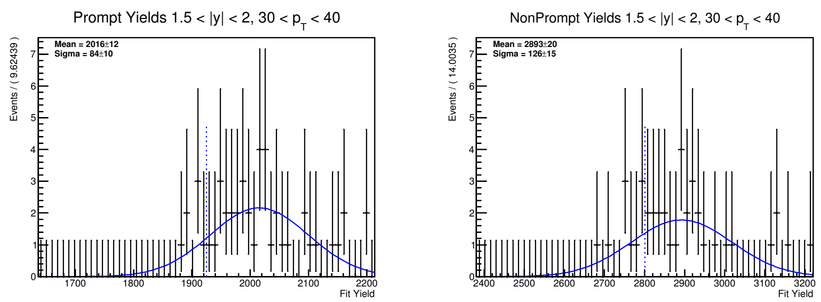

(h) $30 < |p_T| < 40$

Figure E.19: Trigger Reconstruction Uncertainty for $1.50 < |y| < 2.00$ (Continued).

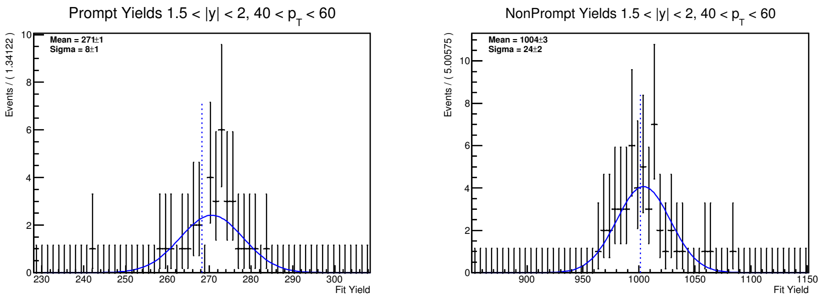

(i) $40 < |p_T| < 60$

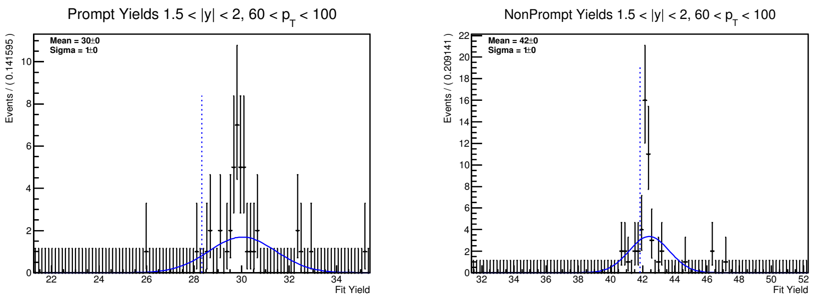

(j) $60 < |p_T| < 100$

Figure E.19: Trigger Reconstruction Uncertainty for $1.50 < |y| < 2.00$ (Continued).

Appendix F

Fit Models

F.1 Fit Models

Shown in this section is the systematic uncertainty arising from varying the fit model, which is the largest systematic uncertainty. Figures (F.1- F.6) show the combination of the cross-sections from all the fit models tested and the total variation from the central model (marked by a dotted line).

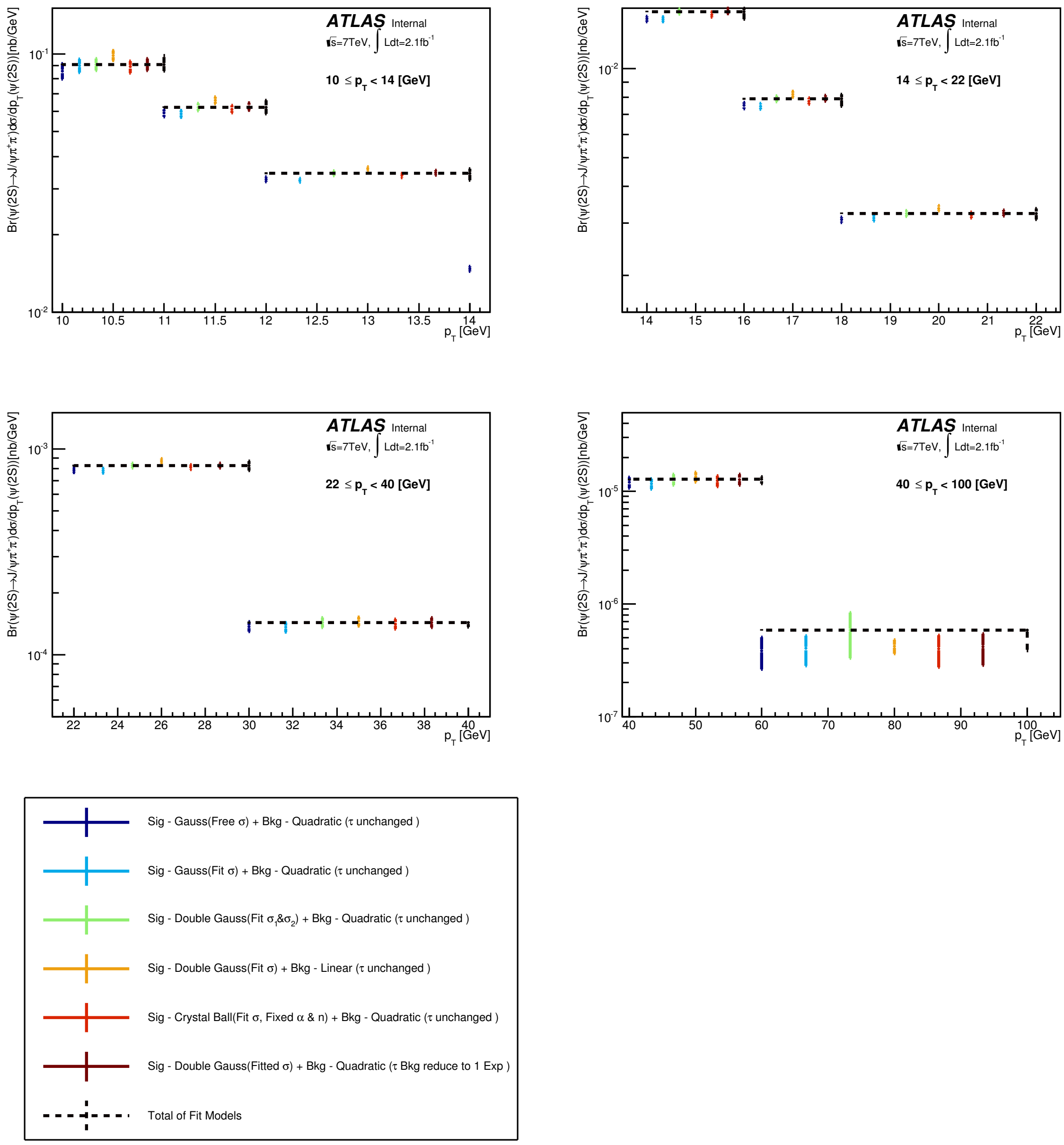

Figure F.1: Comparison of the fit models for the prompt component in the rapidity region $0 \leq |y| < 0.75$.

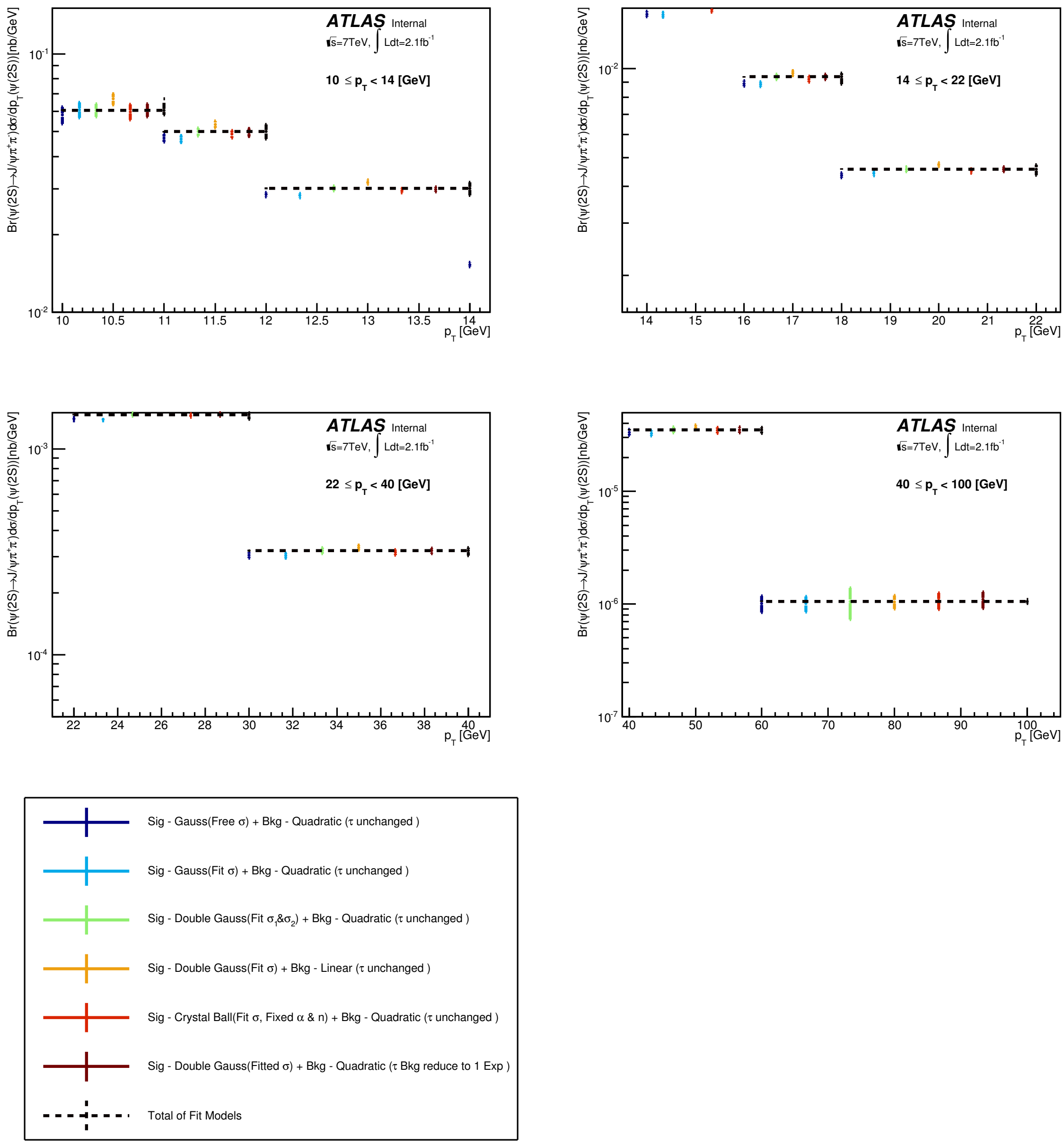

Figure F.2: Comparison of the fit models for the non-prompt component in the rapidity region $0 \leq |y| < 0.75$.

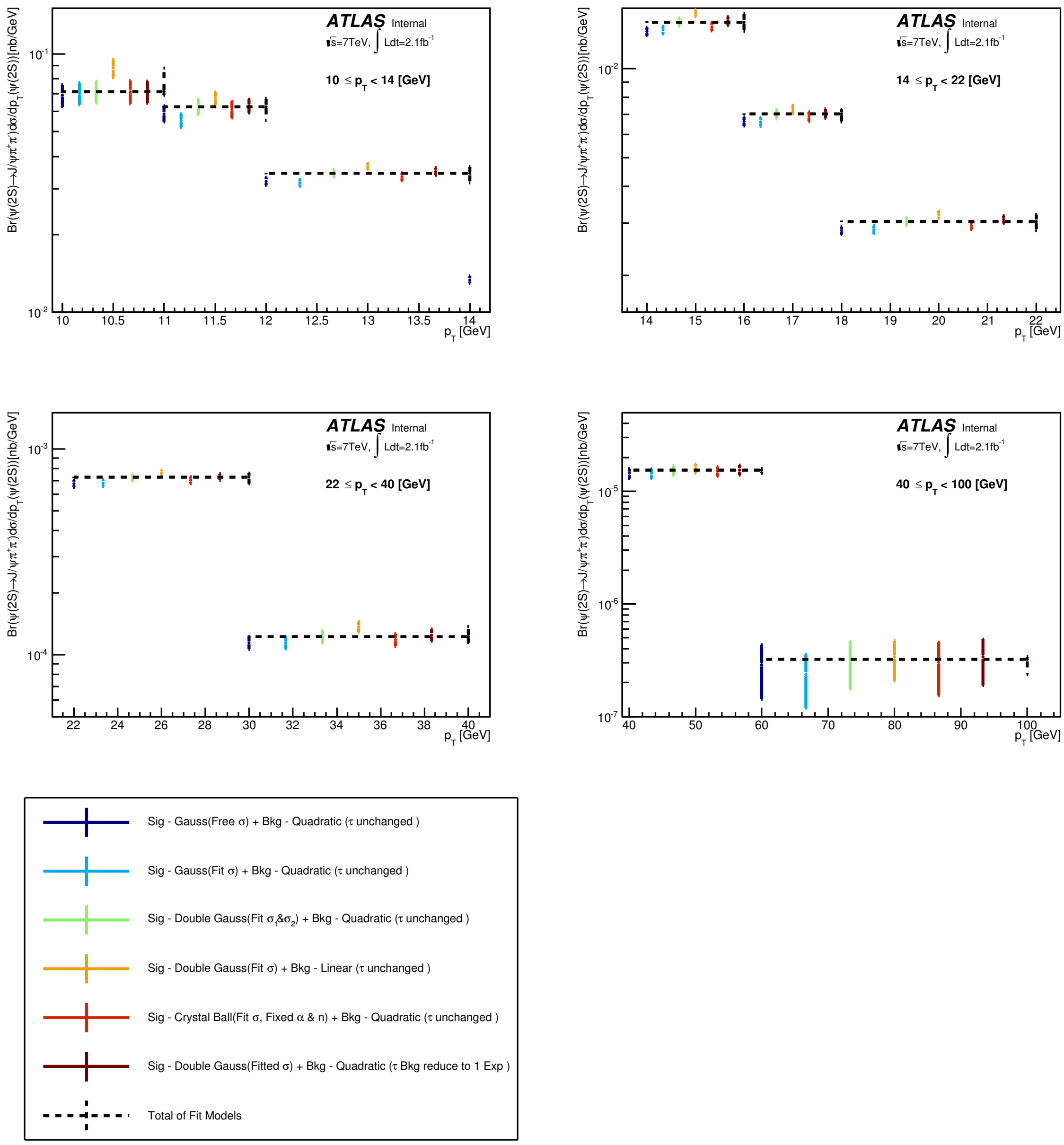

Figure F.3: Comparison of the fit models for the prompt component in the rapidity region $0.75 \leq |y| < 1.5$.

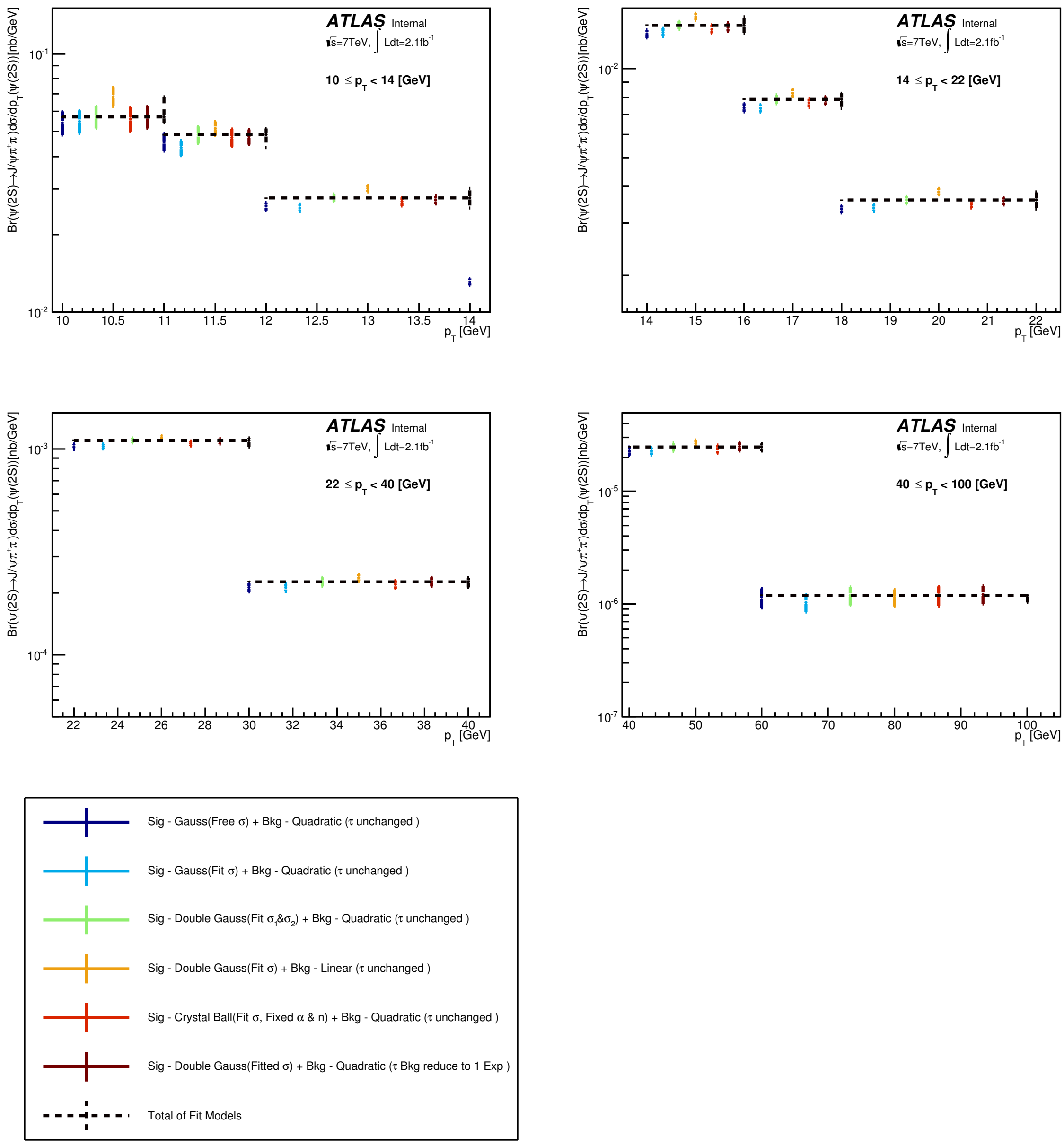

Figure F.4: Comparison of the fit models for the non-prompt component in the rapidity region $0.75 \leq |y| < 1.5$.

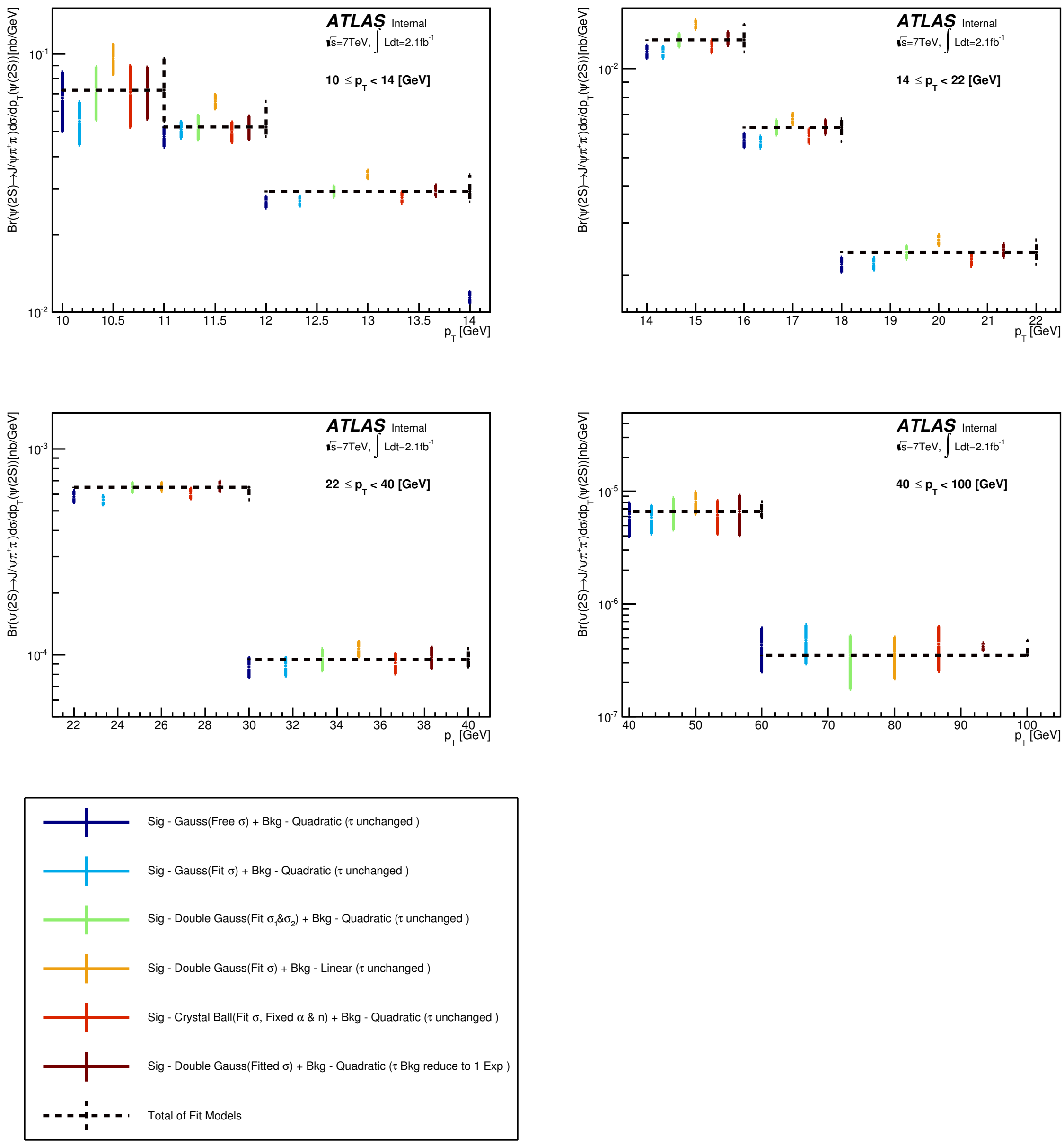

Figure F.5: Comparison of the fit models for the prompt component in the rapidity region $1.5 \leq |y| < 2.0$.

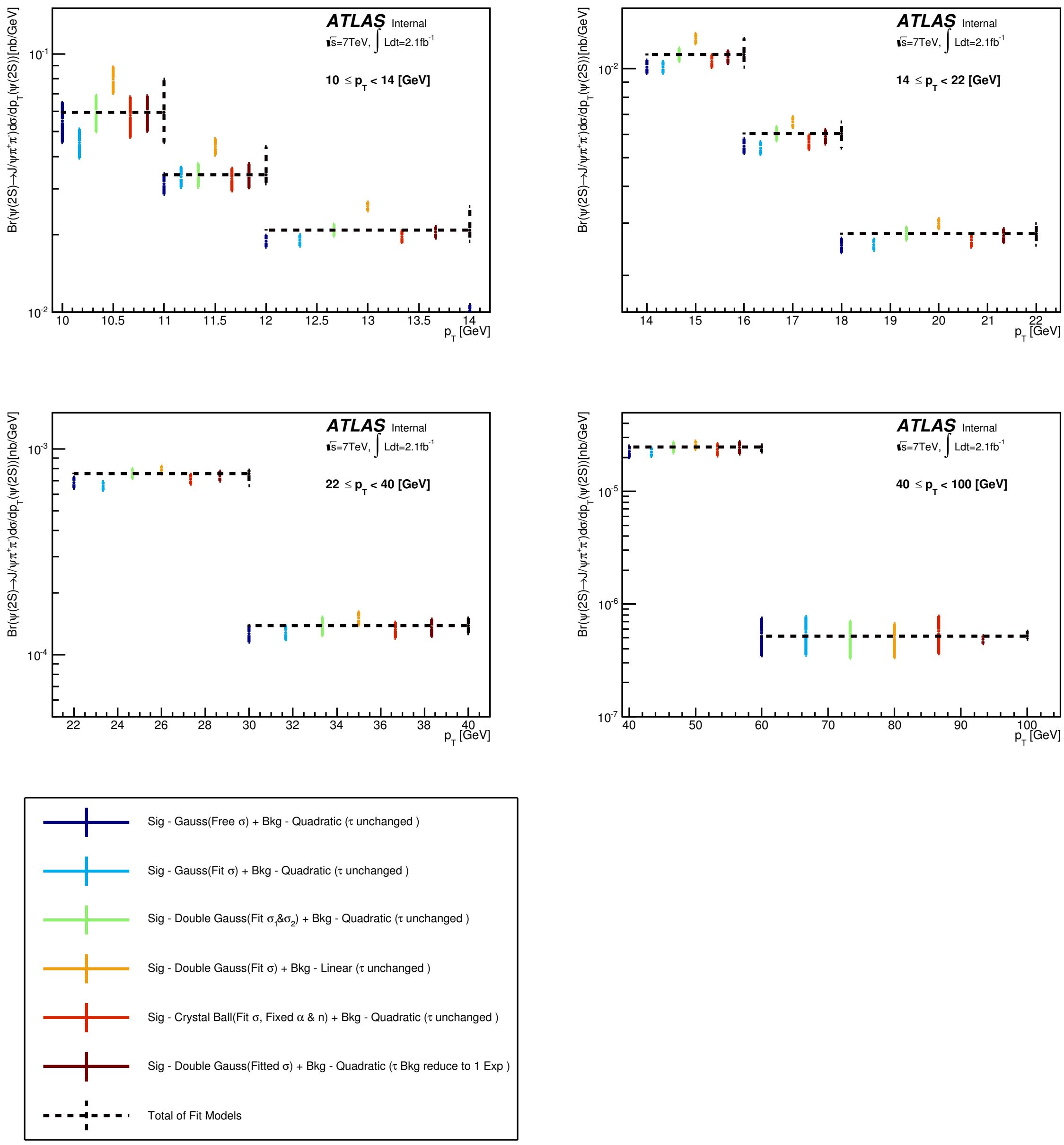

Figure F.6: Comparison of the fit models for the non-prompt component in the rapidity region $1.5 \leq |y| < 2.0$.

Appendix G

Charm 2013

The work in this thesis was presented as a poster and given in a talk by the author, at the 6th International Workshop on Charm Physics (CHARM 2013), held at the University of Manchester. Figure G.1 is the poster that was shown.

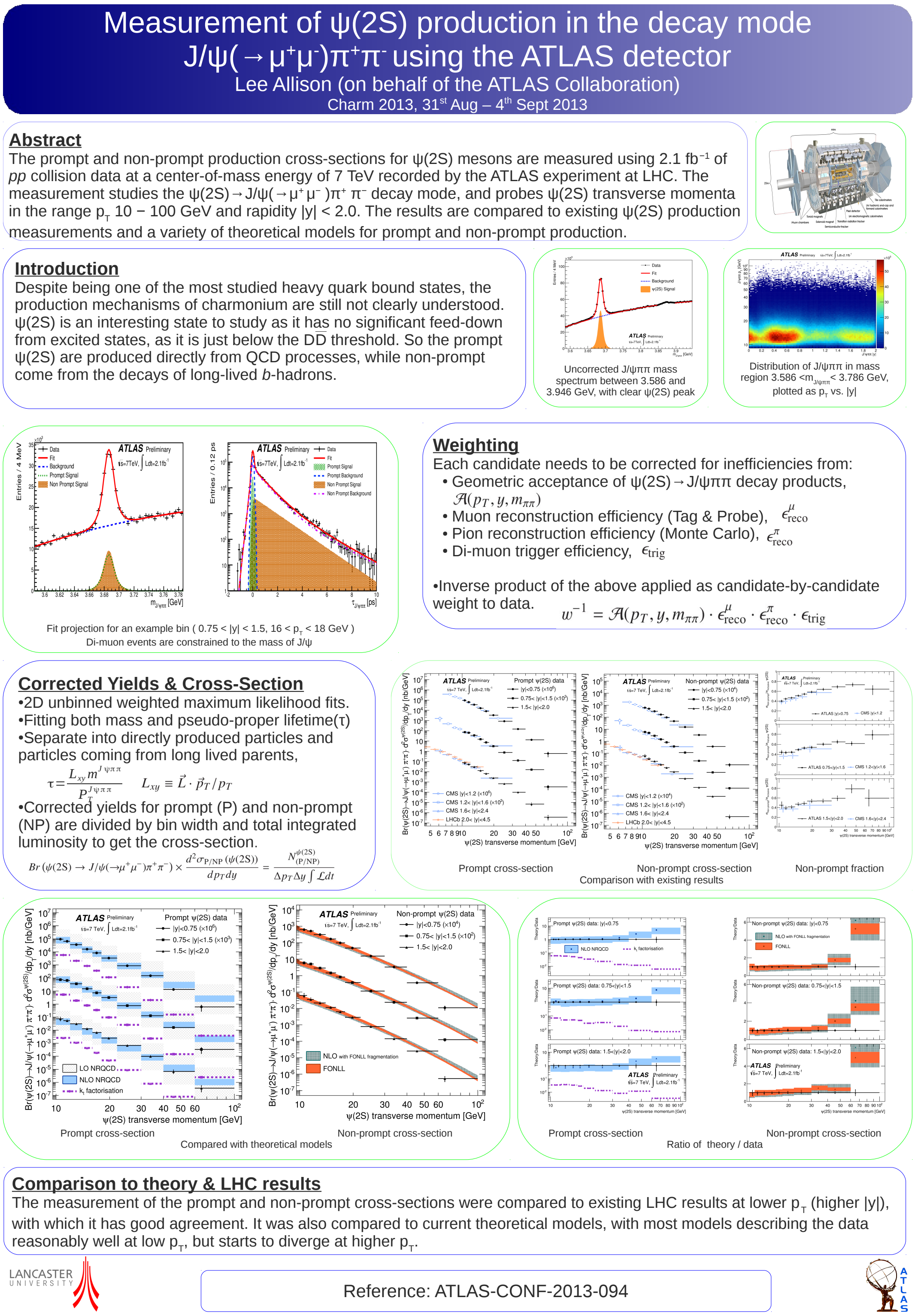

Figure G.1: Poster Presented at the CHARM 2013 conference in Manchester.

References

[1] *Cross-Section Measurement of* $\psi(2S) \to J/\psi(\to \mu^+\mu^-)\pi^+\pi^-$ *in 7 TeV pp collisions at ATLAS*, Tech. Rep. ATLAS-CONF-2013-094, CERN, Geneva, Aug, 2013. 2

[2] A. Purcell, *Go on a particle quest at the first CERN webfest. Le premier webfest du CERN se lance la conqute des particules*,. 4

[3] Wikipedia, *Standard Model — Wikipedia, The Free Encyclopedia*, 2013. `http://en.wikipedia.org/wiki/Standard_Model`. [Online; accessed 2013-09-24]. 5

[4] G. Altarelli, *Collider Physics within the Standard Model: a Primer*, `arXiv:1303.2842 [hep-ph]`. 5

[5] S. Glashow, *Partial Symmetries of Weak Interactions*, Nucl.Phys. **22** (1961) 579–588. 5

[6] S. Weinberg, *A Model of Leptons*, Phys.Rev.Lett. **19** (1967) 1264–1266. 5

[7] P. W. Higgs, *Broken Symmetries and the Masses of Gauge Bosons*, Phys. Rev. Lett. **13** (1964) 508–509. 5

[8] S. Tomonaga, *On a relativistically invariant formulation of the quantum theory of wave fields*, Prog.Theor.Phys. **1** (1946) 27–42. 5

[9] J. S. Schwinger, *Quantum electrodynamics. I A covariant formulation*, Phys.Rev. **74** (1948) 1439. 5

[10] R. Feynman, *Space - time approach to quantum electrodynamics*, Phys.Rev. **76** (1949) 769–789. 5

[11] E. Fermi, *Versuch einer Theorie der -Strahlen. I*, Zeitschrift fr Physik **88** no. 3-4, (1934) 161–177. `http://dx.doi.org/10.1007/BF01351864`. 5

[12] F. L. Wilson, *Fermi's Theory of Beta Decay*, American Journal of Physics **36** no. 12, (1968) 1150–1160. `http://link.aip.org/link/?AJP/36/1150/1`. 5

[13] P. W. Higgs, *Broken Symmetries and the Masses of Gauge Bosons*, Phys.Rev.Lett. **13** (1964) 508–509. 5

[14] H. Fritzsch, M. Gell-Mann, and H. Leutwyler, *Advantages of the Color Octet Gluon Picture*, Phys.Lett. **B47** (1973) 365–368. 6

[15] D. J. Gross and F. Wilczek, *Asymptotically Free Gauge Theories. I*, Phys. Rev. D **8** (1973) 3633–3652. 6

[16] S. Weinberg, *Non-Abelian Gauge Theories of the Strong Interactions*, Phys. Rev. Lett. **31** (1973) 494–497. 6

[17] J. J. Aubert et al., *Experimental Observation of a Heavy Particle J*, Phys. Rev. Lett. **33** (1974) 1404–1406. 6

[18] J. E. Augustin et al., *Discovery of a Narrow Resonance in e^+e^- Annihilation*, Phys. Rev. Lett. **33** (1974) 1406–1408. 6

[19] S. Herb, D. Hom, L. Lederman, J. Sens, H. Snyder, et al., *Observation of a Dimuon Resonance at 9.5-GeV in 400-GeV Proton-Nucleus Collisions*, Phys.Rev.Lett. **39** (1977) 252–255. 6

[20] Belle Collaboration Collaboration, S.-K. Choi et al., *Observation of a Narrow Charmoniumlike State in Exclusive $B^\pm \to K^\pm\pi^+\pi^- J/\psi$ Decays*, Phys. Rev. Lett. **91** (2003) 262001. 6

[21] N. Brambilla, S. Eidelman, B. Heltsley, R. Vogt, G. Bodwin, et al., *Heavy quarkonium: progress, puzzles, and opportunities*, Eur.Phys.J. **C71** (2011) 1534, `arXiv:1010.5827 [hep-ph]`. 6, 9

[22] S. Godfrey, *Topics in Hadron Spectroscopy in 2009*, `arXiv:0910.3409 [hep-ph]`. 8

[23] Quarkonium Working Group Collaboration, N. Brambilla et al., *Heavy quarkonium physics*, `arXiv:hep-ph/0412158 [hep-ph]`. 9

[24] CDF Collaboration, F. Abe et al., *J/ψ and $\psi(2S)$ production in $p\bar{p}$ collisions at $\sqrt{s} = 1.8$ TeV*, Phys.Rev.Lett. **79** (1997) 572–577. 9

[25] J. Lansberg, *On the mechanisms of heavy-quarkonium hadroproduction*, Eur.Phys.J. **C61** (2009) 693–703, `arXiv:0811.4005 [hep-ph]`. 10

[26] ATLAS Collaboration, *Measurement of the differential cross-sections of inclusive, prompt and non-prompt J/ψ production in proton-proton collisions at $\sqrt{s} = 7$ TeV*, Nucl.Phys. **B850** (2011) 387–444, `arXiv:1104.3038 [hep-ex]`. 11, 16, 46, 74

[27] C.-H. Chang, *HADRONIC PRODUCTION OF J / psi ASSOCIATED WITH A GLUON*, Nucl.Phys. **B172** (1980) 425–434. 12

[28] R. Baier and R. Ruckl, *Hadronic Production of J/psi and Upsilon: Transverse Momentum Distributions*, Phys.Lett. **B102** (1981) 364. 12

[29] E. L. Berger and D. L. Jones, *Inelastic Photoproduction of J/psi and Upsilon by Gluons*, Phys.Rev. **D23** (1981) 1521–1530. 12

[30] S. Baranov, A. Lipatov, and N. Zotov, *Prompt J/Ψ production at LHC: new evidence for the k_t-factorization*, Phys.Rev. **D85** (2012) 014034, `arXiv:1108.2856 [hep-ph]`. 12, 74

[31] CMS Collaboration, *J/ψ and ψ_{2S} production in pp collisions at $\sqrt{s} = 7$ TeV*, JHEP **1202** (2012) 011, `arXiv:1111.1557 [hep-ex]`. 13, 15, 68

[32] M. Cacciari, S. Frixione, and P. Nason, *The p(T) spectrum in heavy flavor photoproduction*, JHEP **0103** (2001) 006, `arXiv:hep-ph/0102134 [hep-ph]`. 14, 74

[33] M. Cacciari, S. Frixione, N. Houdeau, M. L. Mangano, P. Nason, et al., *Theoretical predictions for charm and bottom production at the LHC*, JHEP **1210** (2012) 137, `arXiv:1205.6344 [hep-ph]`. 14, 74

[34] V. Kartvelishvili, A. Likhoded, and V. Petrov, *On the Fragmentation Functions of Heavy Quarks Into Hadrons*, Phys.Lett. **B78** (1978) 615. 14

[35] S. Palestini, *Angular distribution and rotations of frame in vector meson decays into lepton pairs*, Phys.Rev. **D83** (2011) 031503, `arXiv:1012.2485 [hep-ph]`. 17, 20

[36] P. Faccioli, C. Lourenco, J. Seixas, and H. K. Wohri, *Towards the experimental clarification of quarkonium polarization*, Eur.Phys.J. **C69** (2010) 657–673, `arXiv:1006.2738 [hep-ph]`. 17, 18

[37] BES Collaboration, J. Bai et al., *psi(2S) → pi+ pi- J / psi decay distributions*, Phys.Rev. **D62** (2000) 032002, `arXiv:hep-ex/9909038 [hep-ex]`. 17, 50, 96

[38] CMS Collaboration, *Measurement of the prompt J/ψ and $\psi(2S)$ polarizations in pp collisions at $\sqrt{s} = 7$ TeV*, `arXiv:1307.6070 [hep-ex]`. 17, 19

[39] CMS Collaboration, *Measurement of the Y1S, Y2S and Y3S polarizations in pp collisions at $\sqrt{s} = 7$ TeV*, Phys.Rev.Lett. **110** (2013) 081802, `arXiv:1209.2922 [hep-ex]`. 17

[40] C. Lefevre, "Lhc: the guide (english version). guide du lhc (version anglaise)." Feb, 2009. 22

[41] C. Lefvre, "The cern accelerator complex. complexe des acclrateurs du cern." Dec, 2008. 22

[42] "The large hadron collider." `http://home.web.cern.ch/about/accelerators/large-hadron-collider`. Accessed: 2013-09-23. 21

[43] M. Bajko et al., *Report of the Task Force on the Incident of 19th September 2008 at the LHC*, Tech. Rep. LHC-PROJECT-Report-1168. CERN-LHC-PROJECT-Report-1168, CERN, Geneva, Mar, 2009. 23

[44] *The LHC quench protection system. Le systme de protection contre les transitions du LHC*,. 23

[45] "The lhc is back (press release)." `http://press.web.cern.ch/press-releases/2009/11/lhc-back`. Accessed: 2013-09-23. 23

[46] "Atlas luminosity public results." `https://twiki.cern.ch/twiki/bin/view/AtlasPublic/LuminosityPublicResults`. Accessed: 2013-09-23. 23, 24

[47] ATLAS Collaboration, *Observation of a new χ_b state in radiative transitions to $\Upsilon(1S)$ and $\Upsilon(2S)$ at ATLAS*, Phys.Rev.Lett. **108** (2012) 152001, `arXiv:1112.5154 [hep-ex]`. 23

[48] ATLAS Collaboration, *Observation of a new particle in the search for the Standard Model Higgs boson with the ATLAS detector at the LHC*, Phys.Lett. **B716** (2012) 1–29, `arXiv:1207.7214 [hep-ex]`. 23

[49] CMS Collaboration, *Observation of a new boson at a mass of 125 GeV with the CMS experiment at the LHC*, Phys.Lett. **B716** (2012) 30–61, `arXiv:1207.7235 [hep-ex]`. 23

[50] ATLAS Collaboration, *The ATLAS Experiment at the CERN Large Hadron Collider*, JINST **3** (2008) S08003. 23

[51] J. Pequenao, "Computer generated image of the whole atlas detector." Mar, 2008. 25

[52] J. Pequenao, "Computer generated image of the atlas inner detector." Mar, 2008. 27, 28

[53] J. Pequenao, "Computer generated image of the atlas calorimeter." Mar, 2008. 29

[54] J. Pequenao, "Computer generated image of the atlas muons subsystem." Mar, 2008. 31

[55] ATLAS Collaboration, *Commissioning of the ATLAS Muon Spectrometer with Cosmic Rays*, Eur. Phys. J. C **70** no. arXiv:1006.4384. CERN-PH-EP-2010-045, (2010) 875–916. 58 p. 33, 34

[56] *ATLAS detector and physics performance: Technical Design Report, 1.* Technical Design Report ATLAS. CERN, Geneva, 1999. Electronic version not available. 36

[57] "Computing." `http://home.web.cern.ch/about/computing`. Accessed: 2013-09-23. 37

[58] *Atlas Computing: technical design report.* CERN, Geneva, 2005. 37

[59] "B physics trigger public results." `https://twiki.cern.ch/twiki/bin/view/AtlasPublic/BPhysicsTriggerPublicResults`. Accessed: 2013-09-24. 39

[60] ATLAS Collaboration, E. Piccaro, *Measurement of the ATLAS di-muon trigger efficiency in proton-proton collisions at 7 TeV*, `arXiv:1111.4329 [hep-ex]`. 40

[61] ATLAS Collaboration, *Improved luminosity determination in pp collisions at $\sqrt{s} = 7$ TeV using the ATLAS detector at the LHC*, Eur.Phys.J. **C73** (2013) 2518, `arXiv:1302.4393 [hep-ex]`. 44, 63

[62] ATLAS Collaboration, *Time-dependent angular analysis of the decay $B_s^0 \to J/\psi\phi$ and extraction of $\Delta\Gamma_s$ and the CP-violating weak phase ϕ_s by ATLAS*, JHEP **1212** (2012) 072, `arXiv:1208.0572 [hep-ex]`. 44

[63] Particle Data Group Collaboration, J. Beringer et al., *Review of Particle Physics (RPP)*, Phys.Rev. **D86** (2012) 010001. 44

[64] ATLAS Collaboration, *Measurement of Upsilon production in 7 TeV pp collisions at ATLAS*, Phys.Rev. **D87** (2013) 052004, `arXiv:1211.7255 [hep-ex]`. 53, 54, 57, 83

[65] ATLAS Collaboration, *Charged-particle multiplicities in pp interactions measured with the ATLAS detector at the LHC*, New J.Phys. **13** (2011) 053033, `arXiv:1012.5104 [hep-ex]`. 53

[66] A. Collaboration, *Track Reconstruction Efficiency in sqrt(s)=7 TeV Data for Tracks with pT > 100 MeV*, Tech. Rep. ATL-PHYS-INT-2011-001, CERN, Geneva, Jan, 2011. 54, 62

[67] M. Oreglia, *A Study of the Reactions $\psi' \to \gamma\gamma\psi$*. PhD thesis, 1980. SLAC-R-0236. 62

[68] J. Gaiser, *CHARMONIUM SPECTROSCOPY FROM RADIATIVE DECAYS OF THE J / psi AND psi-prime*. PhD thesis, 1982. SLAC-R-0255. 62

[69] T. Skwarnicki, *A study of the radiative CASCADE transitions between the Upsilon-Prime and Upsilon resonances*. PhD thesis, 1986. DESY-F31-86-02. 62

[70] LHCb Collaboration, R. Aaij et al., *Measurement of $\psi(2S)$ meson production in pp collisions at sqrt(s)=7 TeV*, Eur.Phys.J. **C72** (2012) 2100, `arXiv:1204.1258 [hep-ex]`. 68, 96

[71] A. Kanaki and C. G. Papadopoulos, *HELAC: A Package to compute electroweak helicity amplitudes*, Comput.Phys.Commun. **132** (2000) 306–315, `arXiv:hep-ph/0002082 [hep-ph]`. 68

[72] Y.-Q. Ma, K. Wang, and K.-T. Chao, *$J/\psi(\psi')$ production at the Tevatron and LHC at $\mathcal{O}(\alpha_s^4 v^4)$ in nonrelativistic QCD*, Phys.Rev.Lett. **106** (2011) 042002, `arXiv:1009.3655 [hep-ph]`. 68

[73] M. Kramer, *Quarkonium production at high-energy colliders*, Prog.Part.Nucl.Phys. **47** (2001) 141–201, arXiv:hep-ph/0106120 [hep-ph]. 68

[74] H. Jung, *Un-integrated PDFs in CCFM*, arXiv:hep-ph/0411287 [hep-ph]. 74

[75] ATLAS Collaboration, *Measurement of χ_{c1} and χ_{c2} production with $\sqrt{s} = 7\,\mathrm{TeV}$ pp collisions at ATLAS*, ATLAS-CONF-2013-095. 74

[76] ATLAS Collaboration, *Measurement of the differential cross-section of B^+ meson production in pp collisions at $\sqrt{s} = 7$ TeV at ATLAS*, arXiv:1307.0126 [hep-ex]. 74

[77] W. Liebig, "Id track selection for physics muons." http://indico.cern.ch/getFile.py/access?subContId=0&contribId=6&resId=0&materialId=slides&confId=164884. 83

[78] A. Collaboration, "Internal documentation of j/ψ cross-section paper." https://cds.cern.ch/record/1313486/files/ATL-COM-PHYS-2010-1035.pdf. 85

[79] Y.-Q. Ma, K. Wang, and K.-T. Chao, *$J/\psi(\psi')$ production at the Tevatron and LHC at $\mathcal{O}(\alpha_s^4 v^4)$ in nonrelativistic QCD*, Phys.Rev.Lett. **106** (2011) 042002, arXiv:1009.3655 [hep-ph].